EXPERIMENTAL AND CFD INVESTIGATIONS OF THE CHARACTERICSTICS OF FLUID FLOW AND AIR CORE INSIDE A HYDROCYCLONE SEPARATOR

By

CHINMAY SHINGOTE

Submitted in partial fulfillment of the requirements for the degree of Master of Science

Thesis Advisors: Dr. Jaikrishnan R. Kadambi and Dr. John Furlan

Department of Mechanical and Aerospace Engineering

CASE WESTERN RESERVE UNIVERSITY

January, 2018

CASE WESTERN RESERVE UNIVERSITY

SCHOOL OF GRADUATE STUDIES

We hereby approve the thesis of

Chinmay Shingote

candidate for the degree of Master of Science *.

Committee Chair

Dr Jaikrishnan Kadambi

Committee Member

Dr. John Furlan

Committee Member

Dr. Bo Li

Date of Defense

11/13/2017

*We also certify that written approval has been obtained

LIST OF TABLES

LIST OF FIGURES

ACKNOWLEDGEMENTS

First of all, I would like to thank my research advisor, Dr. J.R. Kadambi, for his invaluable guidance and teachings for this research project. I have gained a lot of skill and knowledge in the areas of fluid mechanics and experimental measurement using PIV techniques. Without his efforts and mentoring, this project would not be completed. I would also like to appreciate the help of my lab mates, Renjie, Erdem, Zhuyan and Daniel, for their help to improve my research and setting up everything for the experiments. They also gave me many useful suggestions in computational works, I enjoyed working with those people.

Next, I would like to thank to GIW Industries, Inc. for their great support and especially to Dr. John M. Furlan for his endless technical help, knowledgeable comments and new ideas which always inspired me to learn more. I'm genuinely grateful for all of his suggestions which made this study possible. I am thankful to Dr. Mohamed Garman for helping me throughout my thesis to obtain great computational results.

I also want to thank my committee members Dr. B. Li and Dr. J. Furlan.

I would like to thank Dr. Mark Wernet, the developer of the post-processing software used in the research and a pioneer in the area of PIV, for his precious time and help towards the technical assistance for the software setup.

Finally, I want to thank Sam Cordaro, Wayne Schmidt and John Weber, from the machine shop, for all of their advice and help in order to get the experimental setup up and running on time.

NOMENCLATURE

CCD	Charge coupled device
CFD	Computational Fluid Dynamics
D_C	Diameter of the cylindrical section of the cyclone
D_x	Control surface diameter
d_{laser}	Diameter of the laser beam
d_e	Effective particle size
d_p	Effective particle size
f	Focal length
FOV	Field of View
f_c	Focal length of the cylindrical lens
f_s	Focal length of the spherical lens
f#	f number of the camera
g	Gravitational acceleration
H	Height of the cylindrical section
H_{CS}	Height of the control surface
I	Turbulence intensity

i	X coordinate of vector map (index)
j	Y coordinate of vector map (index)
k	Turbulent kinetic energy
LES	Large Eddy Simulation
M	Optical system magnification
N	Number of pixels
NAI	Sodium Iodide
N_s	Number of measurements
PIV	Particle Image Velocimetry
P_s	Static pressure
p’	Modified pressure
Q	Volumetric flow rate
Re_D	Reynolds number based on the inlet diameter
RI	Refractive Index
RSM	Reynolds Stress Model
r-z	radial-axial plane
r-θ	radial-tangential plane

s	Imaged pixel size
SR	Spatial Resolution
$S_{i,j}$	Standard Deviation of the velocity at each grid point on vector
T_{LS}	Minimum light sheet thickness
U	Inlet velocity
u’	Fluctuating velocity component
V_m	Velocity of fastest particles
V_r	Radial Velocity
V_s	Settling Velocity
V_x	Axial Velocity
V_θ	Tangential Velocity
W_S	Width of the laser sheet
Δx	Seed particle displacement
Δt	Interframe time
λ	Wavelength of the laser beam
δ_z	Camera depth of field
γ	Turbulent length scale

ρ_f	Density of the working fluid
ρ_p	Density of the tracing particles
μ	Dynamic viscosity
μ_t	Turbulent viscosity
μ_{eff}	Turbulent effective viscosity
σ_{u}	Uncertainty in velocity
σ_{t}	Temporal uncertainty
σ_{x}	Spatial uncertainty
σ_{system}	Systematic uncertainty
σ_{random}	Random uncertainty
σ_{total}	Total uncertainty
$\tau_{\mathrm{ij}}^{\mathrm{sgs}}$	Residual stress tensor

Experimental and CFD Investigations of the Characteristics of Fluid Flow and Air Core Inside a Hydrocyclone Separator

Abstract

by

CHINMAY SHINGOTE

Hydrocyclone separators are widely used in industrial applications in the oil and mining industry to sort, classify and separate solid particles or liquid droplets within liquid suspensions. Numerous valuable studies have been performed recent years to investigate the flow field inside hydrocyclones.

However, the information regarding the performance of cyclones has limitations. Based on the current available theoretical models, it cannot be considered completely applicable when related to the most real-world applications. Therefore, in this thesis, a two phase flow system inside a hydrocyclone was explored with the aid of both computational and experimental techniques (Particle Image Velocimetry).

The previous work, completed by Ke (2016) using the same technique as the current study, mainly focused on the flow field in the r-θ plane, within a hydrocyclone running with an air core. The study revealed several physical phenomena and flow patterns of multi-phase flow in a hydrocyclone. An air core is generated along the central axis of the hydrocyclone, as the

underflow is open to atmosphere. In this study, the flow field in the r-z plane has been investigated.

The computational modelling was performed using a commercial Computational Fluid Dynamics (CFD) software package, CD-Adapco Star CCM+. Using the built-in mesh generator, a mesh domain containing more than 1,170,205 unstructured cells was created in a Cartesian coordinate system. To improve the numerical calculation accuracy and provide a logical and meaningful comparison with the experimental results, two numerical models were used: Large Eddy Turbulence Model, and Volume of Fluid multiphase model to handle the air core. The second order discretization scheme was more suitable to get an accurate simulation of the flow field. The velocity and pressure contours belonging to various section planes will be presented and discussed. Additionally, the computational studies also focused on the prediction of the dimensions of the air core.

For experimental investigations, Particle Imaging Velocimetry (PIV) method was used. A laser was used as the light source. The laser projected a laser plane in the desired section of the Hydrocyclone. In order to use PIV, Refractive index matching procedure was used. The Hydrocyclone model was made of clear acrylic material. The test liquid used in the experiment was sodium iodide aqueous solution (63.3% NaI by weight) in order to achieve the refractive index matching. The seed particles used in this experiment were 10 µm silver coated hollow glass spheres which were introduced into the flow by global seeding. Four fields of view (FOV) were used in the r-z plane of the hydrocyclone. The laser sheet was set just in front of the air core to observe the flow field around the air core. Two dimensional velocity vector maps were shown on each of the fields of view.

The experimental data were compared to the numerical results. The Large Eddy Turbulence model produced a physically accurate air volume fraction contour when applied with the Volume of Fluid Multi-phase model. The data obtained from PIV was used to validate the numerical result. The value of axial velocity was in good agreement along the r-z plane with the computational values. The shape and diameter of the air core were in good agreement with the experimental data, and the physical time of the air core generation calculated from the simulation approximated to the time scale observed in the experiments.

CHAPTER 1

INTRODUCTION

A hydrocyclone is a device used to separate, classify, and sort a liquid suspension system into at least two separate density components. The flow field of the hydrocyclone is generally a multi-phases flow system. In 1891 E. Bretney obtained the first patent for hydrocyclone predecessor of all the conventional hydrocyclones. This sparked the applications hydrocyclones in numerous industries including oil, drilling, metal working and mineral processing.

A modern hydrocyclone normally has a cylindrical section at the top liquid is being fed tangentially and a conical base tapering downwards is attached to the bottom of the cylindrical section. The geometry of the cyclone and the feed stream characteristics play a significant role in hydrocyclone operation. The mixture is fed to the cylindrical chamber through a tangential inlet. A high swirling flow is seen in the conical section due to the high acceleration of the tangential inlet. This causes centrifugal and centripetal forces in the flow field which are considered as the primary separation mechanism.

The dense and coarse particles have a higher ratios of body force to fluid drag force which causes them to concentrate and travel towards the wall of the cyclone body, while the light and fine particles have a low body force to fluid drag force which caused them to accumulate near the center axis of the cyclone. Therefore, the heavier particles travel in a spiral path with the fluid suspension and are discharged through a spigot. This outlet is defined as “underflow outlet”. The finer and lighter particles concentrate along central axis of the cyclone and move upwards towards the cylindrical part and are discharged through the vortex finder. This outlet is defined as “overflow outlet”.

Previous works finished by Renjie Ke (2016) laid a foundation for current study. The flow inside a hydrocyclone has three components: tangential, axial and radial. The tangential velocity has the highest magnitude, whereas the radial velocity is very small and has very less influence on the separation process. The axial and the tangential velocities will be examined in these experiments. The tangential velocity is proportional to the radius of the cyclone. The tangential velocity increases as the flow area diminishes along the conical section towards the underflow. The magnitude of axial velocities below the vortex finder is equal to zero. This region is called “locus of zero” (Rietema, 1960).

Figure 1.2 (Dlamini 2005) shows the two distinct flow patterns present inside the hydrocyclone. The Rankine vortex, which is a combination of two vortices: (a) the outer swirl vortex, (b) the inner swirl vortex. The difference between the two vortices is whether the tangential velocity is proportional to the radius (forced vortex, inner vortex) or to the inverse of the radius (free, outer vortex) (Chiné & Concha, 2000). Moreover, the eddy flow will occur when the inner swirl is unable to pass through the vortex finder (Heiskanen, 1993).

1.1 Hydrocyclone Geometry

The model used in the current study is the same used by Ke (2016) study; the only difference being the addition of a U-loop at the overflow which is used to install the SONARtrac instrument. SONARtrac is a device used for measuring the volume fraction of air in the overflow return piping of the cyclone. A hydrocyclone has two outlets along the central axis, the apex and the bottom of the conical section called as the underflow and the vortex finder at the top of the cylindrical section called the overflow. Figure 1.1 shows a typical hydrocyclone that is widely used in the mineral processing industry.

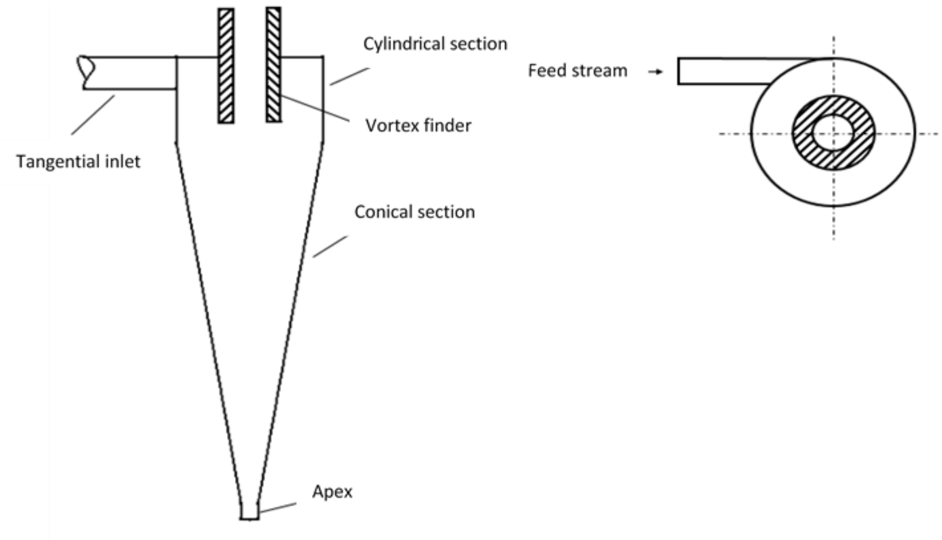

Figure 1.1 Hydrocyclone Schematic

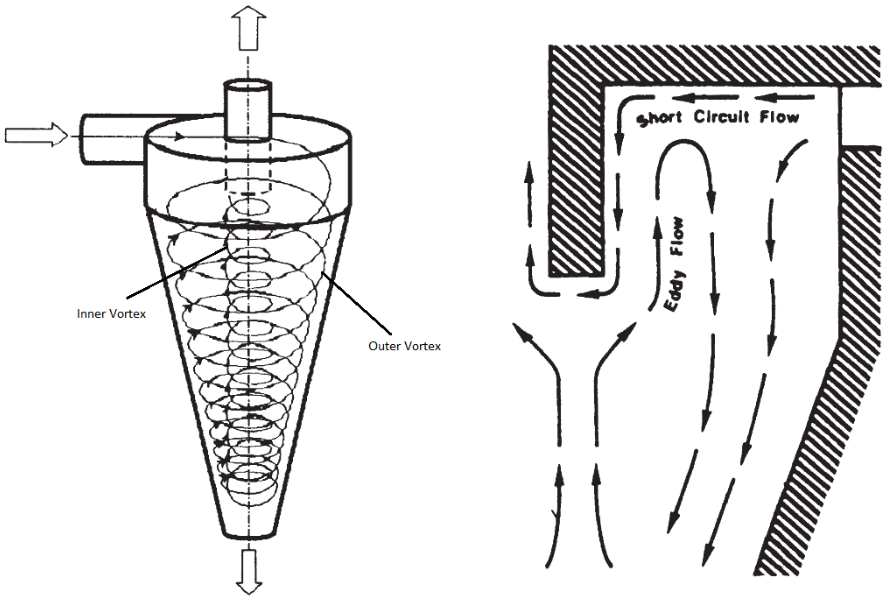

Figure 1.2 Flow patterns in a cyclone (a) vortices (b) secondary flows (Dlamini, 2005)

The hydrocyclone geometric parameters consists of inlet diameter, cylindrical section, cone angle, length of the cylindrical section and total height of the cyclone, vortex finder and apex diameter. The geometry has a direct impact on the device performance. These parameters have to be precisely considered in designing the hydrocyclone since the hydrocyclone has no moving parts. Industries alter the total height of the cyclone depending on the application. Heiskanen (1993) suggested the variation of the height of the cylindrical section;

$$h = kD_c \qquad \text{(where } 0.7<k\text{)} \qquad (1.1)$$

The increase in the height of the hydrocyclone results in a higher separation efficiency as well as increases the capacity of the device. According to Heiskanen (1993), the maximum improvement in the separation efficiency occurs at $h=5D_c$, where D_c is the cyclone diameter, and h is the overall height.

1.2 History of Hydrocyclones Development

Air cyclones were the first cyclones, and were used for removing dust from air. These cyclones were based on using the centrifugal forces for separating the dust particles from air. Knickerbocker Company, USA received the first patent for the air cyclones in 1885. In 1891, E. Bretney received the first patent for a hydrocyclone predecessor (US Patent No: 453. 105). The first commercial cyclone was installed in a phosphate plant in USA in 1914. From 1891 to 1939, many patents related to non-commercial hydrocyclones were handed out to different individuals.

The first application of hydrocyclones in mining was done in 1939 by Dutch State Mines, which were used for removing sand from coal. In the following ten years, the most prolific period of development of the hydrocyclones occurred, during which they were applied to various industrial applications. The basic design of the hydrocyclones has not changed much ever since. With the development of advanced computer technology and experimental methods, researchers have found new ways to investigate hydrocyclone flow fields.

1.3 Literature Review

Hydrocyclones have a wide variety of applications in many industries, particularly in mineral and chemical processing. In the past years, scientists and researchers have developed many theoretical models for predicting the velocity fields and pressure regions inside the hydrocyclone. These theoretical models were used for developing hydrocyclones with higher efficiencies. For a long time, the selection and the design of hydrocyclones was based on empirical equations and experience. In 1982, Richard A. Arterburn published in his study as a basic thumb rule for selecting the correct geometric parameters for designing hydrocyclones. G. Q. Dai et al. (1999) evaluated several hydrocyclone models that were developed previously. Their work concluded that a viable research of a hydrocyclone should consider certain factors such as the pressure drop, particle cut size, grade efficiency and the flow split, which is the ratio of underflow to inlet mass flow rate. Zhao (2004) developed a theoretical model which could predict the pressure drop across the hydrocyclone. According to him, the four different components of the pressure drop were: pressure drop due to geometry of the inlet, wall friction, swirling flow, and the flow leaving from the overflow. The wall friction was responsible for the major part of the pressure drop and was proven by several experimental studies. The model was established for studying single phase flows only, so the application of this model was not suitable for many industries as many industrial hydrocyclones are based on multi-phase flow.

Besides the theoretical studies, researchers also used experiments to investigate and validate optimum dimensions of hydrocyclones. Young et al. (1994) conducted an experiment to search for optimized oil-water separation hydrocyclones. Several operational variables, including inlet size, cylindrical diameter and straight section dimensions, etc., were chosen in this study. After that they tested the parameters respectively on the experimental hydrocyclone in which the various dimensions of the hydrocyclone could be changed gradually, so that the optimum design could be found.

However, this type of experiment, measuring only "global" or macroscopic flow characteristics, is quite anecdotal, and cannot give a fundamental understanding of the physics at play within hydrocyclones, which means for a particular case, substantive tests still need to be conducted, which is quite time-consuming. In order to have a basic understanding about the flow field within the hydrocyclone, scientists and engineers began using advanced experimental methods for cyclone separator studies. A.J. Hoekstra et al. (1999) used the Laser-Doppler velocimetry method to study the turbulent, strongly swirling flow field in a gas cyclone separator. The water/glycerol solution was fed into a pressured air atomizer to provide the seeds in a mean diameter of 2 μm within the main flow line. The mean in time tangential and axial velocity components were measured in three different diameters of the vortex finder. The swirl distribution for the three different experiments showed the same type of vortex; that is the outer free vortex and a solid-body rotation at the core region. However, they also showed a dramatic increase in the maximum tangential velocity, measured below the vortex finder, which went from 1 to 2.5 times the inlet velocity as a result of the reduction of the vortex finder diameter. The smallest vortex finder gave the larger tangential velocity value than the vortex finders in larger sizes. Meanwhile, the maximum magnitude of axial velocity components increased as the diameter of vortex finder decreased. Another finding from this study was that the reduction of the spigot diameter contributed to the decrease of the diameter of inner vortex core, which resulted in an increase in the tangential velocity.

More recently, Bai (Bai et al. 2009) used a two-component laser Doppler velocimeter to measure the axial and tangential velocity, as well as the fluctuation velocity, in a 35 mm diameter de-oiling hydrocyclone. Air core development was reported in their results when the inlet flow rate was more than 2.00 m^3/h and in this case, the measured fluctuation velocities were greater than running without air core. They indicated that the significant role of the air core in the hydrocyclone was that it created more turbulent fluctuations. They also concluded that the turbulence fluctuations near the inner core were a disadvantage to separation because they could make an oil droplet, which had already been separated and in the inner vortex, return to oily wastewater again. Another conclusion was that the axial and tangential velocity magnitude are dependent on the inlet flow rate but that the inlet flow rate does not change the flow character. However, Bai notes that it is possible that instead of the air core being the cause of the increased turbulence quantities, that perhaps the cause was the increase in inlet velocity, and that the association between decreased separation efficacy and air core presence may not be valid.

The computational fluid dynamic (CFD) modelling of cyclones, specifically the turbulence modeling is also an important task. Accurate turbulence field prediction will lead to more accurate prediction of the velocity and pressure field. Due to the internality of k–ε models, where the turbulence is treated as isotropic, only one scalar velocity fluctuation is modeled. Ma et al. (2000) has proved that k–ε model are not a good choice for turbulence calculations of hydrocyclones. Similar results could also be found in other studies, such as Petty and Parks (2001).

The Differential Reynolds Stress model (DRSM) is a powerful numerical model that was used to study the turbulence characteristics of hydrocyclones. Specifically, the full DRSM method has been used in more recent work. Slack et al. (2000) and Brenan et al. (2003) have used this model as a numerical study method for hydrocyclones. Good predictions in gas cyclones have been achieved, but when simulating solid-liquid (slurry fed) hydrocyclones, which typically have a distinct air core present, this method might not be appropriate.

More and more physical and mathematical models which are more appropriate for hydrocyclones were integrated into some commercial software and more accurate simulations are becoming possible due to the increased performance of the modern computer, which results in immensely decreased computational costs. Dlamini (2005) was able to set up a simulation of a single-water-phase only hydrocyclone in the commercial CFD code Fluent v6. A three dimensional hydrocyclone geometry with a tangential rectangular inlet was used in this study. The inlet velocity boundary condition type was specified with an inlet velocity as 2.28 m/s. The Reynolds Stress Model was selected as the turbulence model in the simulation. The velocity profile and pressure profile were predicted and then compared to the available data in the literature. The turbulent kinetic energy per unit mass was also predicted by the simulation and different shapes of the tangential inlet were modeled, and a comparison was made between circular and rectangular inlets. The result showed that the turbulent kinetic energy will be less with a rectangular inlet as compared to a circular inlet. In this simulation, it was attempted to artificially develop an air core by introducing air as part of the feed stream from the tangential inlet so that the air core was developed in the negative core pressure area. However, the numerical solution resulted in an extremely unstable air core, and it also exhibited divergent behavior. Some of the observations made in this thesis indicate that the air core is made up of air which enters the cyclone from the underflow, and as such, the aforementioned numerical issues when attempting to simulate an air core in this manner are not un-expected.

Bhaskar et al. (2007) also conducted a validation study between CFD simulations and experiments for a hydrocyclone. Their initial work included the comparison of experiments and CFD simulated results using three different types of turbulence models: standard k–ε, k–ε RNG, and RSM. Parametric changes in the spigot in the experiment indicated that contracting the spigot opening increased the upward vertical velocity of flow more when compared to the decrease in the downward velocity. With the increase in the feed pressure, the static pressure radial gradient was increased within the cyclone body and hence more flow split into the overflow. Their data also verified that an increase in the inlet pressure has also increased the tangential velocity.

In further studies, the phenomenon of the air core development has caused extensive concerns and has been observed in many experiments. The prediction of air core diameter and shape by numerical modeling has become a major direction in this field. A number of scientists and engineers tried to develop a numerical method to describe the flow pattern inside cyclones and to make accurate predictions for the air core. Dyakowski and Williams (1995) have focused on this problem and tried to find an answer. Despite the limitation in computer performance at that time, they presented a new mathematical method to solve the conservation equations. The effect of bulk viscosity, surface tension and flow conditions were taken into account, and the relation between slurry mixture viscosity and the air core diameter was computed, that is, increasing the viscosity would reduce the diameter of the air core. In M. Narasimha's research (2006), the large eddy simulation (LES) turbulence model and volume of fluid (VOF) model were used. The LES model led to an improved prediction when compared to DRSM, and they concluded that a transport effect is the dominating factor in the air core development. They also mentioned that the air core diameter would be reduced as the viscosity of liquid increases when the feed velocity is constant. As can be seen from the literature review, all of the previous experimental work focused on extremely simplified and/or scaled down geometries in comparison to actual milling circuit hydrocyclones.

1.4 Objectives

From the literature review, a better understanding of hydrocyclone flow dynamics should be developed using advanced experimental and numerical methods. The objectives of this study include investigating the two-phase fluid flow inside a geometrically realistic (in both features and scale) model hydrocyclone, with an air core present, using Particle Image Velocimetry (PIV) and validating CFD results obtained by using a commercial CFD package, Star CCM+.

CHAPTER 2

THEORETICAL BACKGROUND

2.1 Governing Equations

The principal consideration for any theoretical study of liquid progression, is the governing equations. The flow field inside a hydrocyclone when an air core is formed is considered unsteady. The representing partial differential equations are the continuity equation and the Navier-Stokes conditions: (Bhaskar et al., 2006)

$$\frac{\partial \rho}{\partial t} + \rho \frac{\partial \bar{u}_i}{\partial x_i} = 0 \qquad (2.1)$$

$$\frac{\partial (\rho \bar{u}_i)}{\partial t} + \frac{\partial (\bar{u}_i \bar{u}_j)}{\partial x_j} = -\frac{\partial \bar{P}}{\partial x_i} + \frac{\partial}{\partial x_j}\left(\mu \frac{\partial \bar{u}_i}{\partial x_j}\right) + \frac{\partial}{\partial x_j}\left(-\rho \overline{u_i' u_j'}\right) + \rho g_i \qquad (2.2)$$

Where ρ is the density, P is the pressure, and μ is the dynamic viscosity of the fluid. $\rho \overline{u_i' u_j'}$ is the Reynolds stress term that includes the turbulence closure, which is modelled in order to close the equations. In the above equations, the velocity u_i has been decomposed into two different components: mean and fluctuating velocity, as shown in figure 2.1. This formulation was introduced by Reynolds (1985):

$$u_i = \bar{u}_i + u_i' \qquad (2.3)$$

2.2 Turbulence

The flow patterns inside the hydrocyclone are of highly swirling behavior, therefore it is important to precisely describe the turbulent behavior of the flow. Flow types are defined by the magnitude of Reynolds number. Flows having Reynolds number over 5000 are considered turbulent. Due to the turbulent nature of the flow inside a hydrocyclone, the flow properties change rapidly. Turbulence is characterized by the following features (Tennekes & Lumley, 1972):

- **Irregularity**: Turbulence requires application of statistical methods.
- **Diffusivity**: Key characteristic for Industrial applications.
- **Large Reynolds Numbers:** As the Reynolds number increases, the flow becomes more unstable, which eventually leads to turbulence.
- **Rotationality**: turbulent flows have non-zero vorticity and have a three dimensional vortex generation mechanism.
- **Non-dependency on fluids:** The general features of turbulence depend on the flow itself rather than the molecular properties of certain fluids.
- **Dissipation**: It is the rate of conversion of kinetic energy into internal energy occurring rapidly under the effects of the viscous shear stresses.

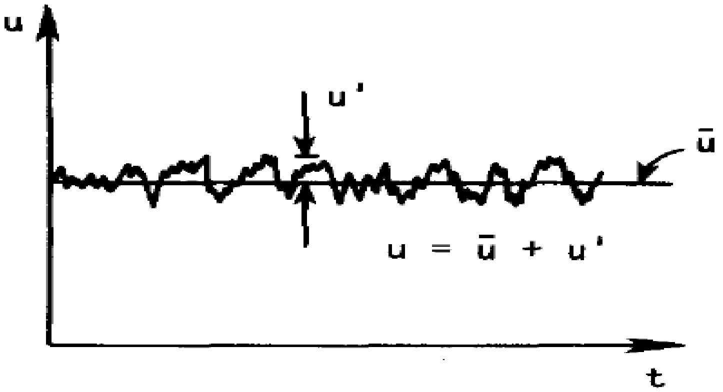

Figure 2.1 The velocity is decomposed into two components: $\bar{u}$ is the mean velocity component, and u' is the fluctuating velocity component (Tannehill, 2011).

2.2.1 Turbulence Models

With the increase in the use of computer technology and performance, researchers were able to develop new turbulence models which would be used in predicting the flow field inside a hydrocyclone, such as the standard k-ε model, RNG k-ε model, Reynolds Stress models, etc. The k-ε model and RSM have achieved some degree of success in modeling hydrocyclones. Although the Large Eddy simulation (LES) is relatively new to hydrocyclone studies, it has also obtained some degree of success (Narasimha et al, 2006). The LES model is by far the most sophisticated model, capable of most accurately modeling the true nature of the flow field, however, it is also extremely computationally expensive, requiring much finer meshes and shorter time steps.

2.2.1.1 The k-ε Model

The k- ε turbulence model is based on the mechanisms that affect the turbulent kinetic energy. The assumption of the model is that the turbulent viscosity is isotropic in nature. It states that the ratio of the Reynolds stress and the mean rate of deformations is same in all directions.

The “k” in this model represents the turbulent kinetic energy, which is used to compute the turbulent velocity scale. The “ε” is the dissipation rate. The main reference described here is from Versteeg et al. (2007). The momentum equation is written as:

$$\frac{\partial \rho u_i}{\partial t} + \frac{\partial \rho u_i u_j}{\partial x_j} = \frac{\partial p'}{\partial x_i} + \frac{\partial}{\partial x_j} \mu_{eff} \frac{\partial u_i}{x_j} \qquad (2.4)$$

Where μ_{eff} is the turbulent effective viscosity and can be calculated from turbulent viscosity μ_t from the following equation:

$$\mu_{eff} = \mu + \mu_t \qquad (2.5)$$

Where p' is the modified pressure which can be computed by:

$$p' = p + \frac{2}{3}\rho k \qquad (2.6)$$

The model assumes that turbulent viscosity is calculated from turbulent kinetic energy and dissipation rate via the equation:

$$\mu_t = \rho c_\mu \frac{k^2}{\varepsilon} \qquad (2.7)$$

Where c_μ is a constant. The value of k and ε come directly from the differential transport equations for the turbulent kinetic energy and turbulence dissipation rate.

According to the nature of the model, when a flow contains anisotropic turbulence, it is not a suitable turbulence model. As such, current study will focus on both RSM and LES models, both of which can model anisotropic turbulence.

2.2.1.2 The Reynolds Stress Model

The k-ε model concentrates on isotropic turbulence, therefore it has disadvantages when it is used to describe the multi-phase flow in hydrocyclones which has anisotropic turbulence. RSM can account for the anisotropy of turbulence and gives good results for swirling flows. It is considered to be the most relevant model for hydrocyclone study (Brennan, 2006). In the RSM, the transport equation is written as:

$$\frac{\partial}{\partial t}\left(\rho \overline{u_i' u_j'}\right) + \frac{\partial}{\partial x_k}\left(\rho u_k \overline{u_i' u_j'}\right) = D_{ij} + P_{ij} + \pi_{ij} + \varepsilon_{ij} + S \qquad (2.8)$$

Where the left first term is the local time derivative of stress and the second term is the convective transport term. The right five terms are:

The stress diffusion term: $D_{ij} = -\frac{\partial}{\partial x_k}\left[\rho\overline{u_i'u_j'u_k'} + (\overline{p'u_i'})\delta_{jk} - \mu\left(\frac{\partial}{\partial x_k}\overline{u_i'u_j'}\right)\right]$

The shear production term: $P_{ij} = -\rho\left[\overline{u_i'u_k'}\frac{\partial u_j}{\partial x_k} + \overline{u_j'u_k'}\frac{\partial u_i}{\partial x_k}\right]$

The pressure-strain term: $\pi_{ij} = p\,\overline{\left(\frac{\partial u_i'}{\partial x_j} + \frac{\partial u_j'}{\partial x_i}\right)}$

The dissipation term: $\varepsilon_{ij} = -2\mu\overline{\frac{\partial u_i'}{\partial x_k}\frac{\partial u_j'}{\partial x_k}}$

The source term: S

The main reference to the RSM model here is provided by Wang et al. (2006).

2.2.1.3 Large Eddy simulation

The large eddy simulation technique was developed based on an implication from Kolmogorov's theory of self-similarity that the large eddies of the flow are dependent on the geometry while the smaller scales are more universal Jayaraju(2009). Hence, the large three-dimensional eddies which are dictated by the geometry and boundary conditions of the flow are directly calculated whereas the small eddies which tend to be more isotropic are modeled. The LES technique is based on separation between large and small scales. These scales that are of a characteristic size greater than the grid size are called large or resolved scales, and others are called small or sub grid scales.

Unlike Equation 2.3, the velocity now is decomposed into the resolved component $\overline{u}_i$ and the residual component $\overline{u}_i'$, and the equation is given by:

$$u_i = \overline{u}_i + \overline{u}_i' \qquad (2.9)$$

The resolved component is obtained by applying a filtering operation to the governing Navier-Stokes equations. The final LES model equations are given below:

$$\frac{\partial \rho}{\partial t} + \rho \frac{\partial \bar{u}_i}{\partial x_i} = 0 \qquad (2.10)$$

$$\frac{\partial (\bar{u}_i)}{\partial t} + \frac{\partial (\bar{u}_i \bar{u}_j)}{\partial x_j} = -\frac{1}{\rho}\frac{\partial \bar{P}}{\partial x_i} + \frac{\partial}{\partial x_j}\left(\mu \frac{\partial \bar{u}_i}{\partial x_j}\right) + \frac{\partial}{\partial x_j}\left(-\frac{\partial \tau_{ij}^{sgs}}{\partial x_j}\right) + g_i \qquad (2.11)$$

Where τ_{ij}^{sgs} is the residual stress tensor that arises from the residual motions, and it can be defined as:

$$\tau_{ij}^{sgs} = \overline{u_i u_j} - \bar{u}_i \bar{u}_j \qquad (2.12)$$

Yakhot et al. (1989) introduced the renormalization group model (RNG), which is effective to model the low-Reynolds-number effects in the near-wall regions, in order to improve the LES results, because the LES method was previously not well defined to solve the flow near the walls.

2.3 Fluid and Particle Velocity Distributions in a Hydrocyclone

The velocity profile has three components inside a hydrocyclone. The tangential velocity v_θ is considered the most important component and it has been studied extensively (Whitby and Peterson, 1965). The others are the axial velocity, v_x and radial velocity, v_r. The three components have been analyzed independently in the past (Elsayed, 2011). The flow patterns and relationships have been established experimentally by Kelsall (1952) and Bradley (1965), which were substantiated with the help of computational fluid dynamics by Pressdee (1989).

2.3.1 Tangential velocity

The tangential velocity has the highest magnitude of all the components in a hydrocyclone flow (Kelsall, 1952). Due to the tangential inlet, a high value of centrifugal force is generated which acts on the suspended particles (either solid or droplet) that causes separation. Hence the tangential velocity plays a vital role in the separation process inside a hydrocyclone. Figure 2.2 shows the tangential velocity distribution, based on the studies of Kelsall (1952).

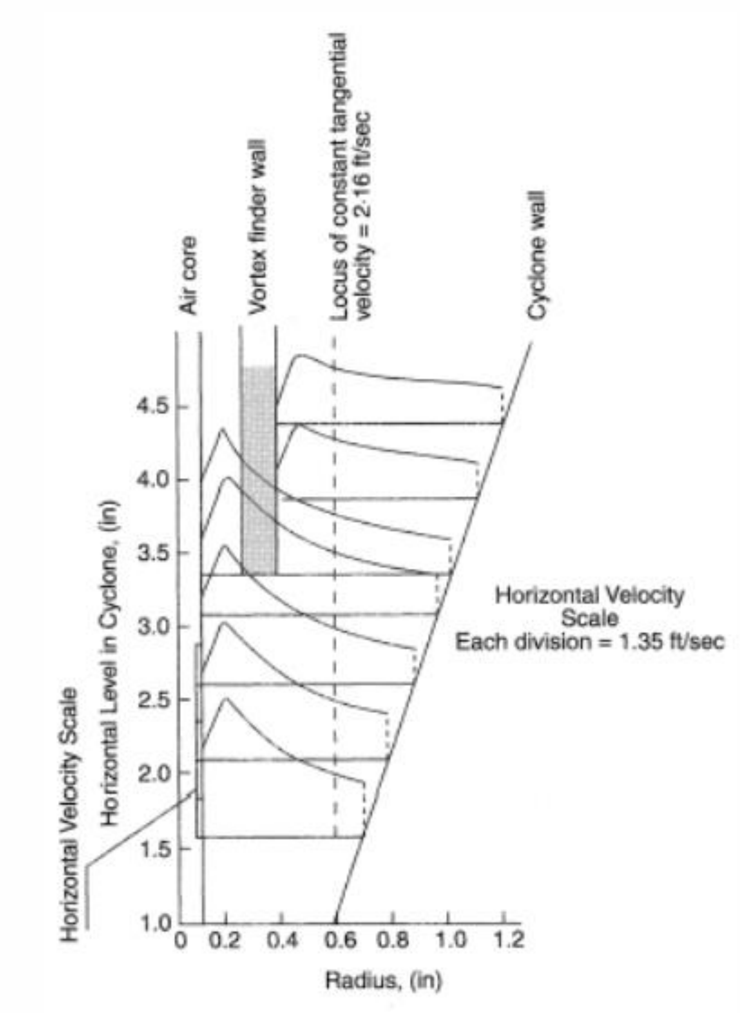

Figure 2.2 Tangential velocity distribution (Kelsall, 1952)

In the outer vortex, the tangential velocity is inversely proportional to the radius of the hydrocyclone, hence it increases as the radius in the conical part of the hydrocyclone decreases. The conservation of angular momentum is not constant since there are energy losses inside the hydrocyclone. Therefore the following equation is used to describe a relation between the tangential velocity and the cyclone radius. (Wen-Ching Yang, 2003)

$$V_\theta R^n = constant \qquad (2.13)$$

Where 'V_θ' is the tangential velocity and 'R' is the radius of rotational flow and 'n' is typically between 0.5 and 1. This relationship is only true when an air core is formed in the middle of the cyclone.

2.3.2 Axial Velocity

Axial velocity determines the proportion of mas flow rates through the overflow and the underflow. The fluid motion near the axis of the cyclone is in the upward direction (axially towards the vortex finder), while near the wall it is in the downward direction (towards the underflow). The axial velocity distribution is shown in Figure 2.3 as per studies performed by Bradley (1965).

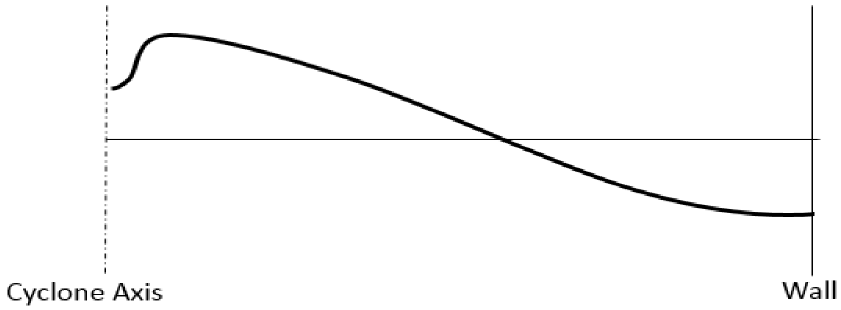

Figure 2.3 Radial distribution of the axial velocity in a gas cyclone (Bradley, 1965)

As illustrated in the figure, the axial velocity becomes zero at a certain point between the cyclone axis and wall. This point is called as the "locus of zero axial velocity," which was introduced by Bradley (1965). Figure 2.4 shows the locus of zero axial velocity in a hydrocyclone, which occurs at the location of maximum tangential velocities (the interface between the inner and outer vortices) within a hydrocyclone.

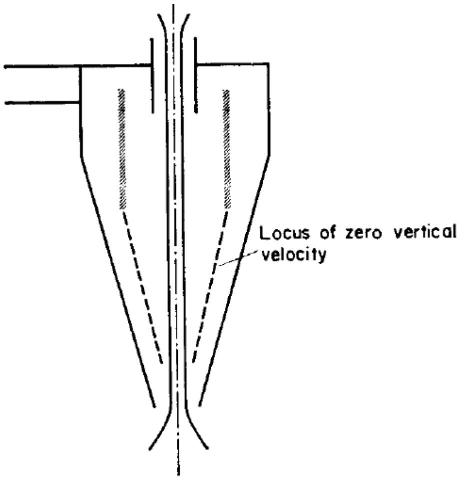

Figure 2.4 Sketch of the locus of zero axial velocity in a cyclone (Bradley, 1965)

2.3.3 Radial Velocity

Radial velocity has the smallest magnitude compared to tangential and axial velocity. This does not mean that it is of least importance since it provides the solid particles with larger residence time so that they can be separated. Since the magnitude of the radial velocity is much smaller than the tangential and axial velocity, it can assumed negligible near the wall and be uniform in the control surface. The following equation can be used for computing the radial velocity.

$$v_r = \frac{\mathrm{Q}}{\pi\, \mathrm{D_x H_{CS}}} \qquad (2.14)$$

Where v_r is the mean radial velocity, D_x is the diameter of the control surface which is equal to the diameter of the vortex finder, H_{CS} is the height of the control surface, and Q is the volumetric flow rate. As stated by Hoffman (2007), it is difficult to measure the radial velocity magnitude correctly due to the small magnitudes however he suggested in his studies that it is usually directed towards the inside of the vortex tube below its opening due to secondary flows.

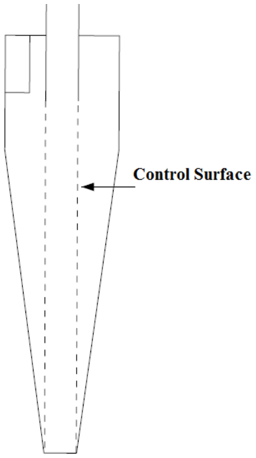

Fig 2.5 Sketch of the control surface of the cyclone

2.4 Particle Motion

A multi-phase flow inside a hydrocyclone, especially, one with the solid-liquid interaction is complicated. The particles injected through the tangential inlet have two forces acting upon it: the centrifugal force which pushes them towards the hydrocyclone wall; while the radial drag force pulls them inward. The equilibrium orbit theory states that the particles that enter the inner swirl are discharged from the overflow, while the particles in the outer swirl are discharged from the underflow. Dai et al. (1999) used a particle dynamics analyzer (PDA) to measure the radial and axial solids velocity components and also the size of solid particles in a hydrocyclone. An important observation was made during the experiments: some of the particles from the inner swirl moved into the outer swirl and got discharged from the underflow. This phenomenon is called a recirculating load. Due to this the equilibrium orbit theory has to be modified, and should only be considered the idealized case.

The centrifugal force is proportional to the particle mass (proportional to diameter cubed) while the drag force is proportional to the diameter squared of the particles as given by Stoke's law. Therefore, the size and mass of the particles are the most significant parameters for particle separation and the larger and denser particles are much more easily separated from the flow in a hydrocyclone.

2.5 Air Core Formation

It is observed in a hydrocyclone system, when the outlets are open to atmosphere, an air core is formed. Air core generation is a remarkable feature and as such it has received extensive attention by both experimental and CFD works. The factors affecting the size of the air core are: geometrical characteristics of hydrocyclones, the feed flow rate, and the viscosity, surface tension, and density of the liquid. The formation of an air core is a transport effect rather than a pressure effect, therefore the feed flow rate is regarded as the major factor. Viscosity also constitutes to the changes in the dimension of the air core. Rietema (1961) claimed that the existence of air core reduces the pressure drop and thus reduces the operation costs of the hydrocyclone. Having an air core present also prevents cavitation from occurring within the cyclone.

The low (negative) pressure field along the central axis of the hydrocyclone is the component of an air core. In experiments, when the underflow outlet is exposed directly to the atmosphere, the atmospheric pressure pushes the air into the hydrocyclone through the underflow and forms the air core along the central axis of the hydrocyclone, where it slowly exits the cyclone through the overflow. That is, there is continuous flow of air in through he underflow, through the air core, and out through the overflow. Even in conditions when an isolated system (isolated from atmosphere by submerging the overflow and underflow), a sub-vapor pressure region is formed due to accumulation of the dissolved gases present in the flow, along the central axis, which generates a gas core (Wang, 2009). According to the energy transfer considerations, the air core development is a result of the static pressure energy of liquid being unable to compensate for the loss of energy as a result of the centrifugal force-created radial pressure gradient (Bai, 2009). This study concluded that the velocity varies a lot (temporarily) near the core and hence the air core presence is a disadvantage due to the turbulence fluctuations that might make the finer particles move back to higher radii. However, without sufficient experimental and numerical studies, the role of the air core will still remain unknown- that is to say, the presence of the air core may not be the reason for increased turbulent kinetic energy near the center of the cyclone. Hence it is vital to employ computational and experimental techniques to obtain more insight. Due to the swirling flow present inside the hydrocyclone, the development of air core is unavoidable in field applications. All mining hydrocyclones have their underflow open to atmosphere, which leads to formation of air core and hence, study of the air core is required.

CHAPTER 3

VOLUMETRIC CONCENTRATION OF AIR

As suggested by Ke (2016), the numerical simulation can generate a more accurate output if the amount of air being introduced into the hydrocyclone could be computed. This is achieved by installing a U-loop pipe section to the overflow of the hydrocyclone and by using a SONARtrac flow meter in order to obtain the volume concentration of air in the overflow pipe.

3.1 SONARtrac

The SONARtrac VF-100 model used in this experiment is a passive flow meter that provides accurate and repeatable volumetric flow measurements for dirty liquids and slurries. The unit contains three essential parts: a sensor band, an environmental enclosure, and transmitter. The sensor band is a wrap-around mesh structure that measures volumetric flow rate by combining turbulent eddies' phase and frequency components as they pass through. By measuring the speed of acoustic waves passing through the mesh, the amount of air entrapped can be correlated to the phase fraction of the two component mixture. These readings are displayed on the transmitter, which features a digital signal processor. The environmental enclosure protects the mesh from damage during handling (*SONARtrac Flow Measurement*). The SONARtrac was installed according to the manual provided by CIDRA, the sensor band had to be aligned with the flow direction, and the position of the band is 10 times the diameter of the pipe from the elbow and 5 times the diameter away from the next elbow. The SONARtrac was also used to measure the percentage by volume of air with water as the test fluid and also with NaI solution.

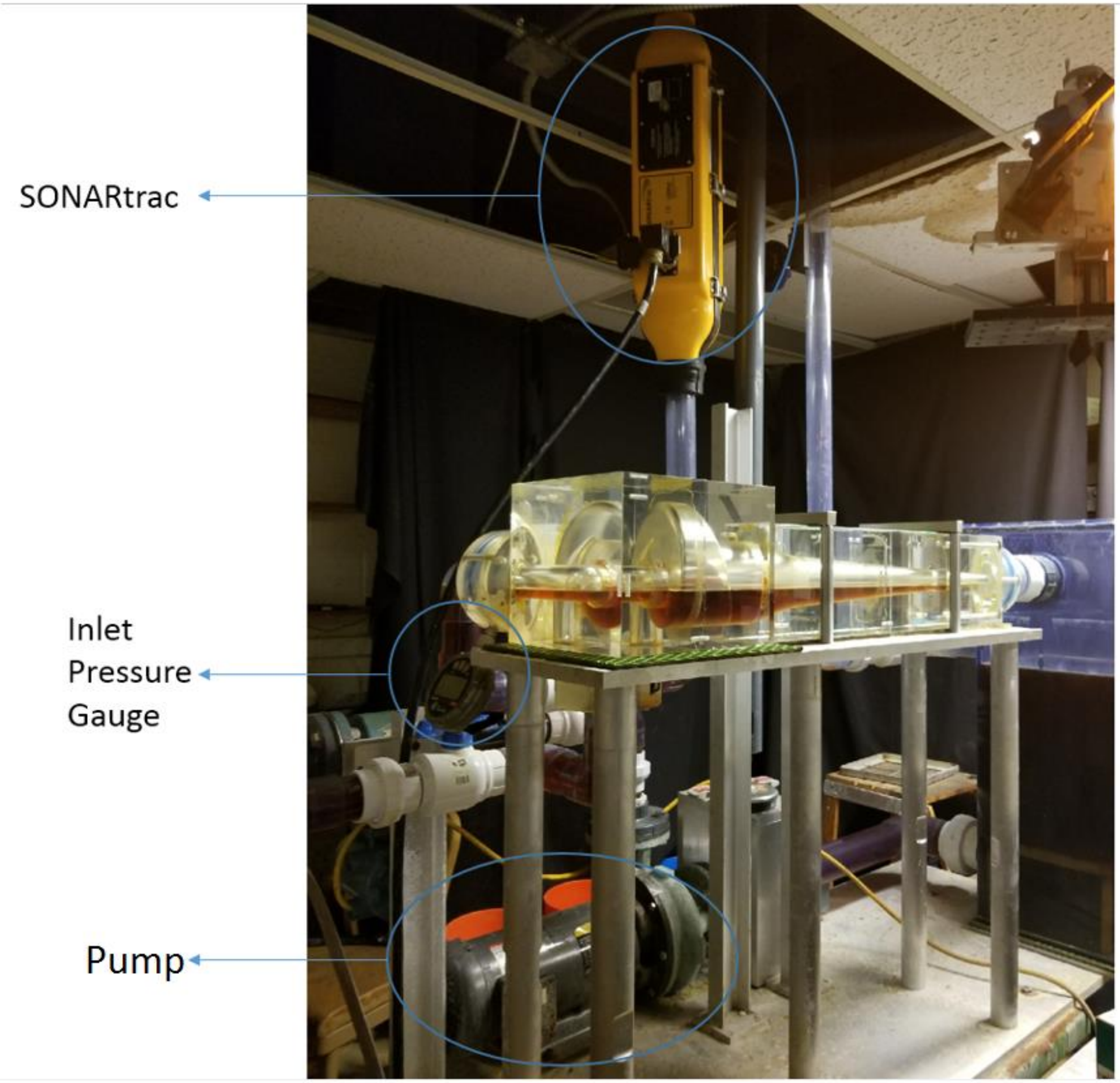

Figure 3.1 Experimental setup

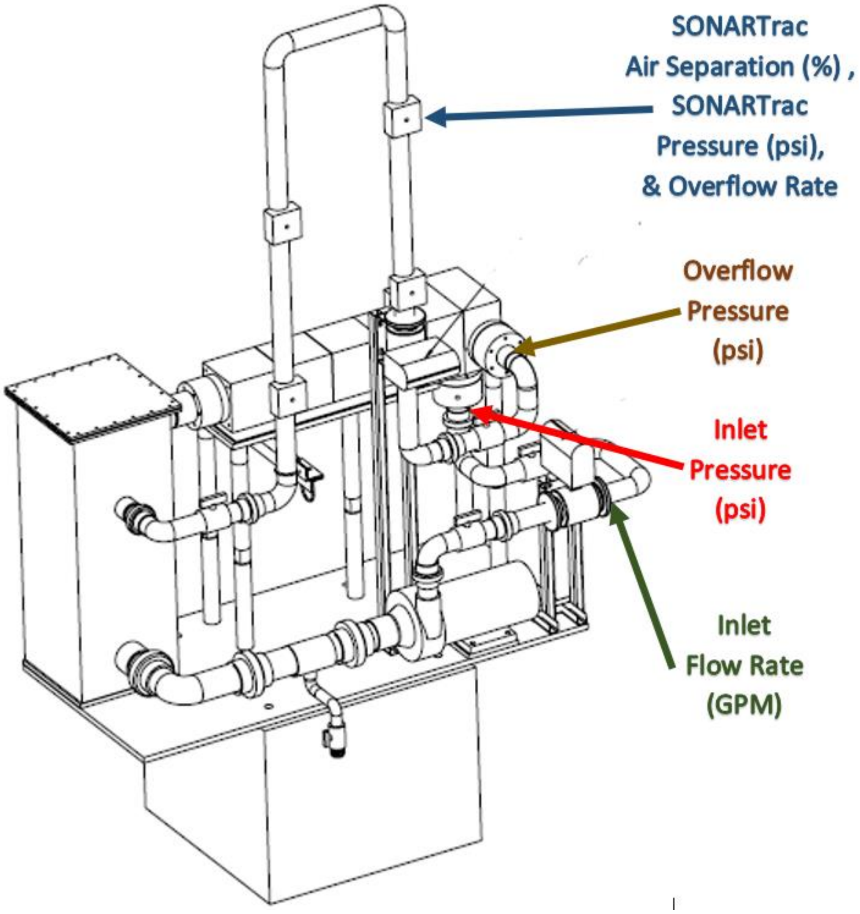

Figure 3.2 SONARtrac location in the U-loop pipe section

3.2 SONARtrac Data

3.2.1 Experimental Procedure

The SONARtrac is used to measure the percentage of air by volume in the overflow U-loop pipe section. At first, the VFD frequency speed is set to 30 Hz so that the NaI solution is able to fill the U-Loop completely and eliminate all of the air pockets in the U-loop pipe section. Then the VFD frequency is turned down to 20 Hz which is the working speed for the PIV experiments. The line pressure at the SONARtrac location has to be entered for every CFD frequency into the control panel of the SONARtrac. The system is kept running for about 5 minutes until the flow stabilizes and a uniform mixture of air and NaI solution is seen in the overflow pipe section. Due to variable air entrainment in the overflow pipe section, the SONARtrac is not able to measure a static value for the percentage of air by volume at a pump speed of 20 Hz. As such, the readings are taken over the span of 10 minutes. A total number of 20 readings are taken at each VFD frequency value from 20 Hz to 60 Hz. Next, the numerical average is taken and is considered the value of percentage air content for the respective VFD frequency value. At each VFD frequency value/inlet flow rate, the static line pressure at the SONARtrac location has to be entered into the SONARtrac controller. Each static line pressure at the SONARtrac location was measured in a separate set of tests, where the inverted U loop was turned backwards, so that the pressure gauge is in the same location as the SONARtrac measurements are taken (i.e. in the vertical up-leg of the inverted U loop).

3.2.2 NaI Solution

The following tables shoes the data collected using the SONARtrac. A correction is made using the ideal gas law in order to calculate the percent air by volume at the overflow outlet from the % air measured at the SONARtrac location in the inverted U loop, knowing the measured pressures at each of those two locations which have been measured with pressure gauges.

Pump Motor Speed (Hz)	Inlet Flow (GPM)	Overflow Flow (GPM)	Inlet Absolute Pressure (Psi)	Overflow Absolute Pressure (Psi)	SONARtrac Absolute Pressure (Psi)	Pressure ratio	Average Air by volume (%)	Corrected Air By volume (%)	Error (%)
25	38.6	37.68	17.35	15.72	12.72	0.809	0.715	0.579	0.2
30	46.8	45.58	18.69	16.17	12.85	0.795	1.284	1.020	0.13
35	54.6	53.53	20.03	16.82	13.06	0.776	1.998	1.551	0.13
40	61.4	59.70	21.71	17.32	13.22	0.763	2.422	1.849	0.11
45	68	65.95	23.4	18.05	13.37	0.741	2.748	2.035	0.045
50	74.5	72.55	24.72	18.78	13.55	0.722	3.019	2.178	0.043
55	81.3	79.00	27.59	19.61	13.72	0.700	3.175	2.221	0.035
60	88.2	87.13	30.26	20.06	14.08	0.702	3.263	2.290	0.033

Table 3.1 Experimental data collected for NaI solution

At VFD frequency of 20 Hz, the flow velocity is not high enough to create enough turbulence to break up the air, and large continuous air slugs and bubbles are present in the vertical pipe. The SONARtrac requires that the air is sufficiently well mixed with the liquid in order to get accurate measurements, and so the measurement at 20 Hz is not considered accurate. As such, the 20 Hz air content at the overflow outlet was interpolated from the measured data at higher flow rates. The LINEST function in MS Excel was used to develop the following fourth degree polynomial from 25-60 Hz readings and interpolated to approximate a corrected average separation percentage for 20 Hz VFD frequency.

$$S_{corr,NaI} = 0.00000258 * f^4 - 0.000419 * f^3 + 0.0228 * f^2 - 0.421 * f + 2.368$$

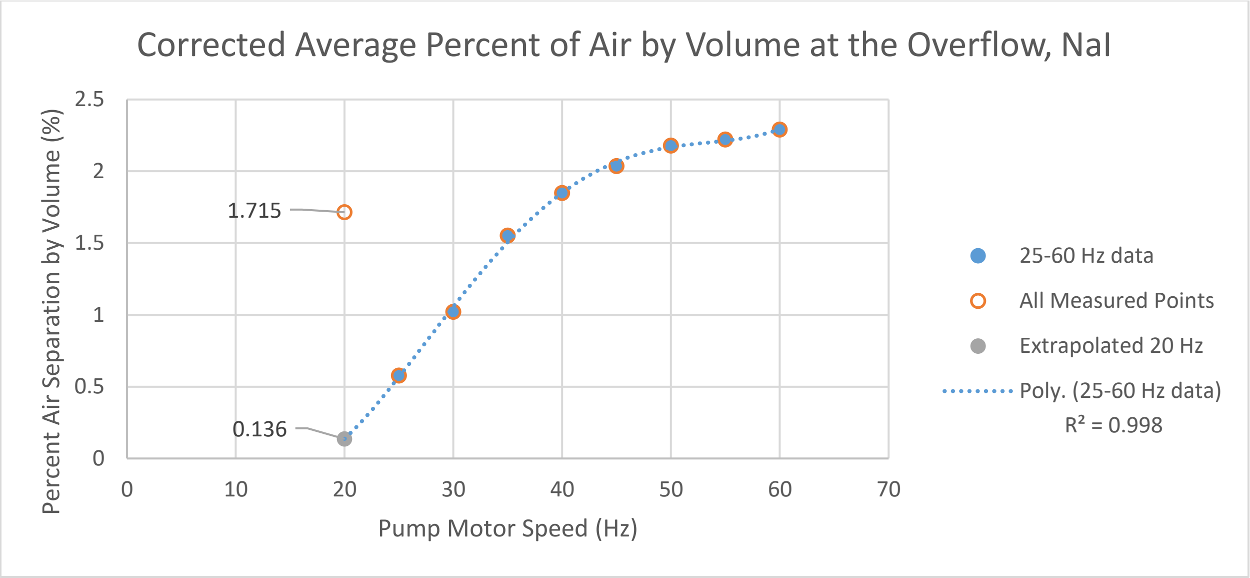

Figure 3.3 Interpolation graph for computing the % air content (volumetric) value at 20 Hz VFD frequency for NaI solution

The value for interpolated, corrected average volumetric concentration of air as a percent for 20 Hz comes to 0.136%. As expected, increasing pump speed leads to higher air concentrations in the hydrocyclone overflow. At higher VFD frequencies from 40 Hz to 60 Hz, a large amount of air is seen entering the hydrocyclone through the inlet, since the filter floss in the tank becomes in-effective at such high flow rates, and large quantities of air are observed going both through and around the filter floss, and into the cyclone. Hence the values of the % air contents measured from 40 Hz to 60 Hz may be higher than they would have been had there been no air going in through the cyclone inlet, as is the case in the field. There is however a good degree of confidence in the % air content readings from 25-35 Hz, which are used to interpolate the 20 Hz point, which is the speed at which the PIV data was taken. It should be noted that although the flow field is not stable enough for measurements in the vertical up leg of the U loop, the flow within the cyclone itself is stable at 20 Hz. Hence, use of the interpolated % air content seems reasonable, as does CFD modeling of the hydrocyclone at the inlet flow rate corresponding to 20 Hz.

3.2.3 Water

Below is a summary of flow data collected for the water-air case. Average percent air content at the overflow outlet for all recoded values are given here.

Pump Motor Speed (Hz)	Inlet Flow (GPM)	Overflow Flow (GPM)	Inlet Absolute Pressure (Psi)	Overflow Absolute Pressure (Psi)	SONARtrac Absolute Pressure (Psi)	Pressure ratio	Average Air by volume (%)	Corrected Air By volume (%)	Error (%)
25	41.8	40.4	16.515	15.42	13.797	0.895	0.782	0.639	0.21
30	50.3	48.5	17.357	15.73	13.988	0.889	0.849	0.967	0.27
35	58.0	56.3	18.342	16.12	14.214	0.882	1.528	1.347	0.25
40	67.1	64.6	19.467	16.57	14.461	0.873	2.001	1.746	0.12
45	75.6	72.6	20.728	17.06	14.752	0.865	2.253	1.948	0.035
50	83.9	80.9	22.264	17.64	15.067	0.854	2.392	2.043	0.063
55	92.2	88.7	23.773	18.21	15.358	0.843	2.489	2.099	0.061
60	100.2	98.0	25.504	18.87	15.751	0.835	2.517	2.101	0.066

Table 3.2 Experimental data collected for Water

Just like NaI solution, the LINEST function in MS Excel was used to interpolate 25-60 Hz data. The interpolated volumetric percent air at the overflow outlet was found for 20 Hz VFD frequency was found using the polynomial given below.

$$S_{corr,H20} = -0.0000482 * f^3 + 0.00468 * f^2 - 0.0803 * f + 0.451$$

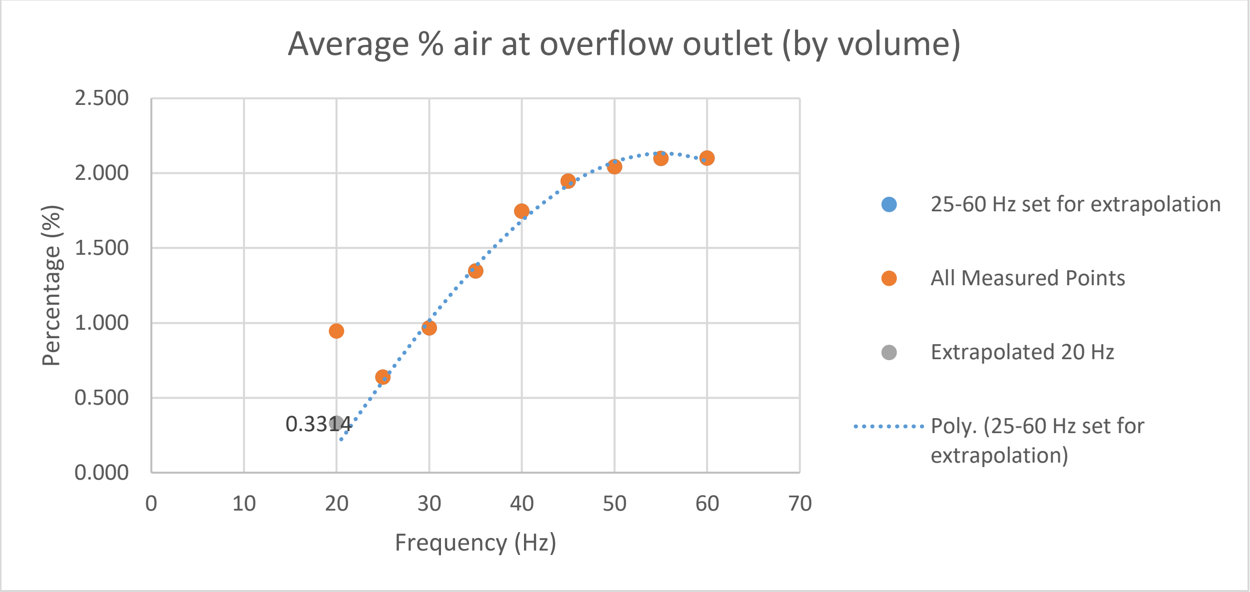

Figure 3.4 Interpolation graph for computing the % air content through the overflow at 20 Hz VFD frequency for water

The value for interpolated, corrected average volumetric concentration of air as a percent for 20 Hz comes to 0.331% with the percent separation of air leveling off near 50 Hz VFD frequency. Similar to the NAI curve seen in Figure 3.3, the water data shows the air content increasing relatively quickly with increases in inlet flow rate, and then leveling off to plateau at a value of just over 2 % by volume. When running on water, micro bubbles were not an issue, and the water was injected into the cyclone inlet with no air content present. Hence the fact that the water data also shows a plateau of % air content vs. inlet flow rate in Figure 3.4 indicates that the same phenomena seen in Figure 3.3 is likely not due to the air coming in through cyclone in let at high inlet flow rates, and that the plateau observed for the NaI data is likely a phenomena that would still be present had the NAI liquid solution been injected with no air in the inlet stream, as is the case with cyclones in the field (i.e. there is no air present in the inlet stream).

CHAPTER 4

COMPUTATIONAL STUDY

In recent years, Computational Fluid Dynamics (CFD) has emerged as a viable tool for simulation of fluid mechanics and heat transfer systems by making use of numerical models. There exist many advanced commercial computational fluid dynamics software programs. Due to the advancements in the field of computer technology, the popularity of CFD among scientists and engineers has greatly increased. Software's like ANSYS Fluent and, CD-Adapco Star CCM+ have emerged through these developments and provide a huge variety of numerical models for simulations with higher calculation accuracy than ever before. The results obtained from performing CFD simulations have shown increased reliability and precision. This can be asserted by comparing the CFD results with experimental data. CFD also provides a simpler platform for obtaining solutions to non-linear partial differential equations, since obtaining the analytical solutions for the same is typically tedious or impossible.

In this thesis, the fluid field in a hydrocyclone was calculated and simulated numerically by using STAR CCM+ version 11.04.012, and the experimental PIV data was used to validate the computational results. The computational simulation in this project was performed for two-phase flow. The first phase was sodium iodide solution (63.3% NAI by weight), and the second phase was air. The data collected was in r-z plane of the hydrocyclone. Some experimental results obtained with a camera to look at the air core were also obtained on water.

4.1 The Geometry and Mesh Generation

In this computational study, a widely used industrial hydrocyclone geometry was imported to STAR CCM+ version 11.04.012. The mesh generation and numerical simulation process was performed using the built-in tools provided by the software package.

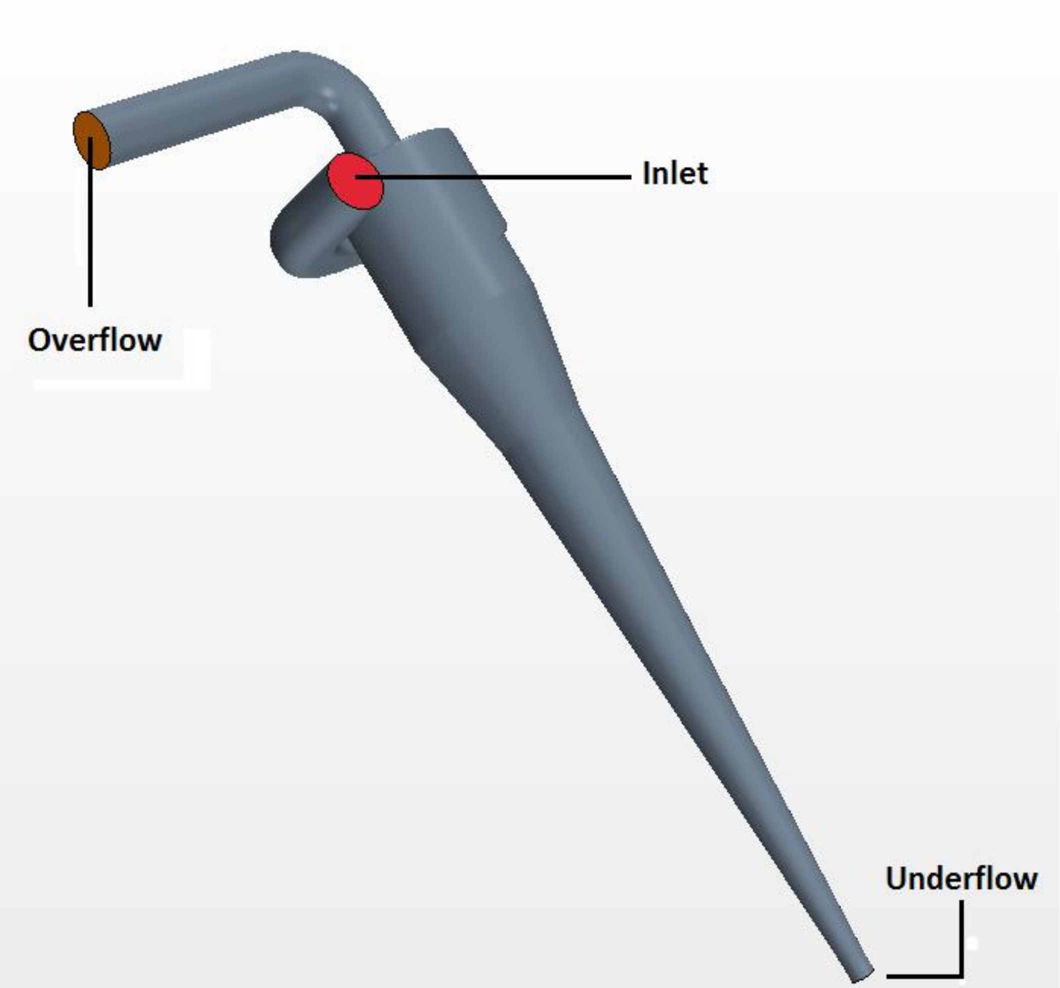

Figure 4.1 Hydrocyclone Schematic Model

Figure 4.1 shows the schematic model of a hydrocyclone. Figure 4.2 shows the drawing and indicates the important dimensions of the hydrocyclone. The table in Figure 4.2 shows the values of the hydrocyclone dimensions.

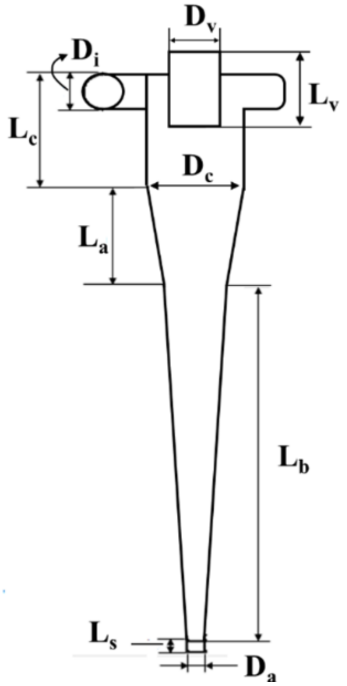

Notation	Parameter	Dimension (inch)
Dv	Vortex finder diameter	2.50
Lv	Vortex finder length	4.25
Di	Inlet diameter	2.03
Lc	Length of cylindrical section	7.1
Dc	Diameter of cylindrical section	6.3
La	Length of the first cone	5.65
Lb	Length of the second cone	20.61
Ds	Spigot diameter	0.88
Ls	Spigot length	0.62

Figure 4.2 Hydrocyclone geometric drawing and dimensions.

For generating the mesh: surface remesher, trimmer (hexahedral) mesh and the prism layer models were used. The overall quality of the surface meshes is improved by the use of the surface remesher. It also improves the overall specification on the geometry surface and achieves functions like edge proximity mesh control, local growth rate specification, etc.

The correct definition of the geometry boundary types plays a very important role in improving the mesh quality and hence, the increase of the accuracy as well as the reliability of the numerical results. Once the two-dimensional mesh generation has been finished, the trimmed cell mesher generates the entire volume meshes based on the surface meshes. The trimmer model has been proven as a robust and efficient mesh model, and it generates mostly hexahedral volume cells and minimize the cell skewness and also allows the refinement based on surface meshes.

In a hydrocyclone, pressure drop is always considered as an important performance parameter, so the correlated parameter, wall friction should be considered. Moreover, complex fluid fields are present near the geometry boundary, thus the higher density of volume mesh and higher accuracy near the boundary are required. Therefore, the prism layer model was applied.

The prism layers model is used with a core volume mesh to generate orthogonal prismatic cells next to a wall surface or boundaries and allows the solver to resolve near wall flow accurately with the use of wall functions, which is critical in determining flow features such as separation. It also provides better cross-stream resolution and reduces numerical diffusion near the wall.

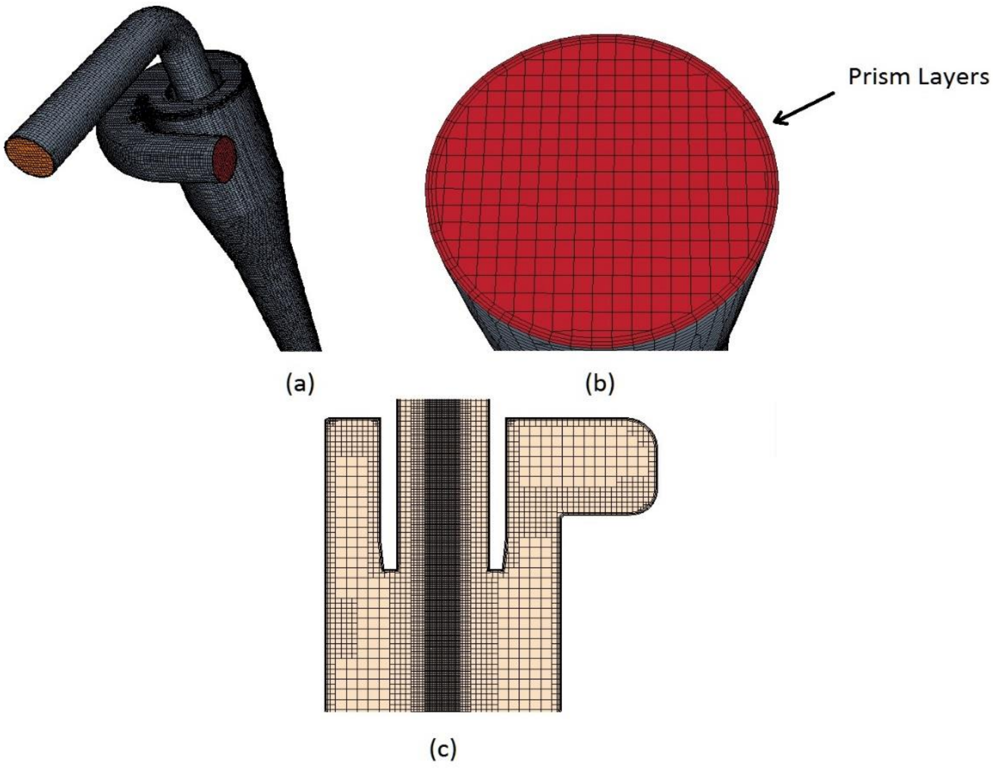

Figure 4.3 (a) Meshed hydrocyclone geometry, (b) Prism layers, (c) r-z plane.

Figure 4.3 illustrates the meshed model and prismatic layers near the wall. A total number of 1,170,205 hexahedral cell were generated, the number of prism layer is 3, and the thickness of the prism layer is 1.5 mm, the maximum skewness angle did not exceed 75 degrees, and the minimum cell aspect ratio was larger than 0.22. In order simulate air core formation in this work, the mesh size and density in the central area were intentionally increased such that the mesh can fully handle the complex flow field in the core area.

In simulating the boundary layers, a wall treatment approach was employed. A wall treatment assumes that the near-wall cell is located within the logarithmic region of the boundary layer, and the viscous-dominated region is not resolved. It further assumes that the turbulence model chosen for the simulation is only valid outside of the viscous sublayer. There are several types of wall treatment including the high y+ wall treatment, the low y+ treatment, and the all y+ treatment. The low y+ wall treatment was used in this simulation. Figure 4.4 shows the y+ values.

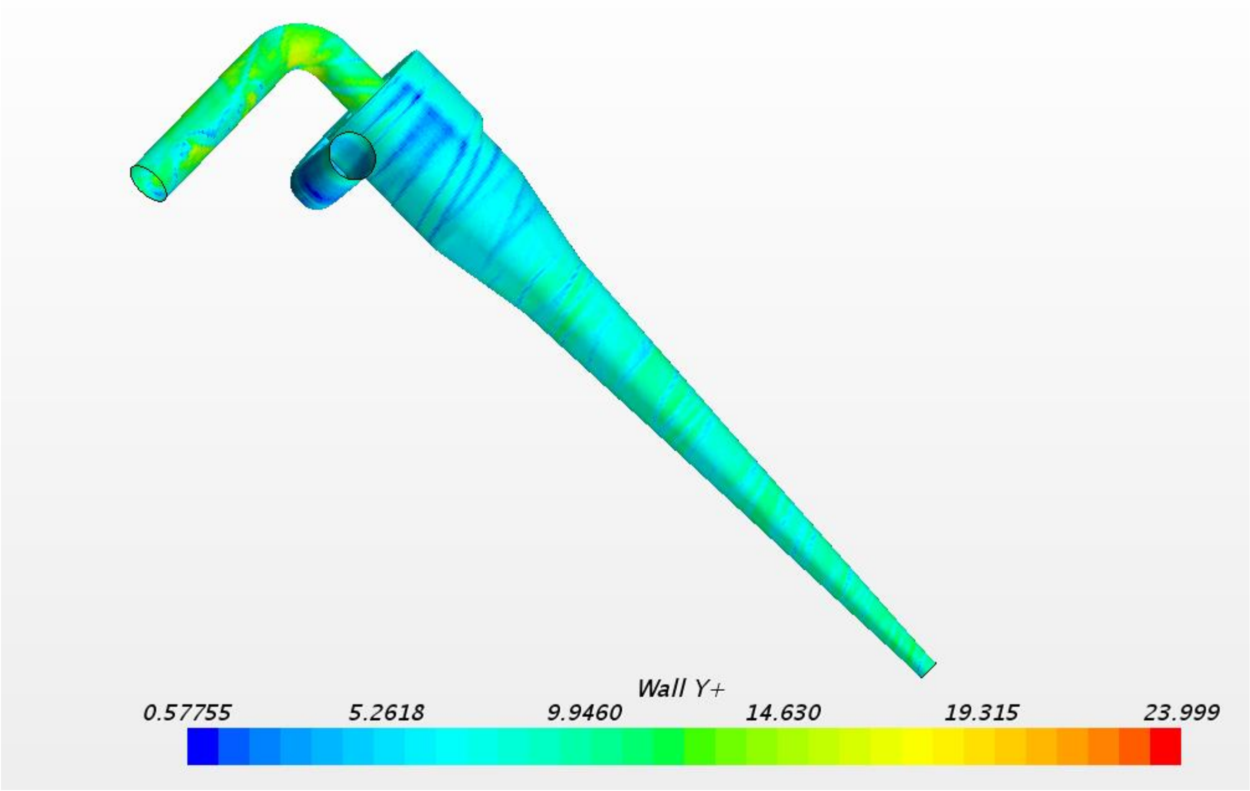

Figure 4.4 Wall Y+ Values

For a successful simulation using LES model, sufficient cells number is very important, and this is a disadvantage when compared to the RSM model because it significantly increases computational costs.

In the numerical calculation process, multiphase mixture and volume of fluid (VOF) model were selected, and no chemical reaction between the two phases was defined.

4.2 Boundary Conditions

The hydrocyclone surface was split by patches and three boundaries were determined based on the real life applications: inlet, overflow and underflow. The inlet was assigned as a 'velocity inlet', the overflow and the underflow were assigned as 'pressure outlet'. Multiphase flow was considered in this numerical simulation. The flow field inside the hydrocyclone was assumed to be filled by air, and then the liquid was introduced from the 'inlet' boundary. This was done to simplify the computational process without losing any reliability. This is the same for the experimental setups. The hydrocyclone rig is empty at first and then the NaI solution is introduced into it from the inlet, thereby forming a uniform air core inside the hydrocyclone.

The inlet flow rate was measured with the help of the magnetic flow meter (Model 8732C by ROSEMOUNT) which was then used to calculate the inlet velocity at the inlet section. The constant value of 0.94 m/s was assigned to the 'velocity inlet' boundary. The value of static gauge pressure at the overflow was measured using a digital pressure gauge (Model XP2i, Crystal Engineering).

The SonarTrac was installed in the overflow pipe section which provided the percentage of air by volume coming out from the overflow. The 'overflow' boundary was set to 99.864% NaI and 0.136% Air.

When the Reynolds stress turbulence model was employed, the turbulent boundary conditions at the inlet were set to "turbulent intensity" and "turbulent length scale" and the following relationships were used to calculate the numerical values:

$$\mathrm{I} = 0.16 \text{ x } (\mathrm{Re_D})^{-1/8} \qquad (4.1)$$

$$\gamma = 0.07 \text{ x } \mathrm{D} \qquad (4.2)$$

Where I is the turbulence intensity, D is the inlet diameter, γ is the turbulent length scale, and $\mathrm{Re_D}$ is the Reynolds number based on the inlet diameter which is defined as:

$$\mathrm{Re_D} = \frac{\mathrm{U\ x\ D\ x\ \rho}}{\mu} \qquad (4.3)$$

Where U is the inlet velocity and μ is the dynamic viscosity of the operating fluid, and ρ is the density of the liquid, which is the sodium iodide solution. By substituting the known values into the above equations, the turbulent quantities can be obtained:

$$\mathrm{Re_D} = \frac{1.0\mathrm{m/s\ x\ } 0.051\mathrm{m\ x\ } 1850\ \mathrm{kg/m^3}}{3.6\ \mathrm{x}\ 10^{-3}\ \mathrm{Pa.s}} = 26{,}208$$

$$\mathrm{I} = 0.16\ \mathrm{x}\ (26208)^{-1/8} \rightarrow \mathrm{I} = 0.0449$$

$$\gamma = 0.07\ \mathrm{x}\ 0.051\ \mathrm{m} \rightarrow \gamma = 3.57\ \mathrm{x}\ 10^{-3}$$

The viscosity of the working fluid was measured by STRESSTECH HR (ATS Rheosystems, NJ) - a high resolution oscillatory rheometer - at different temperatures. A value of $3.6\mathrm{x}10^{-3}$ Pa.s was used to set up the dynamic viscosity in the computational simulation based on Ke's works (2016). The working temperature for the Experimental data acquisition was 25 C. Figure 4.5 shows the viscosity vs temperature graph.

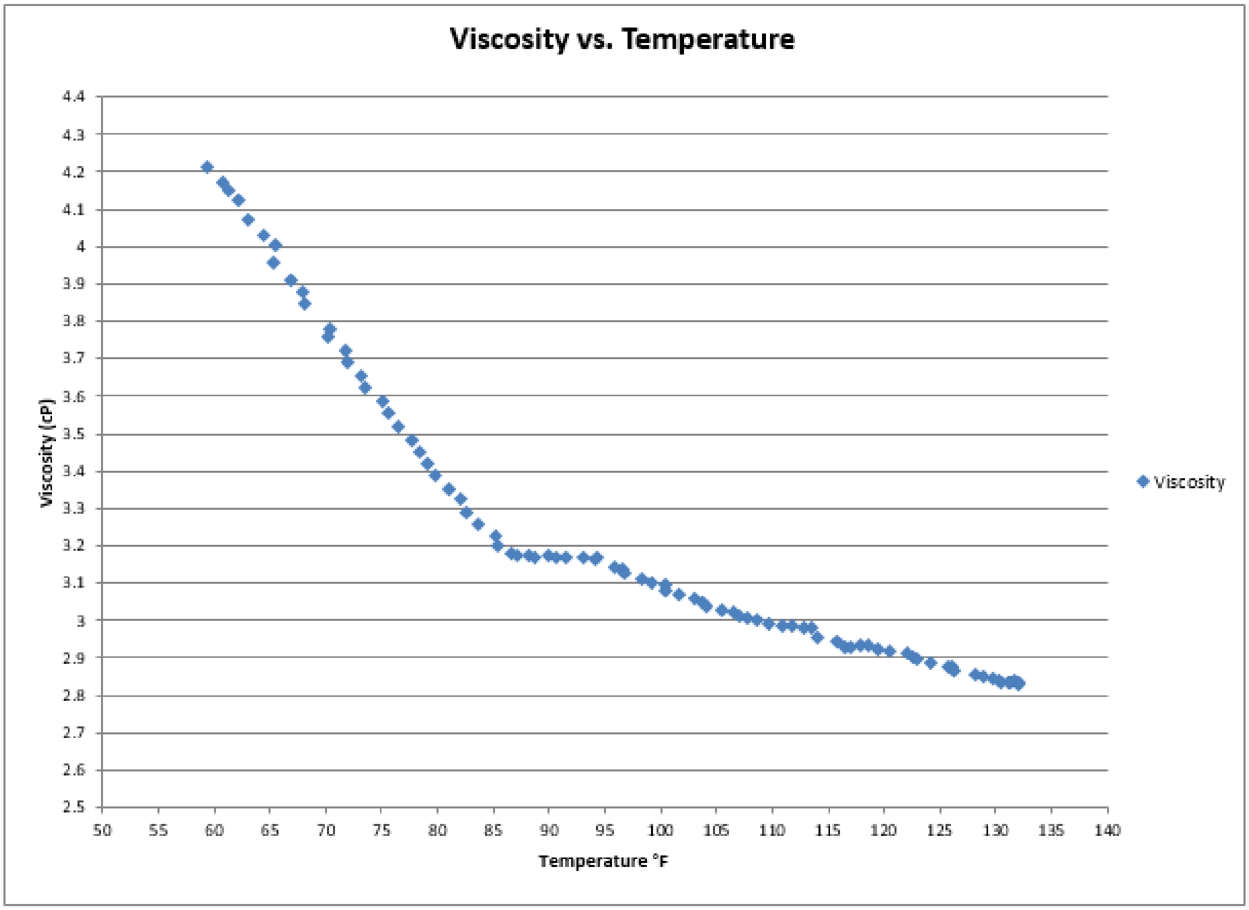

Figure 4.5 Temperature vs Viscosity of NaI solution

The pressure outlet condition was chosen for both the overflow and underflow. The static pressure values for both outlet were specified in the Star CCM+; both these values were set to 0 atm.

Since there is highly swirling motion at the boundaries, the radial equilibrium outlet option was selected in order to improve the simulation. When this option is enabled, the defined static pressure only applies to the center of boundary. The pressure gradient is calculated by:

$$\frac{\partial p}{\partial r} = \frac{\rho V_{\theta}^{2}}{r} \qquad (4.4)$$

Where r is the distance from the center axis, and V_θ denotes the tangential velocity. The static pressure distribution here at the outlets is fully based on the tangential velocity. The following figure 4.6 describes all the boundary conditions used in this simulation.

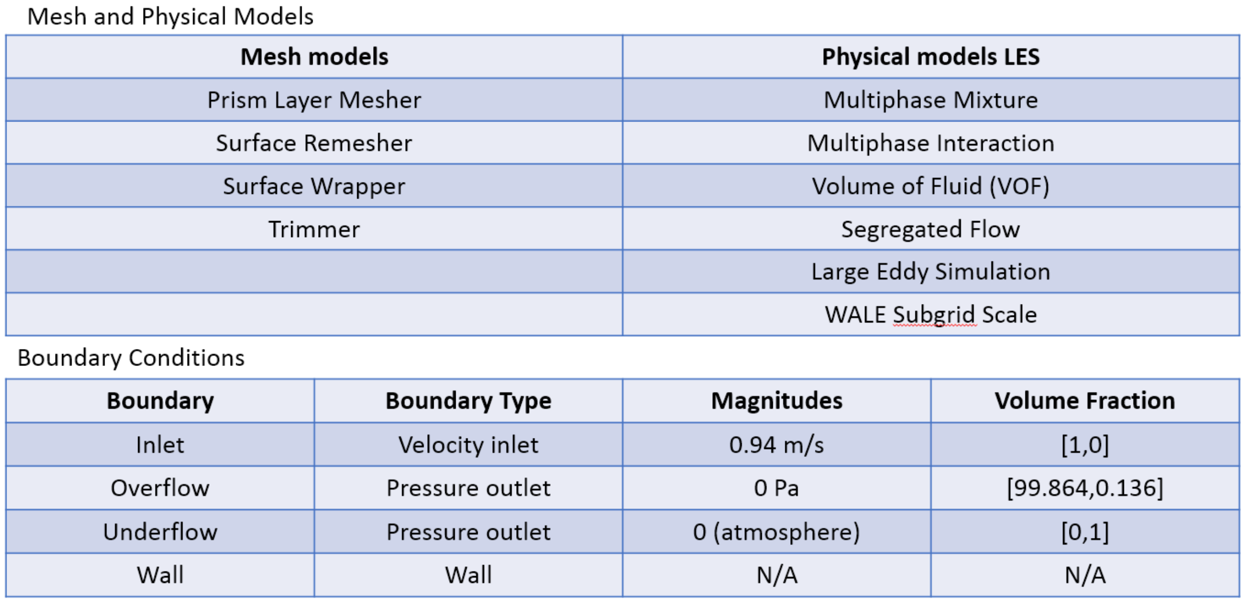

Mesh and Physical Models

Mesh models	Physical models LES
Prism Layer Mesher	Multiphase Mixture
Surface Remesher	Multiphase Interaction
Surface Wrapper	Volume of Fluid (VOF)
Trimmer	Segregated Flow
	Large Eddy Simulation
	WALE Subgrid Scale

Boundary Conditions

Boundary	Boundary Type	Magnitudes	Volume Fraction
Inlet	Velocity inlet	0.94 m/s	[1,0]
Overflow	Pressure outlet	0 Pa	[99.864,0.136]
Underflow	Pressure outlet	0 (atmosphere)	[0,1]
Wall	Wall	N/A	N/A

Figure 4.6 Boundary Conditions used for CFD (Volume fraction given as [Liquid fraction, Air fraction.])

4.3 CFD Results

The velocity and pressure profiles predicted by the computational simulation of the flow in the hydrocyclone are presented and discussed in the current chapter. Multiphase flow was used in the simulation: fluid phase (NaI and Water) and gas (air) phase. The prediction of the size and shape of the air core is also presented. The computational results will be validated by the experimental results in the subsequent chapters. The choice of the turbulence model is very crucial since, as discussed previously, the flow inside the hydrocyclone is highly swirling. The k-ε model has limitations when predicting the flow characteristics accurately. The Reynolds stress model and Large Eddy simulation both showed good agreement with experimental measurements in some recent cyclone studies.

Ke (2016) used both the RSM and LES turbulence model. He concluded in his study that CFD results which were achieved using the LES model were validated by the PIV data for flow within the hydrocyclone with an air core present. Hence, the LES model is adopted in the simulation in this study for validating the PIV data in the r-z plane.

The LES model presented better results about air core shape and dimensions although it was computationally expensive when compared to the RSM model. The implicit unsteady time step and the second order discretization scheme were used in the LES simulations and the time step was eventually set to 0.00001 seconds. A larger time step was initially used in order to get the air core to form within a reasonable amount of computational time.

The following is some guidance on how to develop a stable air core CFD solution from Ke (2016):

When flow is injected from the inlet, a higher time step scale was used initially, such as 0.1 seconds, and the number of inner iterations was set to 15 or less for a faster turnaround time, because from inlet to the vortex finder, the flow is just like the pipe flow. Next, the flow field was monitored and as the solution progressed, and the time step was gradually reduced to 1e-5 seconds, while the number of inner iterations per time step was increased to 20 or more. It should also be noted that the LES model requires a smaller time step scale than RSM, so if running RSM simulation, a time step of 0.001 seconds can be sufficient.

When doing RSM simulations, it is also necessary to specify “Turbulence Specification”, with which you have the options to pick “intensity + Viscosity Ratio”. The intensity could be set to 0.01~1, and the turbulence viscosity ratio is from 10~100 (star CCM+ user tutorial).

When using 2nd discretization scheme, it is best to start with 1st order, and once the solution has progressed and become stable, go to 2nd order.

At the beginning of the simulation, it is best to increase the under-relaxation factors, but it should always < 0.9. This helps to obtain a faster convergence per time-step. Subsequently, as the solution progresses, in order to stabilize the simulation, a value < 0.5 should be used.

Next, the boundary conditions are the most important for air core formation. Ke (2016) recommended 100% air volume fraction, as for overflow, although 100% air fraction is not a real case, but with fluid phase in the overflow, the backflow could cause some issues, and this can be used as a first attempt. In this thesis actual measurements of the % air content at the overflow is measured using the SonarTrac, and can be used to set the boundary condition in the overflow once a stable solution is obtained, thereby increasing the accuracy of the solution.

Another option would be to start with a steady simulation, obtain a steady simulation converged first, and then transfer to an unsteady simulation. However, this technique of using a steady simulation (starting with the cyclone full of liquid initially) yielded unstable results when tried at GIW in the summer of 2017, and hence abandoned.

For LES, it is recommended to start with the RSM turbulence model, and then once the solution is developed and stable, switch to LES.

4.3.1 Air Core Shape and Dimensions

As presented in Figure 4.7, central radial-axial plane (central r-z plane) is illustrated. The Cartesian coordinate system was also used in the numerical simulations to denote every plane where contours are presented in order to help readers become familiar with the geometrical notations used in this study.

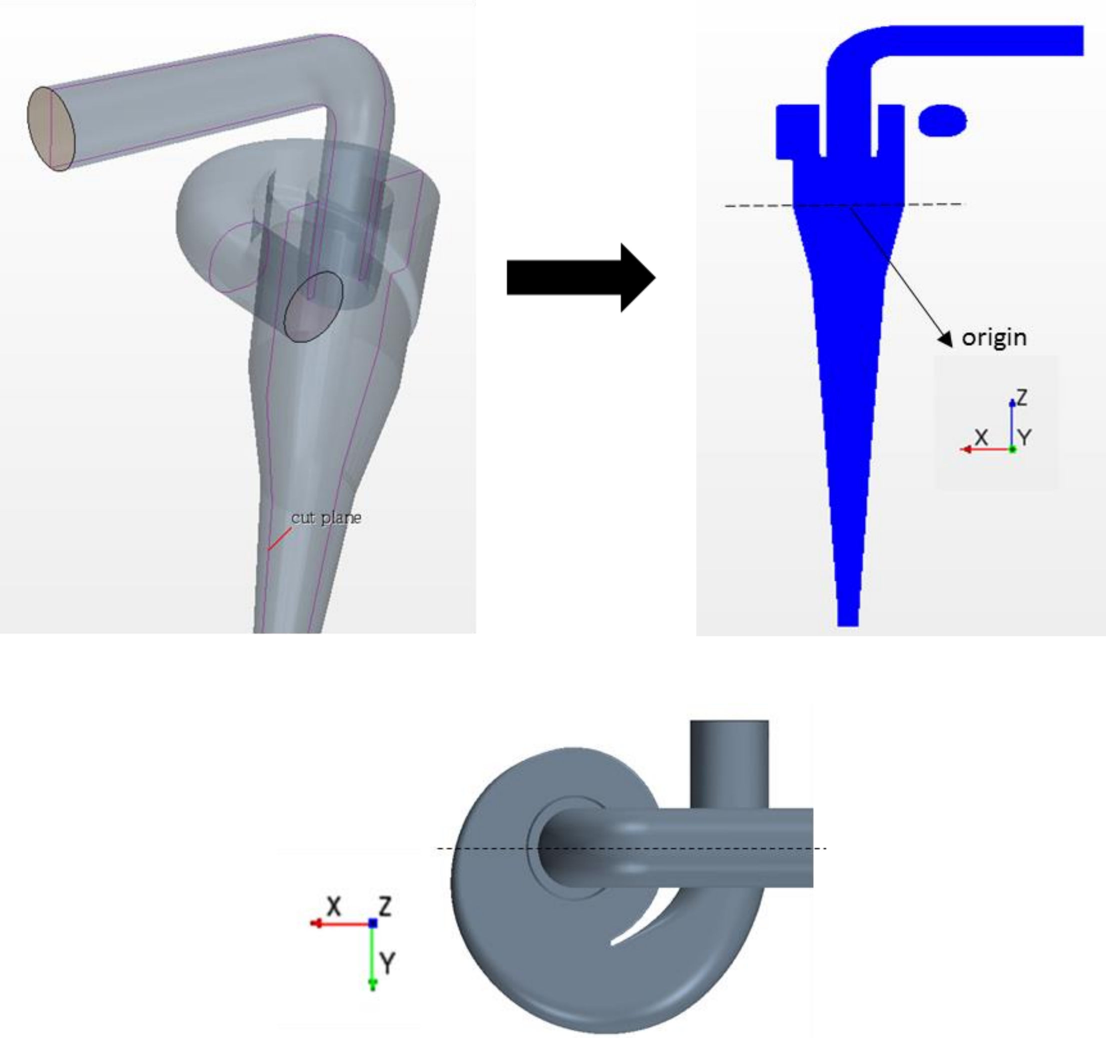

Figure 4.7 Schematic view of the cut planes (r-z plane)

Figure 4.8 shows the volume fraction contour for the LES model on the central r-z plane. As can be seen, the development of an air core was observed in the central area of the hydrocyclone.

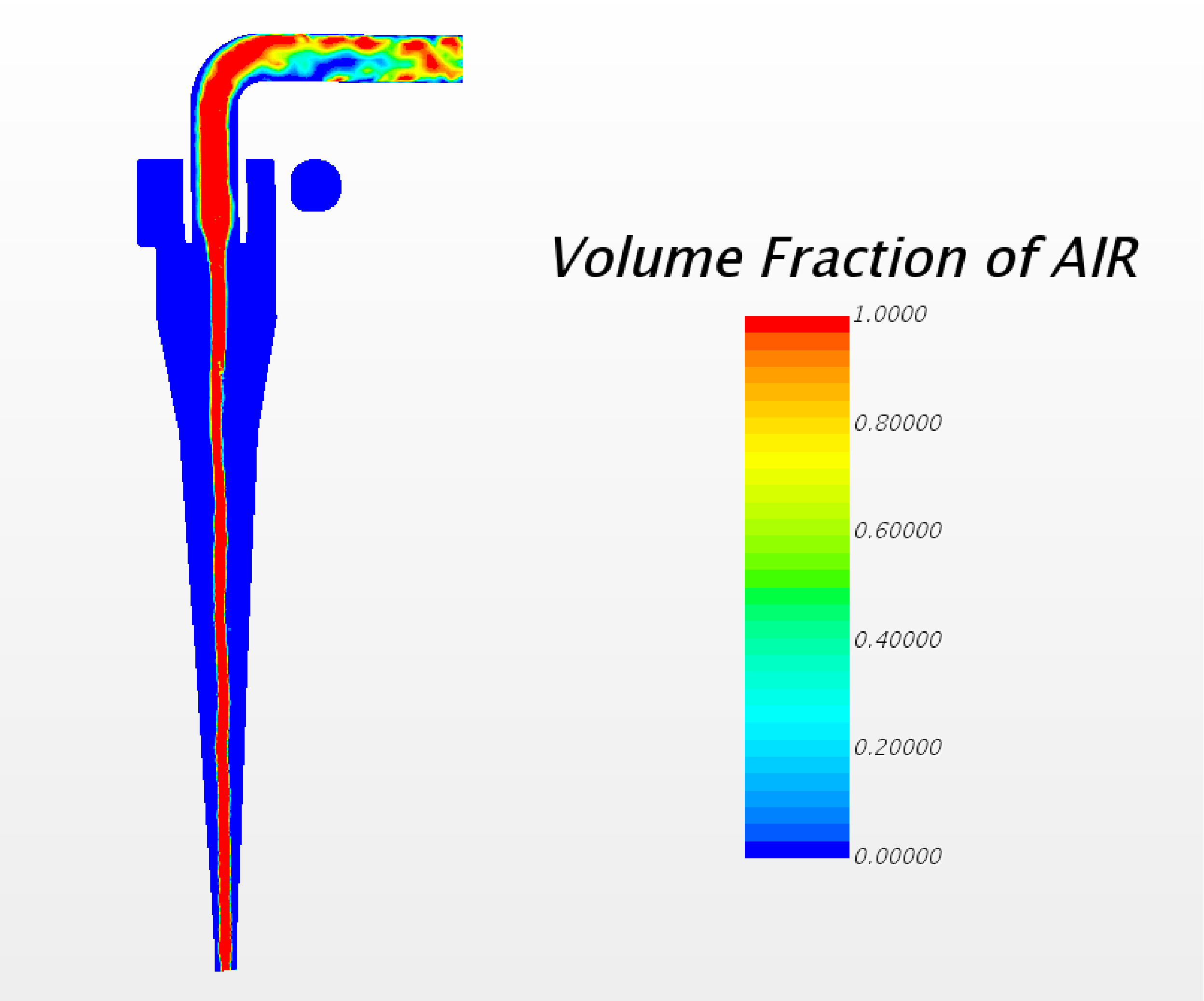

Figure 4.8 Volume fraction of air: LES turbulence model

As shown in Figure 4.8 the LES turbulence model provides a better prediction of the air core shape and dimensions. According the Ke (2016) the air core exhibits a discontinuous nature when using the RSM turbulence model.

4.3.2 Predicted Velocity and Pressure Contours and Plots

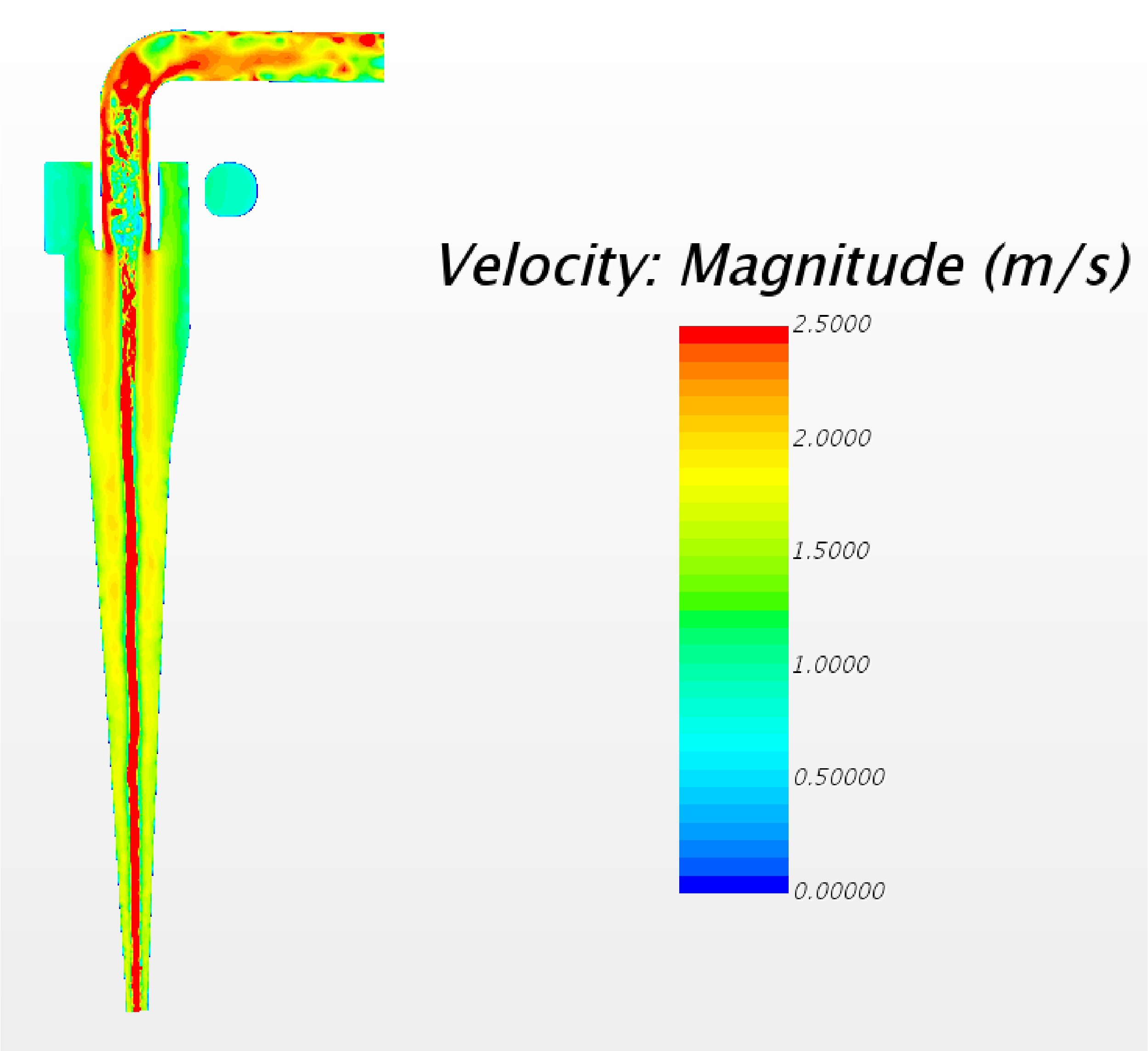

Figure 4.9 Velocity contour of LES turbulence model

Figures 4.9 shows the velocity contour at the central r-z cut plane for the LES turbulence model. The incoming flow injected into the hydrocyclone creates a secondary flow which moves directly to the vortex finder without separation. This phenomenon is known as “tip leakage”.

The total pressure contours of the LES turbulence model at central r-z cut plane is shown in Figure 4.10. The contour presents the low pressure core area in the center of the hydrocyclone. Due to the existence of the air core, small negative pressure values were observed. Nevertheless, the LES contour gives a maximum total pressure magnitude of 12,543 Pa in the inlet pipe. In order to indicate the locations from which forthcoming velocity plots (Figures 4.13 – 4.15) are taken, positions of each interrogation line are indicated in Figure 4.11.

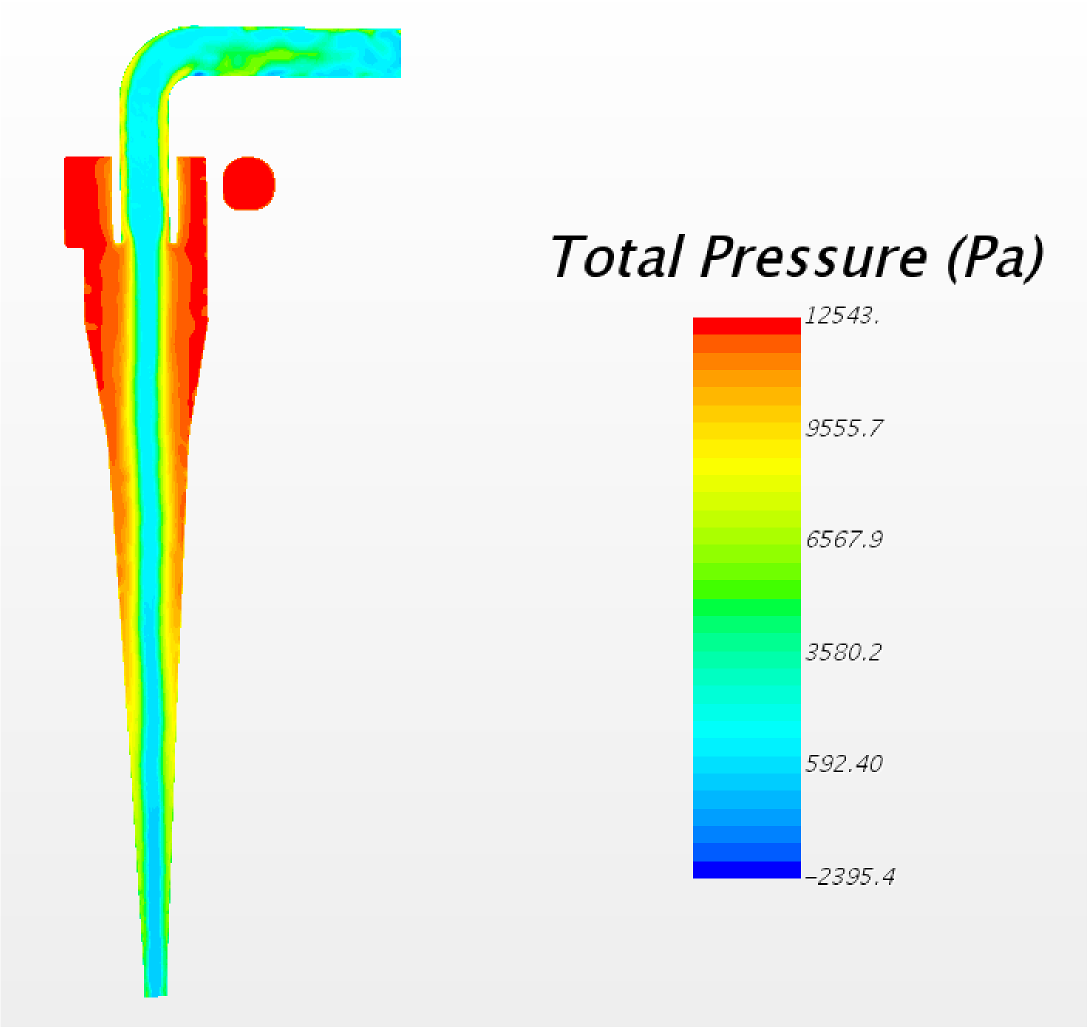

Figure 4.10 Total pressure contour of LES turbulence model sections

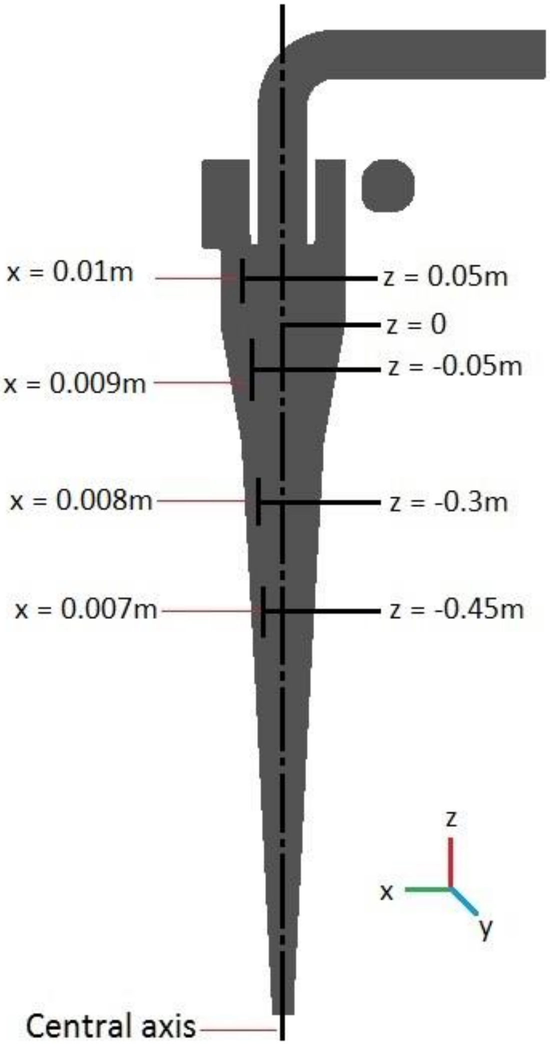

Figure 4.11 Various interrogation planes on the hydrocyclone plane

y=0.01m, z=-0.05m was the first plane of interest in the r-z plane during PIV experiments. The velocity and the total pressure contour are presented below.

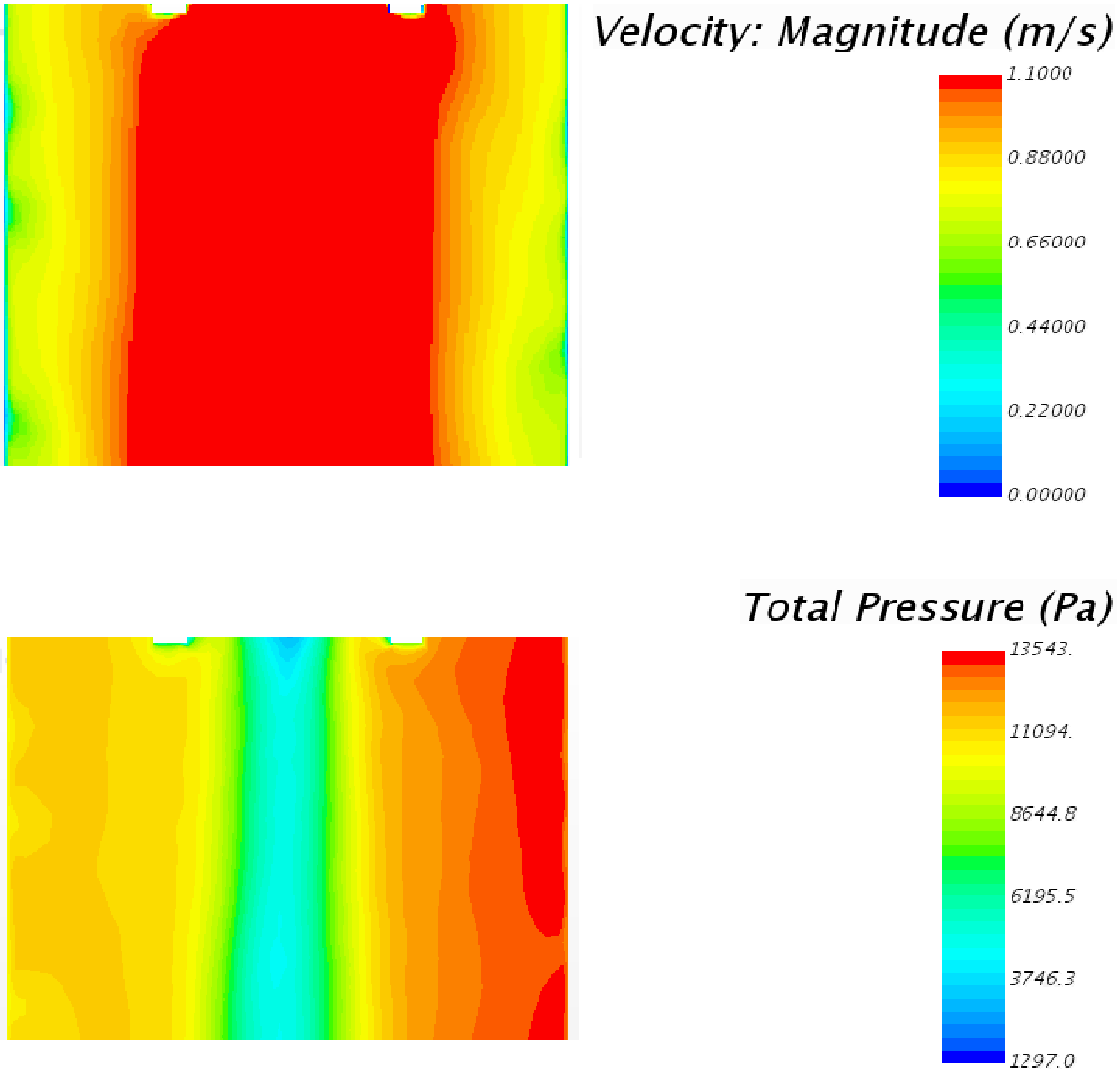

Figure 4.12 Velocity and Total Pressure contours of 1st section

The inlet pressure was recorded using a pressure gauge mounted at the inlet pipe as 11,307 Pa, and the dynamic pressure can be calculated using:

$$P_d = \frac{1}{2}\rho v^2 \qquad (4.5)$$

Where P_d is the dynamic pressure, ρ is the density of the working fluid, and v is the mean inlet velocity. Substituting the known measured values into the equation gives a value of dynamic pressure of 900 Pa. The velocity profiles in the r-z generated using the LES models are shown below.

The first section was offset to x = 0.01 m; z=0.05 m from the central axis of the cyclone. z = 0 represents the beginning of the conical section of the hydrocyclone. The second section was at x = 0.009 m; z = -0.05 m, the third at x = 0.008 m; z = -0.3 m, and the fourth at x = 0.007 m; z = -0.45 m. Figure 4.12 shows the radial velocity distributions at all the four different test locations in the r-z plane. Radial velocity is the smallest by magnitude among the three components of velocity. The graphs show the value being comparatively very small than the tangential and axial component of velocity. Since the test planes are offset from the air-core, the tangential velocity shows a steady increase when moving away from the center and then decrease towards the cyclone wall. The magnitude of tangential velocity decreases as the radius of the hydrocyclone decreases. The magnitude of axial velocity is higher near the air core, hence the graph shows a steady decrease of axial velocity as we move away from the central axis. Since we are offset from the air core, the locus of zero cannot be located in the r-z plane. Also from the graphs it can de deduced that the highest values of axial velocity occur at different radial locations, this confirms that the air core is not of a perfect cylinder shape instead has a wavy nature.

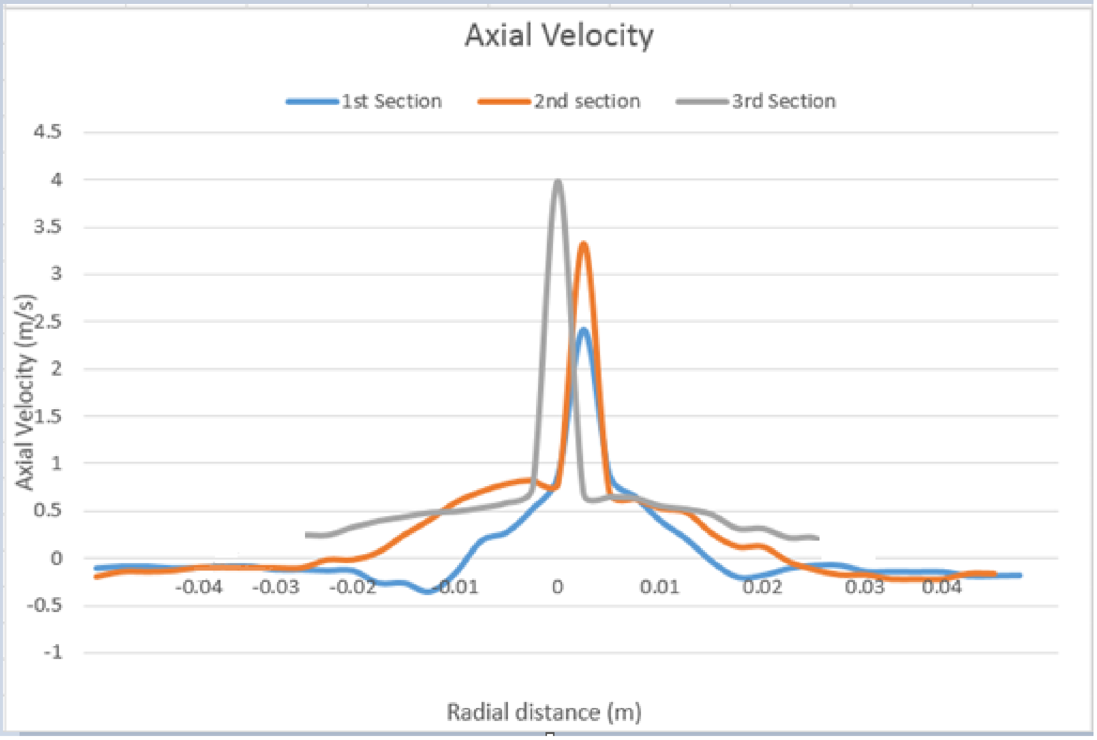

Figure 4.13 Axial Velocity profiles at various test locations

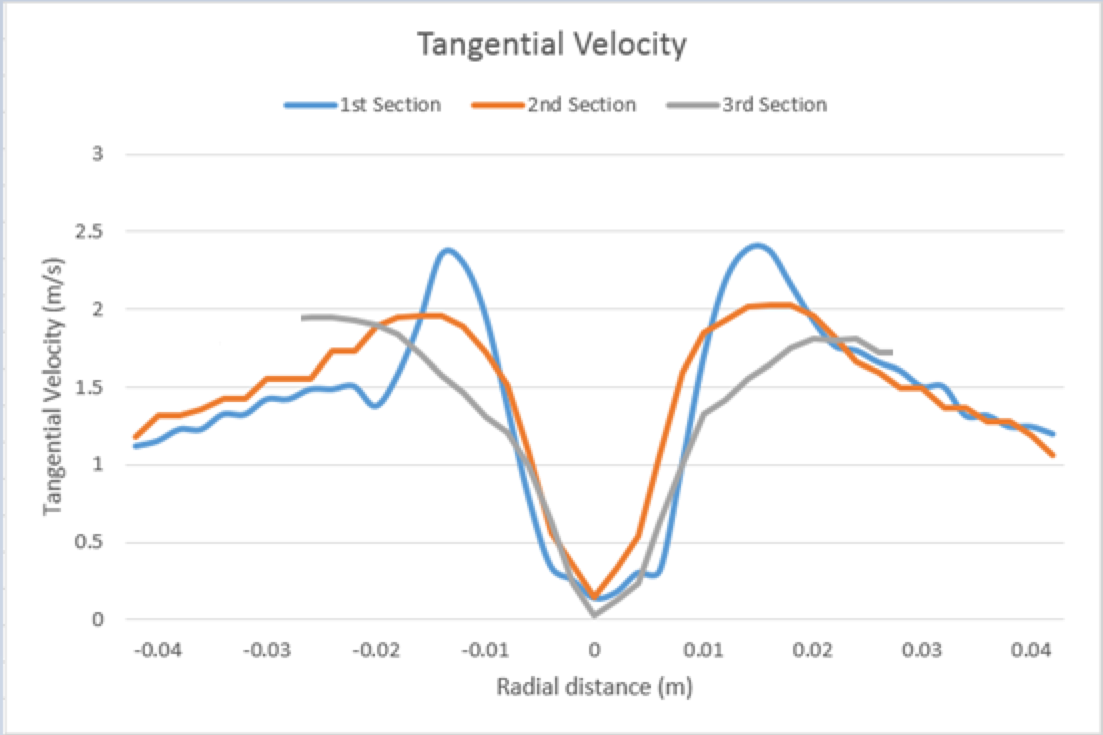

Figure 4.14 Tangential Velocity profiles at various test locations

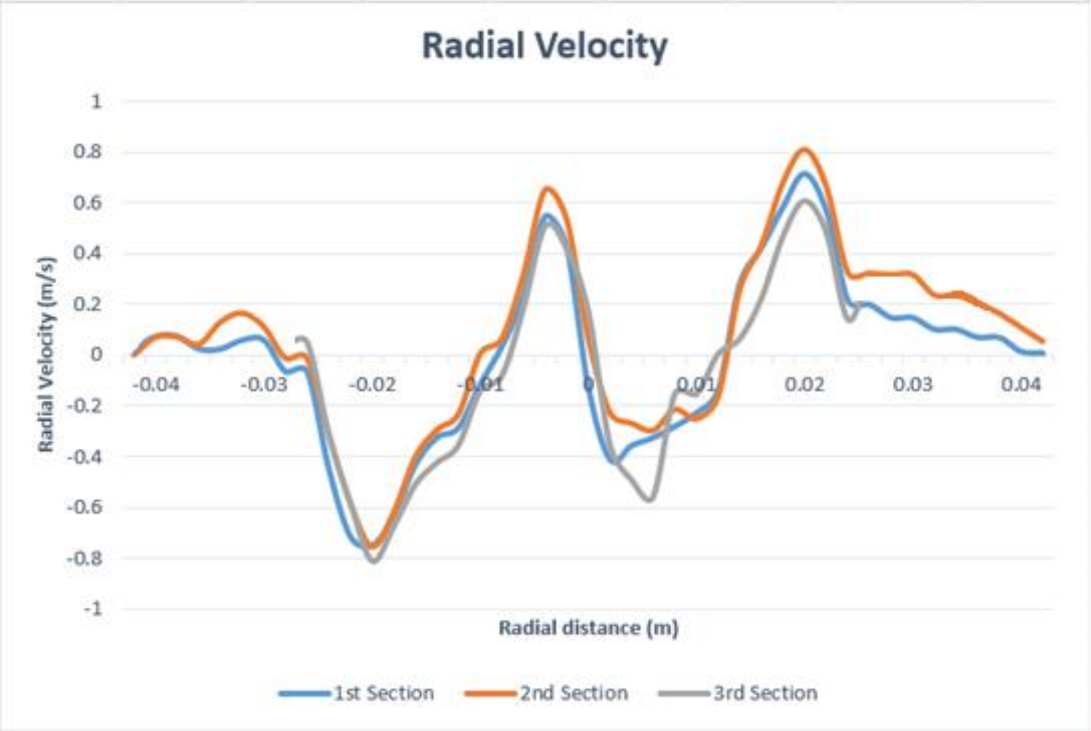

Figure 4.15 Radial Velocity profiles at various test locations

As can be seen in the Figures, the radial velocities are relatively small among the three velocity components. As the data was taken in the r-z plane, the axial components are still the main focus.

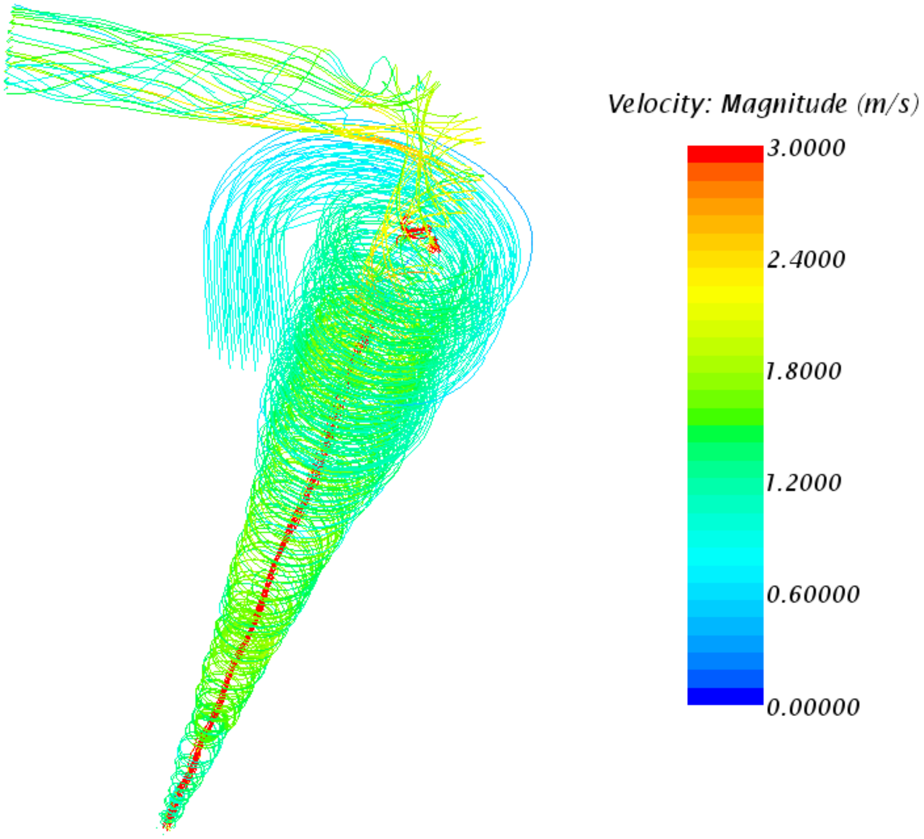

Figure 4.16 Streamlines

Figure 4.16 presents the streamlines, with the color indicating the velocity magnitude. It can be seen that the streamlines which constitute the outer swirl move towards the underflow. The streamlines of upward flow including the air and the liquid create an inner swirl which has a smaller diameter than the outer swirl.

CHAPTER 5

EXPERIMENTAL METHODOLOGY

5.1 Introduction

This chapter will concentrate on the experimental method of Particle Image Velocimetry (PIV) which was used to get the velocity vector measurements, which were used for validating the computational results. The experimental setup will be described: the same hydrocyclone and the same technique (PIV) of Ke's earlier investigation (2016) were used in this investigation. The experimental rig was altered for using the SONARtrac instrument. A u-loop pipe section was installed in the overflow section of the hydrocyclone for using the SONARtrac. The experimental setup will be explained in the following text.

The two major parameters affecting the operation of a hydrocyclone are: geometry of the hydrocyclone and the properties of the feed stream. In the current project, the velocity and pressure distributions are taken into consideration, since the performance and operational efficiency of the hydrocyclone depends on them. Hence, the optimization process for new designs can only be made if the flow characteristics in a cyclone are well known and modeled under normal operating conditions. Therefore, for optimizing the design and operation of the hydrocyclone with CFD, the vector maps and pressure at the inlet of a cyclone flow to be determined in order to validate the CFD model.

In the experimental setup, the underflow is open to atmosphere, therefore air entering the cyclone forms an air core. Due to this, the separation efficiency and pressure drop would be different at the same flow rate of the feed stream than if there were not an air core present. In this study, a mixture of air and sodium iodide solution is observed in the overflow pipe. This causes the formation of air bubbles in the tank due to high turbulence levels. This problem is discussed in the later sections.

The computational simulation of the hydrocyclone was performed with the use of the commercial software Star CCM+ as discussed in Chapter 4. The results obtained from the simulation were good and showed agreement with many studies in the literature. However, due to the high dependency of the numerical solution on the discretization of the continuous domain and boundary conditions, and due to numerical errors, only numerical data is not reliable. Therefore, validation of the computational data has to be done using the experimental results. A scaled down version of a hydrocyclone was manufactured using acrylic plastic and was used in the experiments. The velocity vector maps were obtained on planes of interest of the hydrocyclone using the PIV. NaI aqueous solution was used as the working fluid so that refractive index matching could be achieved. The refractive index was matched to acrylic plastic (RI = 1.485).

The experimental setup consisted of the hydrocyclone closed-loop and PIV laser diagnostics system. When compared to previous study of Ke (2016), the PIV laser diagnostics system is the same. The only difference in the loop from Ke (2016) study was that hydrocyclone flow loop had the addition of the U-loop pipe section in the overflow for the installation of SONARtrac.

5.2 PIV System

The PIV system is made up of the following components, as shown in Figure 5.1:

- A CCD camera
- Laser controllers
- An ND-Yag Laser
- PIV processor
- Optical devices
- PIV processing/post-processing software
- A host computer

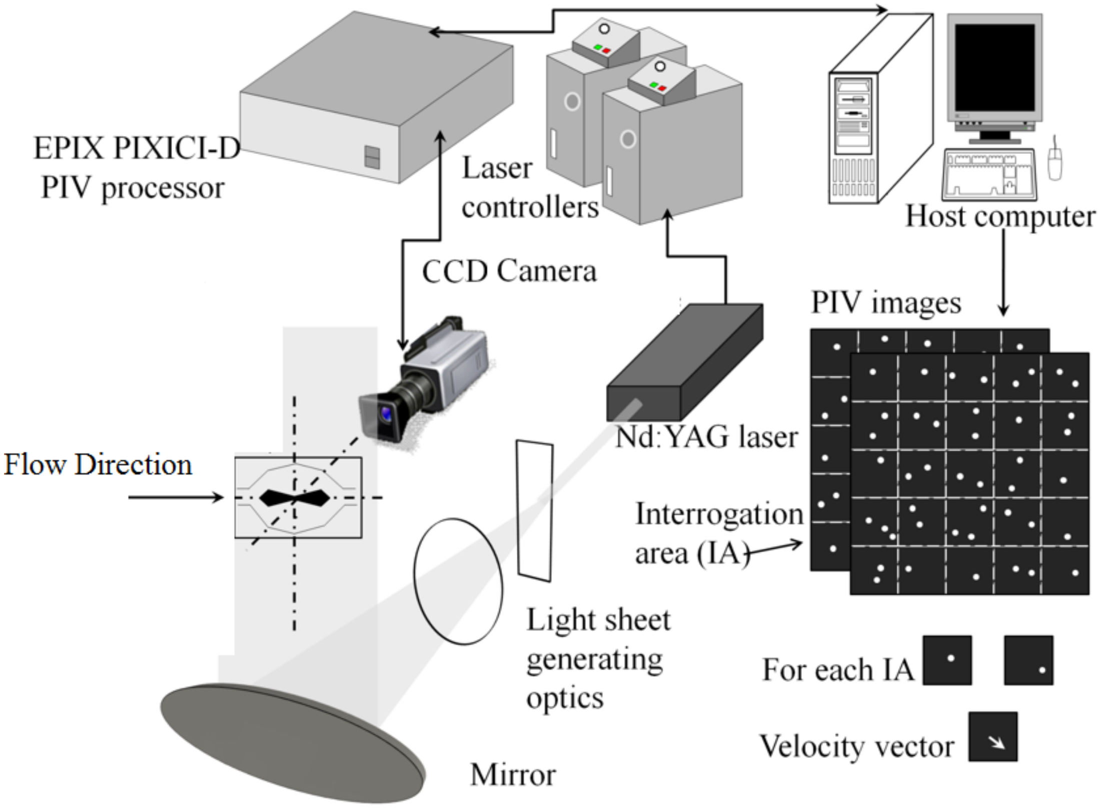

Figure 5.1 The PIV system

Particle Image Velocimetry (PIV) is a technique which enables instantaneous measurement of the flow velocities in a plane. A light sheet is introduced in the flow field, with the help of a light source, which illuminates the tracing particles in the flow and the position of the tracing particles is recorded at a fixed time step. A Digital CCD camera is used to capture two exposures of the illuminated particles in the plane. In this study, a well-known technique called "Frame Straddling" was used, and the light source was a pulsed laser in order to eliminate the background noise and decrease the time interval between exposures. The inter-frame time (time between each light pulse) was also set using a computer code, PIVACQ (written and developed by Dr. Wernet, NASA Glenn Research Center).

When the light source is turned on, the flow field is illuminated, the tracing particles scatter the light, and this scattered light is captured by the CCD camera which is placed at right angles to the light sheet. In each measurement, two exposures yields a pair of images in the plane. These images are saved on a host computer and then processed using another computer code on the host computer, PIVPROC (Wernet, NASA), which generates the velocity vector map. This computer code uses "Cross-correlation" technique for post-processing the data. The entire image will be divided into small sub-regions and calculates the average particle displacements per region. The average displacement (Δx) of the small interrogation region in the image is determined and the knowledge of the time interval (Δt) between light sheet pulses permits computation of the flow velocity (V) using Equation 5.1:

$$V = \frac{\Delta x}{\Delta t} \qquad (5.1)$$

5.2.1 CCD Camera

A charge-coupled device (CCD) is an integrated circuit etched onto a silicon surface forming light sensitive elements called pixels. Photons incident on this surface generate charge that can be read by electronics and turned into a digital copy of the light patterns galling on the device. These detector configurations are the most common image capture technology used in modern optical application.

The Kodak ES 1.0 CCD camera (Redlake MASK, Inc., CA) was used in this investigation. Some of the key specifications of the camera are list below:

- The CCD sensor array: 1008 x 1018 pixels (horizontal x vertical);
- The area of each sensor: 81 μm^2;
- Maximum acquisition rate: 15 Hz.

The camera was mounted on a mechanical aluminum plate which could be moved along the vertical axis. The focus of the camera was perpendicular to the plane of the laser sheet. A camera lens with focal length of 60 mm (Nikon) was installed to the camera. The aperture of the lens was set to 1.8 for minimum exposure to light. This allowed to capture the pictures of the tracing particles more precisely since unneeded lights were eliminated.

The camera and the host computer were connected by a PIXCI-D2X frame grabber board, made by EPIX Inc. (Buffalo Grove, IL). The camera operation and image data acquisition are controlled by the host computer. Another timer board (model NI-6602, National Instruments, Austin TX) was also installed in the host computer, which allows the adjustment of the laser firing interval time within image acquisition.

5.2.2 ND-Yag Laser and Optical Devices

The laser emitter used in this study could emit a laser beam with energy intensity of 120 mJ/pulse, wavelength is 532 nm, and the light beam diameter is 5 mm. The laser beam then passes through an optical system comprising of a cylindrical lens with a focal length of -6.35 mm and a spherical lens whose focal length is 300 mm. This setup of both the lenses would transform the laser beam into a flat horizontal laser sheet which is then reflected vertically into the hydrocyclone by a mirror set at 45 degree angle relative to the horizontal plane. When the tracing particles pass through this vertical sheet of light, they get illuminated. The distance between the spherical lens and the cylindrical lens was fixed to generate the thin laser sheet with constant-width.

5.2.3 PIV Processing Software (PIVACQ/PIVPROC)

The PIV processing technology "frame straddling technique", which is introduced by Dr. Wernet (NASA, Glenn Research Center), is a significant part of the whole processing procedure. It allows the CCD cameras to acquire images within the small time intervals needed for relatively high-speed flows.

PIV Acquisition (PIVACQ) is an interface-friendly software package developed by the NASA Glenn Research Center with great data acquisition capability. It allows the inputs like inter-frame time, frame offset, and the pulse width depending on the flow conditions. 800 image pairs were obtained for each field of view (FOV) during the experiments; this number depends on the memory space of the host computer and it is the maximum that I could get in the current condition.

PIVPROC is another software (developed by Dr. Wernet, NASA Glenn Research Center) that integrates the cross-correlation techniques. Different correlation settings and configurations are available within the program. The post-process procedure begins with introducing the image pairs into the PIVPROC, after that the interval time and the field of view should be input to set the correct physical units. It is important to enter the accurate values of the time step and the length scale of the field of view, since the change in the value of the time step can cause different values of the velocity in the same field of view.

The CCD camera has to be focused properly on the tracing particles in the plane of interest. A suitable time step has to be input into the PIVACQ settings, this can be obtained by performing mathematical calculations for the exact time step. The time step was obtained by testing different time interval values and selecting the optimum value during the experiments. The results were post processed for the different time steps and suitable time step was selected based on the observation of the vector maps.

There were three selection for the sub region in the PIVPROC. The 64 x 64 pixels interrogation area was used in this study. It is a balance between the spatial resolution and the number of data sets required to resolve fully a given plane of interest.

A problem of air bubble entrainment was faced in the experiments. In which small air bubbles enter from the inlet of the hydrocyclone. The air bubbles formed as a result of high turbulence in the large tank. A filter fiber layer had to be set up in the tank in order to stop the air bubbles from entering the inlet of the hydrocyclone. This also caused for some of the tracing particles to get stuck in the fiber but most of them could go through since they were very small in size. Hence, the 64 x 64 sub-region was used in this study as the amount of tracing particle did not facilitate the use of the 128 x 128 sub-region. Figure 5.2 shows the whole PIVACQ wiring diagram:

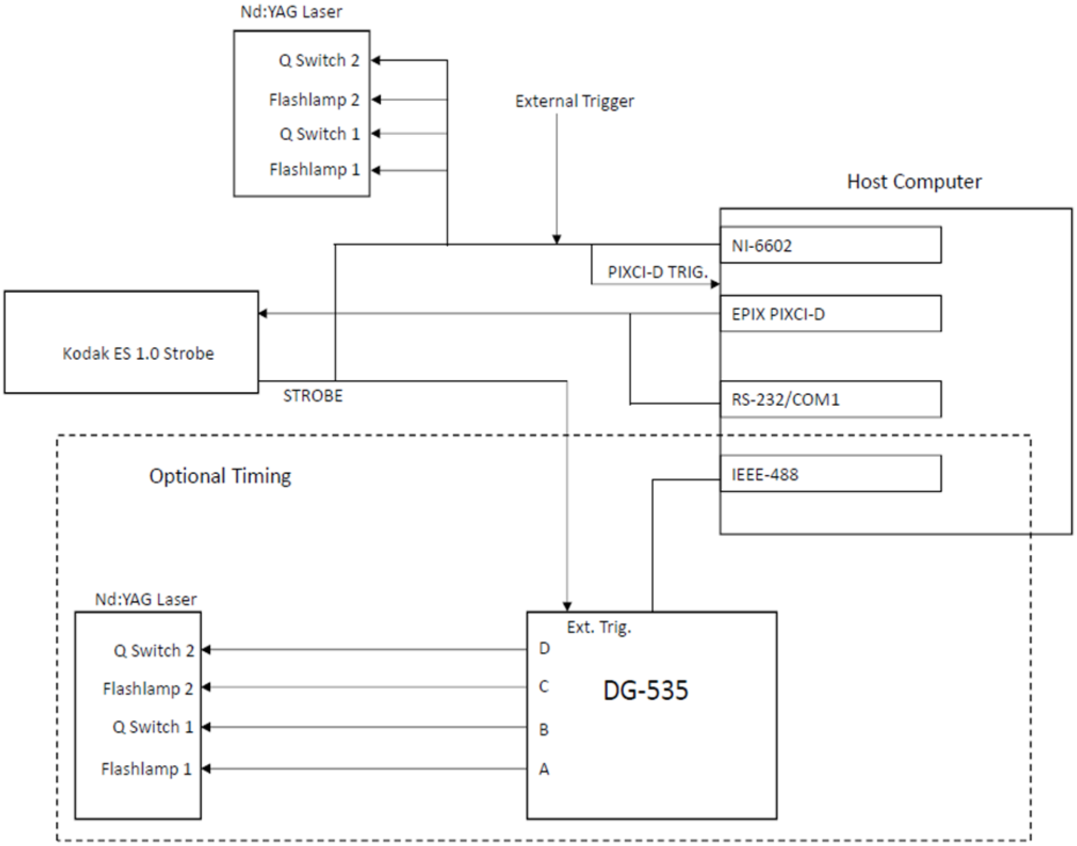

Figure 5.2 The PIVACQ wiring diagram

5.3 Solution and Seed Particles Used in the Hydrocyclone Flow Loop

The experimental model of the hydrocyclone was manufactured from acrylic plastics. This made the hydrocyclone system transparent and suitable to be used with an optical system. Refractive index matching is vital part of PIV experiments. Matching the refractive index of the working fluid and the hydrocyclone material had to be achieved so that the laser sheet would pass through the system without distorting or scattering. The refractive index of acrylic plastic is 1.49. The concentration of the NaI solution was altered to achieve the same refractive index. In order to match the refractive index the concentration of the sodium iodide in water has to reach 63.3% by weight.

The density of the solution was 1850 kg/m3 and kinematic viscosity of the solution was 2.5 cP when measured at 25˚C. The PIV acquisition was performed at 25˚C.

In PIV, the velocity of the particle is measured instead of that of the fluid. Hence, the selection of the tracing particles is of utmost importance. The selection of tracing particles requires that: they are neutrally buoyant; they should be small enough such that they follow the flow without causing any disturbance in the flow field, and they should be large enough to scatter sufficient amount of light to be detected. Silver-coated hollow glass spheres (Potter Industries Inc., NJ) were used as tracing particles for this study. It has been proven that these glass spheres could provide the ideal particle detectability. Some primary physical properties of this particle are listed below:

- The mean density: 1700 kg/m^3
- The mean diameter: 10 µm
- The refractive index: 1.8

Equation 5.2 provides an expression for the calculation of the settling velocity of the particles:

$$V_s = \frac{2R^2[\rho_p - \rho_f]g}{9\mu} \qquad (5.2)$$

Where V_s is the settling velocity, R is the radius of the particle, ρ_p is the particle density, ρ_f is the fluid density, g is the gravitational acceleration, and μ is the dynamics viscosity of the solution.

5.4 PIV Experimental Parameters

5.4.1 Optical System Magnification

Optical system magnification (M) is the ratio of the actual field of view appearing on the CCD camera array; based on the value of M, it could be magnification or de-magnification. The linear magnification of the thin lens is calculated using Equation 5.3:

$$\mathrm{M} = \frac{f}{f - d_0} \qquad (5.3)$$

Where f is the focal length and d_0 is the distance from the lens to the object. In the PIV experiment, it can also be computed using Equation 5.4:

$$\mathrm{M} = \frac{camera\ pixel\ size \times pixel\ dimensions}{field\ of\ view} \qquad (5.4)$$

The field of view of the current study was measured as 32.5mm in the horizontal direction, corresponding to the CCD camera (The KODAK ES 1.0 camera) used in this study, the pixel size of the camera is 1008 x 1018 (horizontal times vertical) and each pixel is 9µm x 9µm. The field of view used for section 1, 2 and 4 was 32.5mm x 32.5mm, while the field of view for third section was 63mm x 63mm.

5.4.2 Spatial Resolution

The spatial resolution of a vector map could be calculated by the following two equations:

$$\text{Spatial resolution} = \mathrm{S} \times \frac{N}{2} \qquad (5.5)$$

$$\mathrm{S} = \frac{Field\ of\ view}{Camera\ array\ size} \qquad (5.6)$$

Where S is the imaged pixel size. The physical meaning of spatial resolution refers to the number of independent pixel values per unit length, which also means it defines the distance between successive vectors in the vector field.

5.4.3 Dimensions of the Laser Sheet and the Camera Depth of Field

The dimensions of the laser sheet were fixed before beginning the experiments. There are two equations used to calculate, and the first equation is:

$$W_s = \frac{f_s}{f_c} d_{laser} \qquad (5.7)$$

Equation 5.7 is used to calculate the width of the laser sheet, W_s where f_s (300mm) is the focal length of the spherical lens, f_c (-6.35mm) is the focal length of the cylindrical lens, and d_{laser} (3.5mm) is the diameter of the laser beam coming from the laser generator. Inserting those values into the equation above give a light sheet width of 236 mm, which is larger than the field of view (32.5mm x 32.5mm).

The second equation is used to determine the minimum laser sheet thickness. The thickness should be less than the depth of field so that well-focused images can be obtained. Equation 4.8 is shown below:

$$T_s = \frac{2.44\lambda f_s}{d_{laser}} \qquad (5.8)$$

Where T_S is the thickness of the laser sheet, and λ is the wavelength of the laser beam, 532 nm in this experiment. Therefore, the minimum laser sheet thickness is 80μm. The camera depth of field can be computed by the Equation 5.9:

$$\delta_z = 4.88\lambda(f\#)^2 \frac{(M+1)^2}{M^2} \qquad (5.9)$$

Where f# is the camera aperture size and M is the magnification factor calculated above. f# depends on the lens and in this study it is 2.8, which is the minimum value allowed by the lens. When substituting all the already-known values into the equation, a camera depth of field of 1122 μm is obtained.

5.4.4 Imaged Particle Size

The effective particle size (d_e) is calculated as 4.4μm using Equation 5.10:

$$d_e = \sqrt{(d_p M)^2 + (2.44(1+M)\lambda f\#)^2} \qquad (5.10)$$

Where d_p is the diameter of the particle diameter, which in this case is 10μm. The first squared term in the square root indicates the particle size projected on the camera, and the second term is based on the diffraction blur of the system.

Table 5.1 summarizes all the experimental parameters that were discussed previously.

Laser Energy and wavelength of the light	120 mJ - 532 nm
Maximum Frequency	15 Mhz
Light Sheet Width (W_{LS})	236 mm
Light Sheet Thickness (T_{LS})	80 µm
Light Beam Diameter (d)	5 mm
CCD Camera Array Size	1008 x 1018
Pixel Size	9 µm x 9 µm
Camera Lens Focal Length (f)	60 mm
Magnification Factor (M)	0.286
Spherical Lens Focal Length (f_s)	300 mm
Cylindrical Lens Focal Length (f_c)	-6.35 mm
Camera Lens f#	2.8
Field of View (FOV) (Section 1, 2 and 4)	32.5 mm x 32.5 mm
Field of View (FOV) (Section 3)	63 mm x 63 mm
Sub-region Size (NxN)	64 pixels x 64 pixels
Vector Number for each FOV	30 x 30
Spatial Resolution	2 mm
Number of Image Pairs	800
Diameter of Tracing Particles	10 µm
Imaged Particle Diameter	4.4 µm
Depth of Field	1122 µm
Total Amount of NAI Solution in the Cyclone Loop	20 gallons
Refractive Index of the Fluid	1.489

Table 5.1 The experimental parameters

5.5 The Hydrocyclone Flow Loop

The hydrocyclone flow loop located in the Multiphase Flow and Laser Diagnostic Laboratory at Case Western Reserve University, was designed by GIW Industries (Grovetown, GA) and manufactured and assembled by the CWRU machine shop. The model hydrocyclone itself is the same as the one used in Ke's work. The only new addition was the U-loop pipe section in the overflow section of the hydrocyclone which was installed for the use of SONARtrac instrument Figure 5.3 shows the new schematic loop.

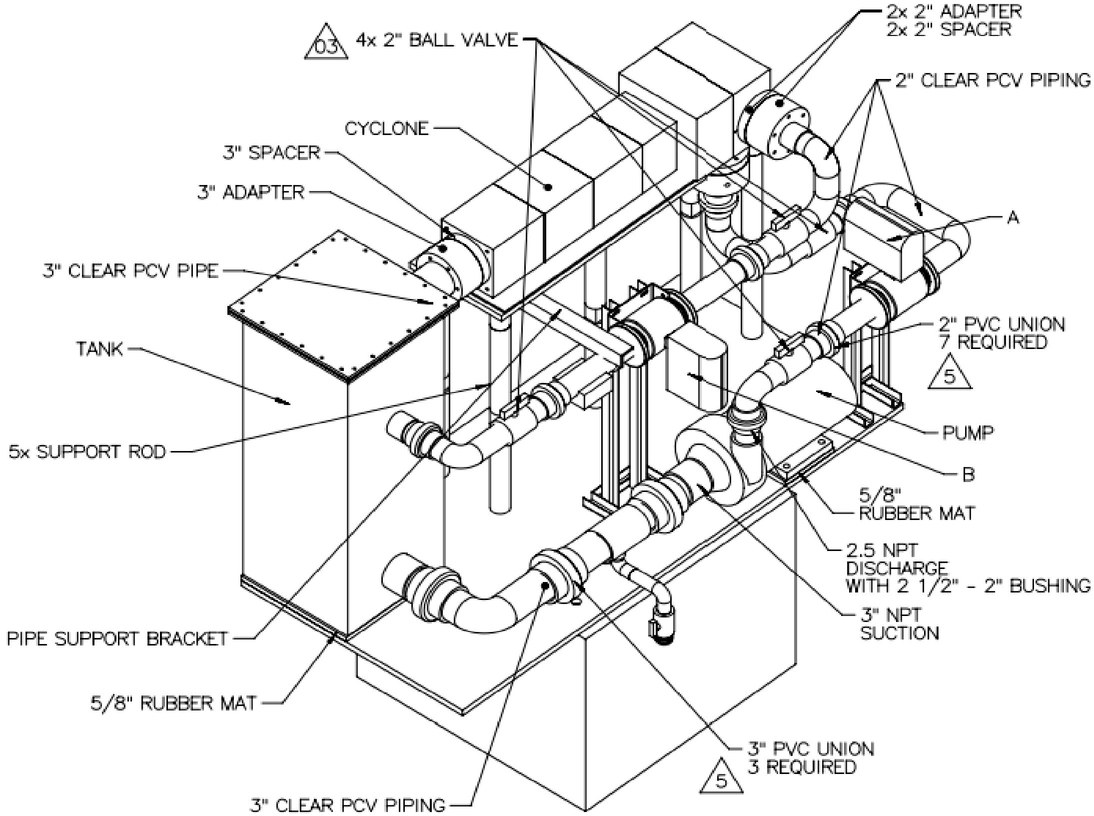

Figure 5.3 The technical drawing of hydrocyclone rig

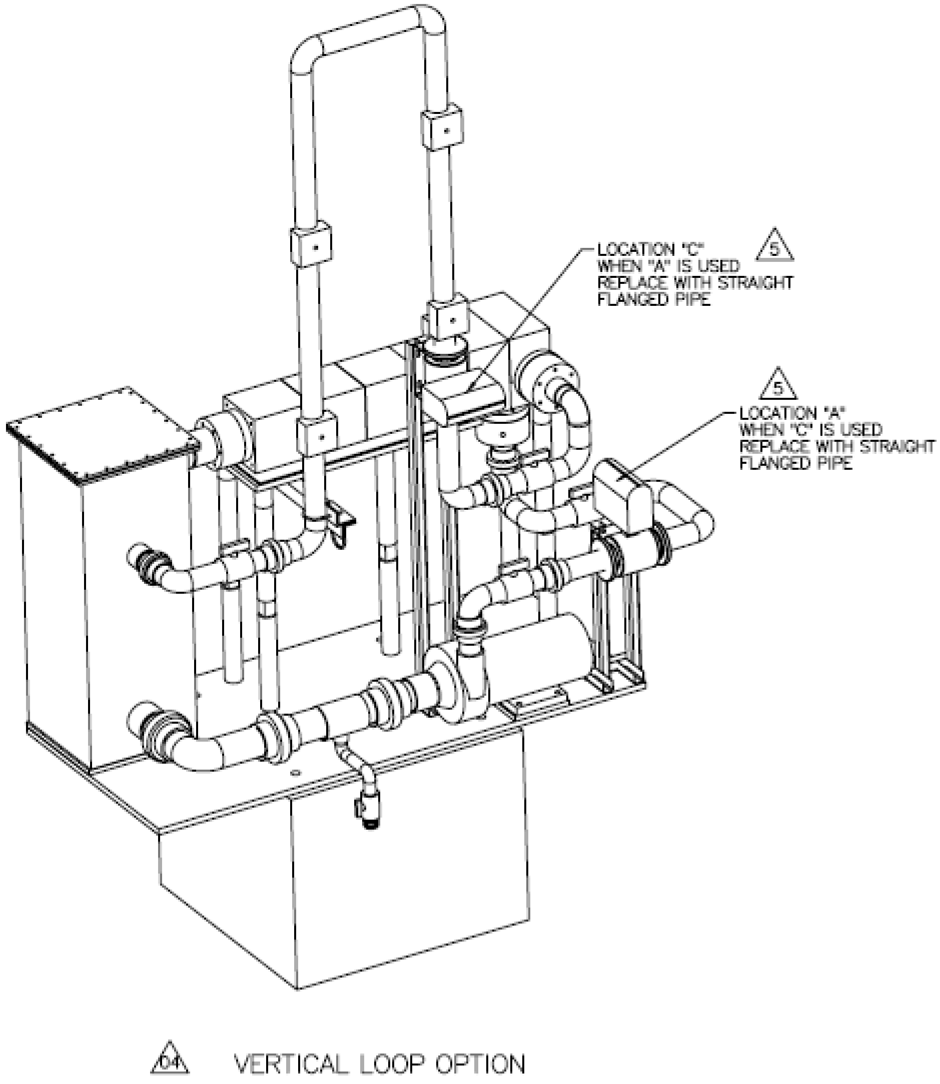

Figure 5.4 The technical drawing of the hydrocyclone rig with U-loop installed

Technical drawings of each part of model hydrocyclone are presented in Figure 5.4. A digital pressure gauge (Model XP2i by Crystal Engineering Corporation) was installed in the loop to provide the pressure value at the overflow and inlet pipe sections. A magnetic flow meter (Model 8732C by ROSEMOUNT) was mounted in the inlet pipe section (and also in the overflow section), in order to measure the volumetric feed (and overflow) flow rates with a digital readout.

Moreover, in the new loop, several sections of the loop were designed to be detachable, and they provided convenience for moving the measurement instruments to the other locations of interest, such as the overflow pipe section. A flow measurement device SONARtrac VF/GFV-100 by CiDRA was installed on the U-loop for measuring the percentage of air in the overflow section of the pipe.

The tank had the outer dimensions of 13.75 x 13.75 x 37 inches (lengths x widths x heights), inner dimensions of 13 x 13 x 36.625 inches, and it supplies fluid into a 3” clear PVC pipe that is connected to a centrifugal pump where the fluid is pressurized. Then the pressurized fluid is fed into the model hydrocyclone through a 2” clear PVC pipe as seen in Figure 5.3. Due to the vortex flow properties inside the cyclone, the feed stream is separated into two different parts, with some of the fluid joining the inner vortex which is discharged through the vortex finder, and the rest of the fluid traveling through the cylindrical and conical chamber of the cyclone spirally to the bottom, where it exits the underflow pipe.

There are several adapters that attach to the inlet, overflow, and underflow pipes of the hydrocyclone. The pressure gauges were installed in the adapters which were attached to the inlet and the overflow pipes for the measurements of the feed pressure and the overflow pressure. A 2” clear PVC pipe was used to manufacture the U-loop. The U-loop was installed in an inverted manner in the overflow pipe section which then connects to the tank. Figure 5.6 shows the dimensions of the U-loop pipe section.

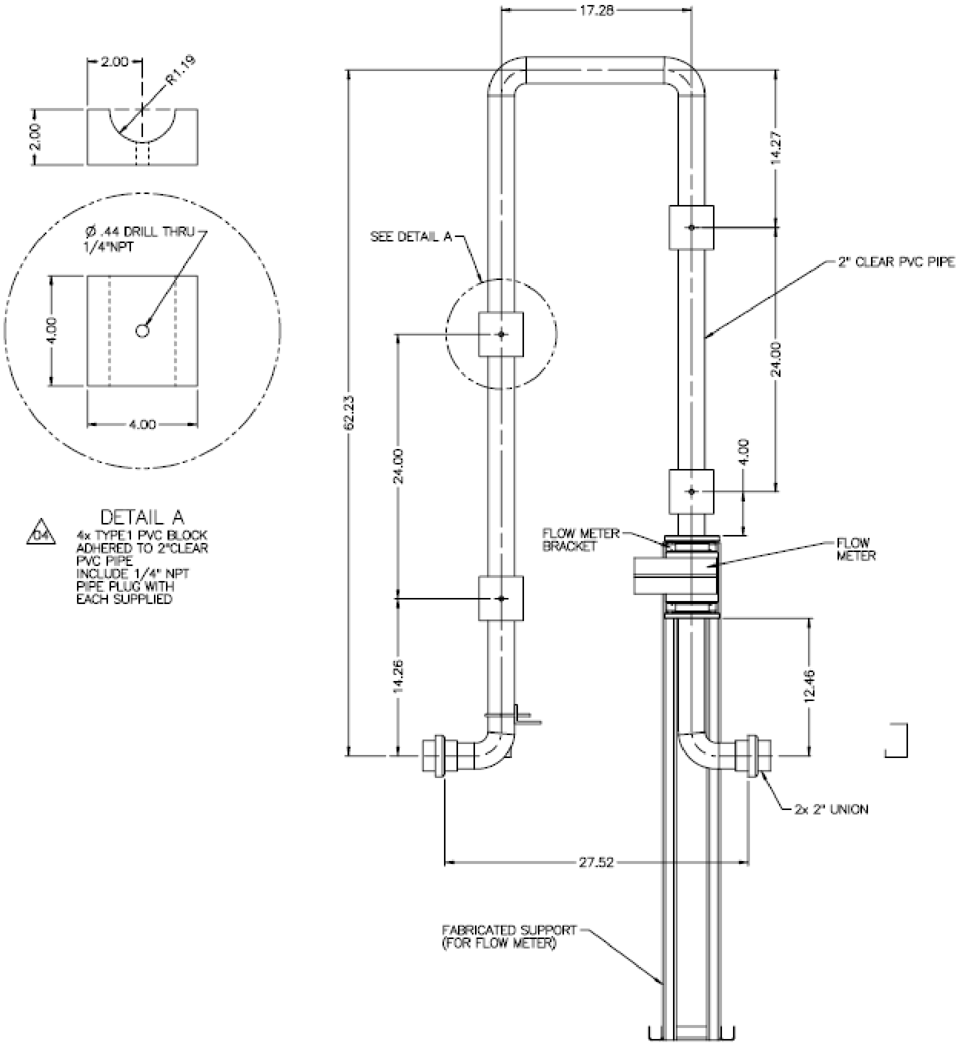

Figure 5.5 Dimensions of the U-loop pipe section

The hydrocyclone was mounted horizontally while many cyclones are installed vertically in practice. In industry, cyclones are mounted horizontally when building tailings dams with the underflow (among other applications). However, the force of gravity is considered small in relation to the centrifugal forces present in a hydrocyclone of this size. The entire loop is seated on an aluminum plate bolted to a machinists table, which allows horizontal and vertical, translation and rotation motion. A drain valve was also mounted in the pump suction pipe in order to drain the loop when needed. The sodium iodide solution was stored in 5 gallon plastic buckets and were sealed off with lids.

The liquid interface height is 5 inches below the bottom of the underflow pipe section when the pump is running and the cyclone is full of liquid, the upper section of the tank is full of air and the underflow outlet is exposed to atmosphere pressure. Air is pushed into the cyclone through underflow because of the pressure difference between the axial center of the cyclone and the air pressure in the tank (atmospheric). A macroscopic air core will be generated in the cyclone.

5.6 Experimental Procedure

5.6.1 Experimental Methodology

The first step is to set up the camera position. For this, a software known as “XCAP” was used. XCAP gives a live video of the camera’s field of view and also provides aid to measure the length scale of the FOV. The tank was filled with the sodium iodide solution until the liquid level was slightly below the underflow. The tracing particles (silver coated hollow sphere) were added to the solution. A lid was bolted to the top of the tank. Then, the pump was started at a slow speed first (usually 10 Hz) in order to avoid damage from vibration and cavitation, and the pump speed was increased by 5 Hz each time up to 30 Hz so that the sodium iodide would fill up the u-loop pipe section and then reduced down until the desired speed was achieved. Figure 5.7 shows the relation between the controller speed and the RPM of the pump.

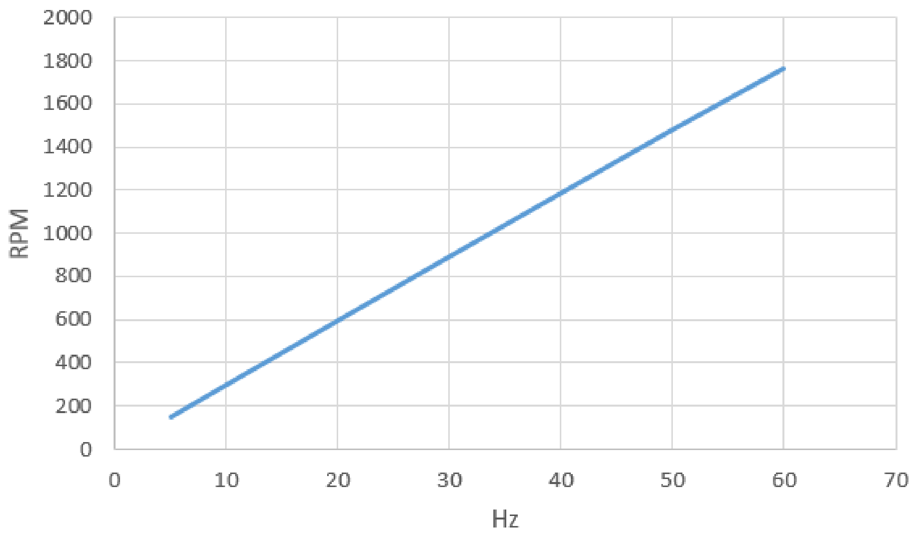

Figure 5.6 The relation between VFD frequency (Hz) and RPM of the pump

Industrial values of cyclone feed pressure correspond to controller speeds at or above 30 Hz in this setup; however, at higher speeds, air bubbles started to enter the hydrocyclone. This is explained in the subsequent section.

5.6.2 Air Bubble Issue

This study primarily focused on the analysis of a hydrocyclone with an air core present. For the formation of the air core, the underflow had to be exposed to atmosphere. Therefore, the tank could not be filled completely with NaI solution. The air that forms the air core enters from the underflow due to the pressure drop. This causes a mixture of air and sodium iodide solution that leaves the hydrocyclone from the overflow, which is fed back into the tank. This causes high turbulence in the tank. This generates more micro bubbles in the tank. These air bubbles then enter the hydrocyclone through the inlet pipe and appear in the flow obstructing the view of the tracing particles. The air bubbles also causes scattering of laser light as the refractive index is different. This phenomenon occurs continuously as the fluid circulates. Due to this performing the PIV experiments is difficult.

The amount of air bubbles increases with the increase in the pump speed hence a study at higher speed is not possible. As the speed is lowered to 10 Hz, the amount of air bubbles starts to diminish. But the air core starts to break down and disappear at this speed, so PIV experiments cannot be performed at flow rates of interest without some modification to the loop.

5.6.3 Methodology for Solving Air Bubble Problem

The micro bubbles are formed due to the high ionic levels present in the NaI solution together with the presence of trace levels of organics. Several tests were performed on samples of the sodium iodide solution using different chemical reagents in benchtop experiments. However, the problem could not be solved by any of them. It was determined that a mechanical air removal procedure should be employed. A filter membrane could stop most of the air bubbles from passing into the inlet of the hydrocyclone. The polyester fiber material that is used in filtration systems of aquariums, proved to be a good filter material during testing. But it had some limitations: as it could not stop the air bubbles from entering the inlet at speeds higher than 20 Hz. But it proved to be of great use as at 20 Hz clear PIV data could be obtained with a stable air core as such, all PIV data presented in this thesis was taken at 20 Hz pump speed. In order to place the filter fiber in the tank a support structure had to be designed. A 316 stainless steel basket designed and provided by GIW Industries was used to support the filter fiber inside the tank. The un-compressed thickness of the fiber layer was 7 inches, and some rubber weights were put on the top of the fiber layer in order to compress it and leave no space between the tank wall and the filter floss. A square shaped rubber gasket was also designed and provided by GIW industries which was placed over the stainless steel basket to obstruct the leak of air into the inlet from the corners of the tank. Alternate methods like changing the loop tank shape and size, and/or adding a second de-aeration tank, were considered time-consuming and uneconomical due to the high cost of NaI, but could provide interesting effects in research in the future. Figure 5.8 shows how the fiber is put in the tank and the technical drawings of the basket.

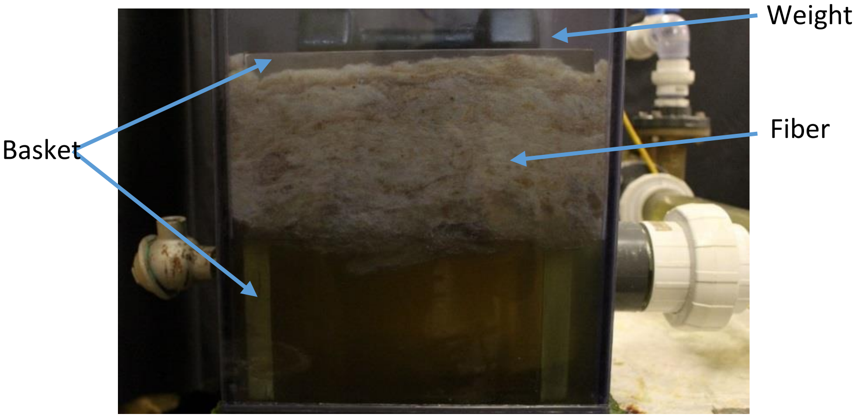

Figure 5.7 Fiber layer in the tank

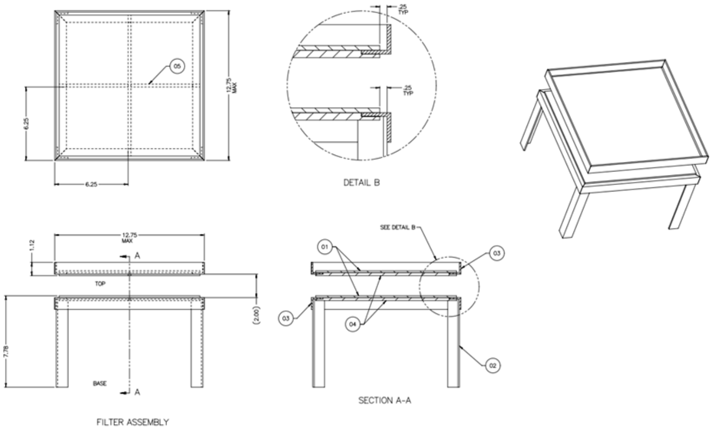

Figure 5.8 The technical drawings of the filter floss basket

5.6.4 Planes of Interest

The r-z plane was selected as the plane of interest for the PIV experiments. The different test locations in the r-z planes are shown in figure 5.10. Four different planes of interest were selected for PIV experiments in this study and the first plane is shown in Figure 5.10. The PIV data was taken in the plane in front of the air core as studying the air core using PIV is not possible due to the large reflections of the light sheet off of the air core which make measurement impossible. Using offset planes gives use the information about the flow around the air core. The air core was centered in all the test locations. The 1st test location was in the cylindrical part of the hydrocyclone. The second test location was in the 1st conical part of the hydrocyclone while the third and fourth test location were 2nd conical part of the hydrocyclone. The fields of view were centered with respect to the air core in the vertical direction.

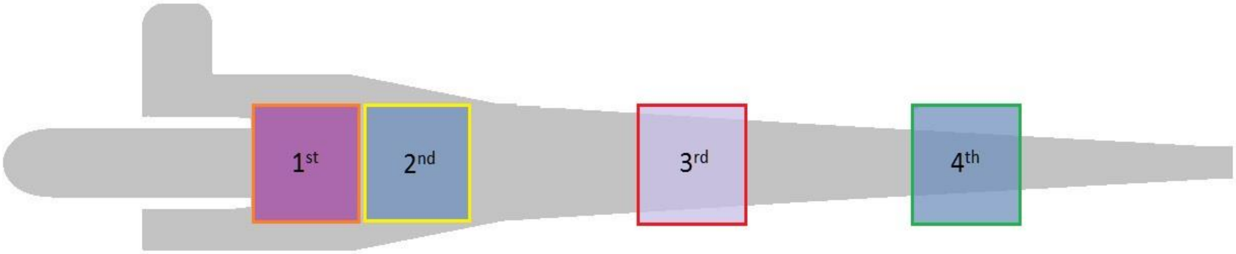

Figure 5.9 Test locations in the r-z plane

There were only four test locations possible due to the support structure and the glue which held the cyclone sections together. And due to lesser space available in front of the air-core as the cyclone tapers to the underflow. Figure 5.11 shows the support structure obstructing the other possible fields of view.

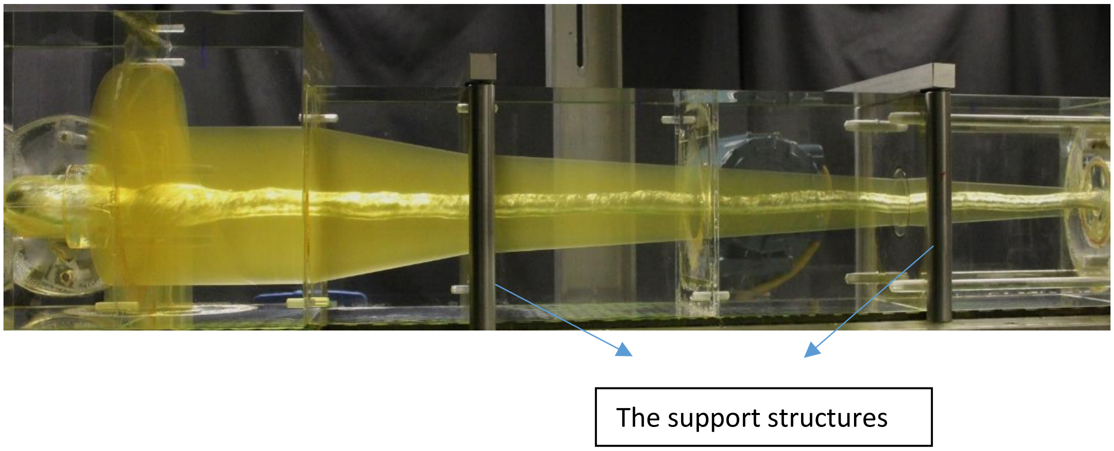

Figure 5.10 The Hydrocyclone support structure

5.6.5 Image Acquisition and Post Processing of the Data

The laser sheet was aligned to the desired location in front of the air core before acquiring images. The positions are shown in the Figure 5.12.

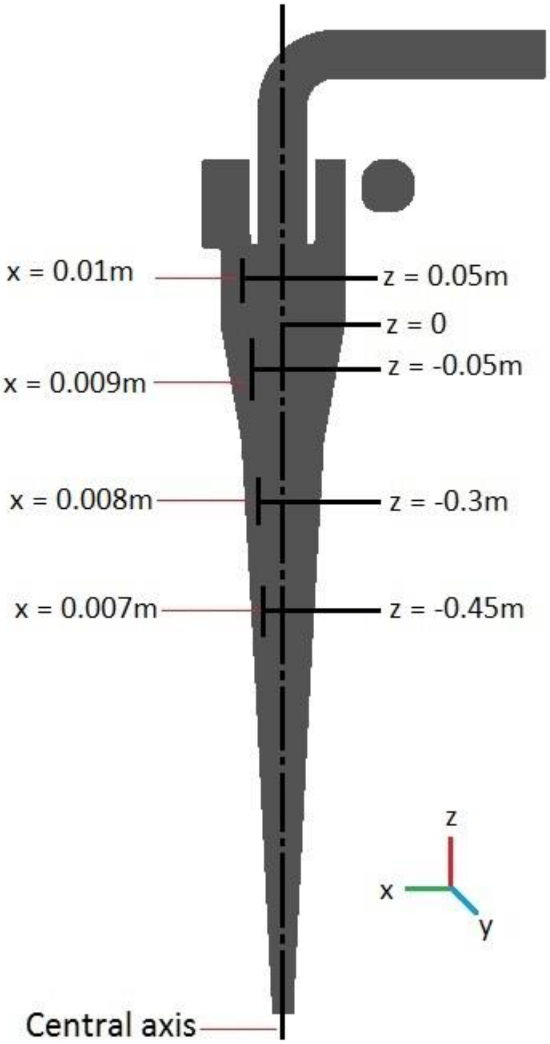

Figure 5.11 The different test locations and interrogation lines.

In order to push the solution through the overflow u-loop pipe section, the pump had to be to sped upto 30 Hz starting from 10 Hz with increments of 5Hz. Once the flow becomes stable, the pump is brought down to 20 Hz which is the working speed for the PIV experiments. A stable air core can be observed at 20 Hz speed. Next the laser is turned on and the attenuation is set to 0.999. Next the laser is switched to stand by and PIVACQ software is opened with the default settings. The inter-frame time has to be calculated and manually entered into the PIVACQ.

In the timing settings interface, the Q-Switch 1 and Q-Switch 2 were 170 µs; the frame Offset was 250 µs. The inter-frame time is the time interval between image acquisitions, and the Q-Switch time delays control the time after the flash lamp. The laser output pulse energy can be controlled by changing the Q-switch time delay. (Wernet, 2005)

A total of 800 image pairs were obtained in the software. The image were later post processed by the software PIVPROC which generated the vector files for the obtained image pairs. The vector files were read and compiled into one file using a data reduction program written in MATLAB (Sankovic, 2005). The output file had the average velocity values and vectors from all the prior outputs. This output file is later opened in Tecplot Focus 2016 in order to read the velocity vector maps.

5.6.6 Calculation of the Appropriate Inter-frame Time

To achieve proper cross-correlation, the inter-frame time has to be carefully calculated. The correlation sub-region and the velocity magnitude in the current field of view determines the inter-frame time. The sub-region size must obey one quarter rule, which specifies the maximum particle displacement has to be no more than a quarter of the sub-region size. The equation used to calculate the inter-frame time is Equation, 5.11:

$$\Delta \mathrm{T} = \frac{16 * \mathrm{FOV}}{1018 \mathrm{~x~} \mathrm{V_m}} \qquad (5.11)$$

Where V_m is the largest velocity magnitude of particles, which was predicted in the simulations, 16 is the maximum number of pixels of displacement, and 1018 is the number of pixels vertically on the CCD camera array. The field of view had the same dimension of 32.5mm by 32.5mm for all the four test locations. The inter-frame time was set to 160 μs, after testing different inter-frame times. For every inter-frame time 10 image pairs were obtained and post processed. A slight change in the inter-frame time did not show a large difference. The selected value was chosen based on the mathematical calculations and the testing trial and error. It was a very time consuming work, but since the inter-frame time plays a vital role in the outputs, it was required to get good data. These works were done before to the official data acquisitions, the results of which are presented in chapter 7.

CHAPTER 6

AIR CORE DIMENSIONS

6.1 Imaging System

The air core development was also observed in the experiments. The shape and dimensions of the air core were measured by attaching a grid paper behind the hydrocyclone. A Cannon DSLR camera was used to capture the images of hydrocyclone running with the air core. These pictures were used to calculate the shape of the air core using the grid paper. This experiment was performed using NaI as well as water as the test fluid.

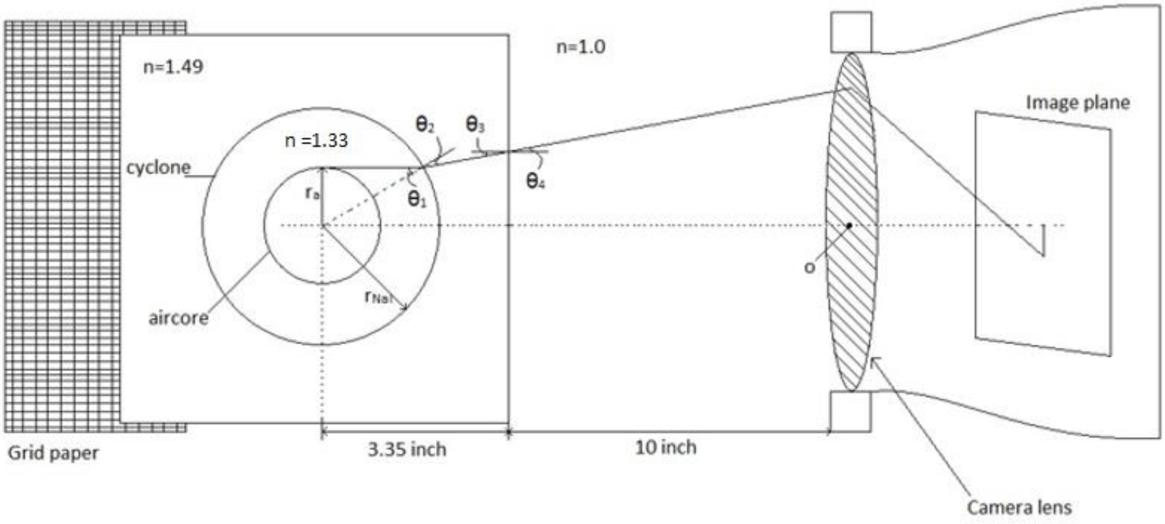

Figure 6.1 Imaging system

6.2 CFD

A different mesh was used for these parts of the experiment. A slightly coarse mesh was used which might have introduced some numerical errors. The LES model gave an inlet pressure of 10956 Pa (1.59psi) which is very close (9% difference) to the inlet pressure of 12031 Pa (1.745psi) measured during the experiment for NaI solution. The development of an air core was observed in the central area of the hydrocyclone. Following were the boundary conditions used for simulation in this section.

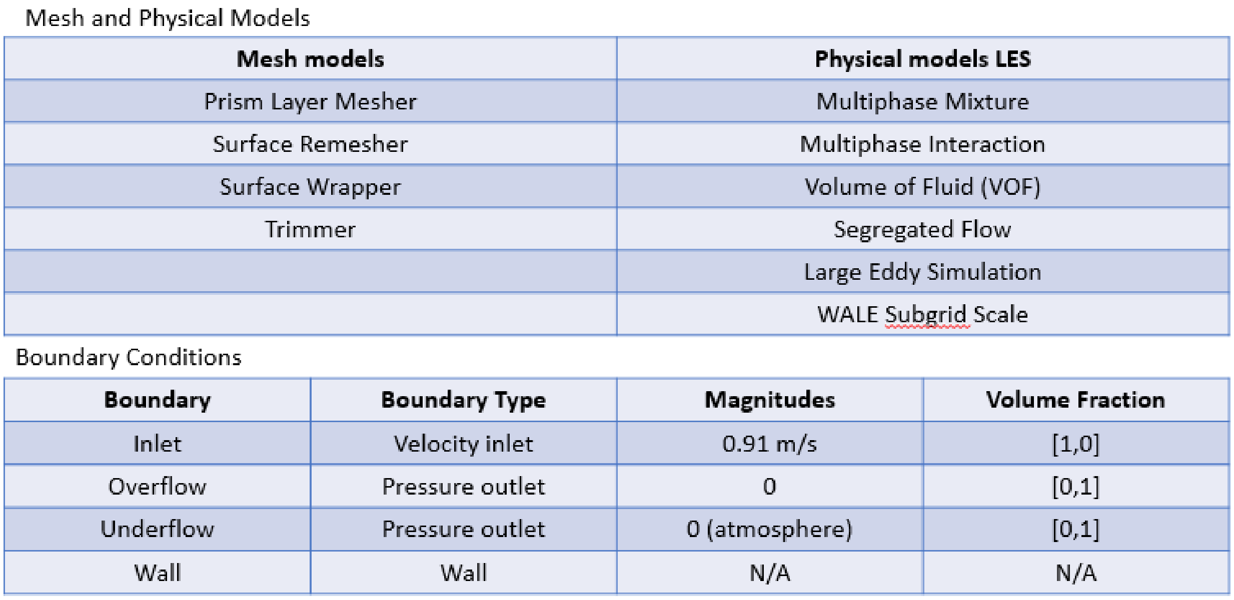

Mesh and Physical Models

Mesh models	Physical models LES
Prism Layer Mesher	Multiphase Mixture
Surface Remesher	Multiphase Interaction
Surface Wrapper	Volume of Fluid (VOF)
Trimmer	Segregated Flow
	Large Eddy Simulation
	WALE Subgrid Scale

Boundary Conditions

Boundary	Boundary Type	Magnitudes	Volume Fraction
Inlet	Velocity inlet	0.91 m/s	[1,0]
Overflow	Pressure outlet	0	[0,1]
Underflow	Pressure outlet	0 (atmosphere)	[0,1]
Wall	Wall	N/A	N/A

Figure 6.2 Boundary conditions for CFD

6.3 Air core measurements for NaI solution

The results are presented Figure 6.3 to Figure 6.7.

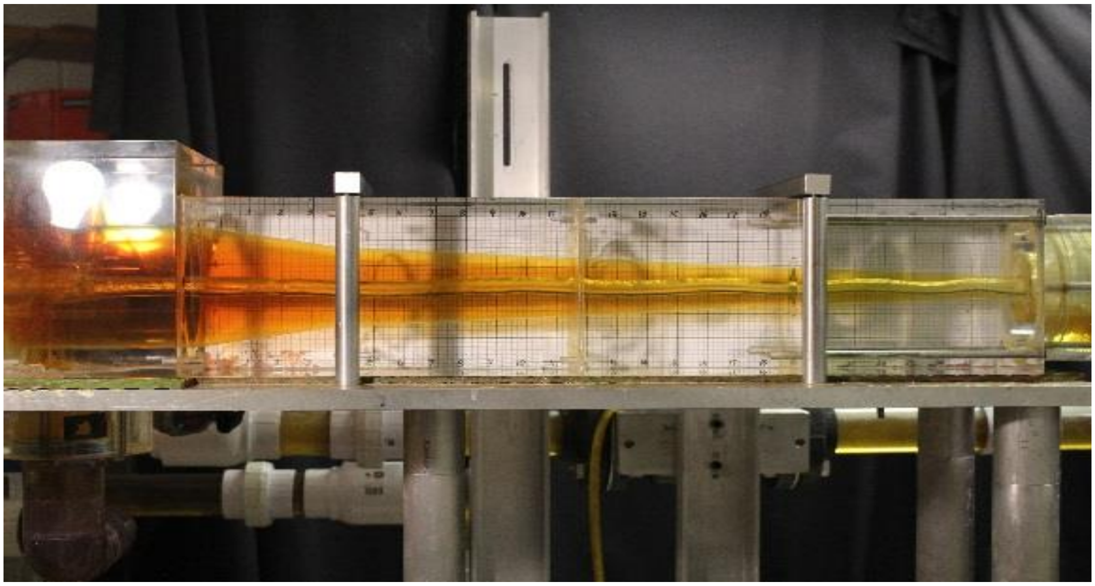

Figure 6.3 Air core formation using NaI

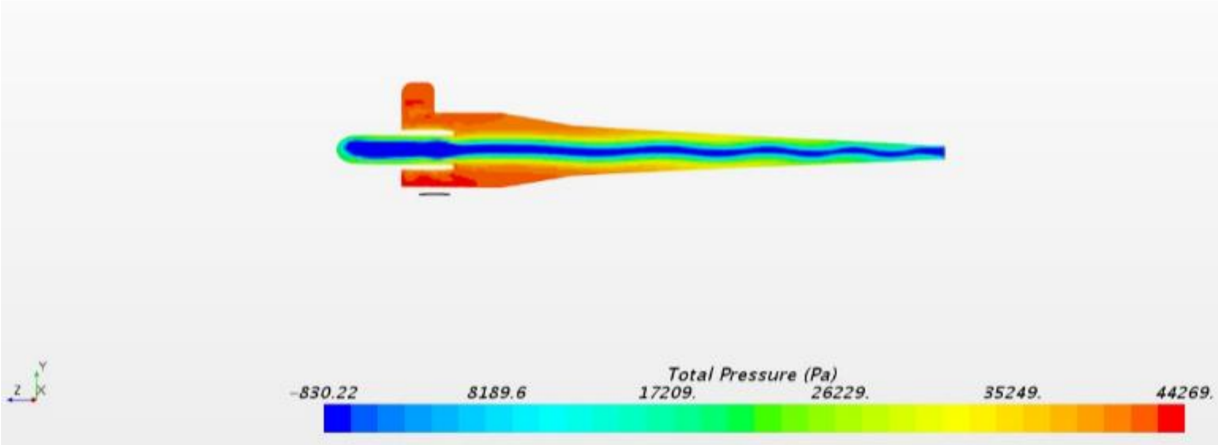

Figure 6.4 Total Pressure contour for NaI solution

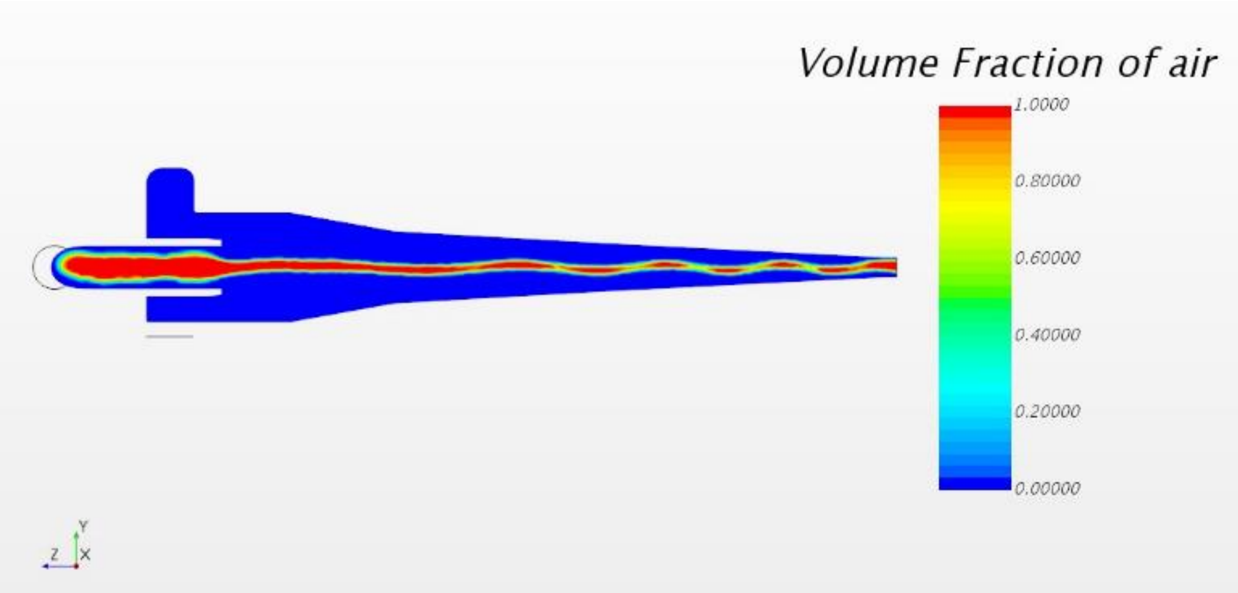

Figure 6.5 Volume fraction of air for NaI solution

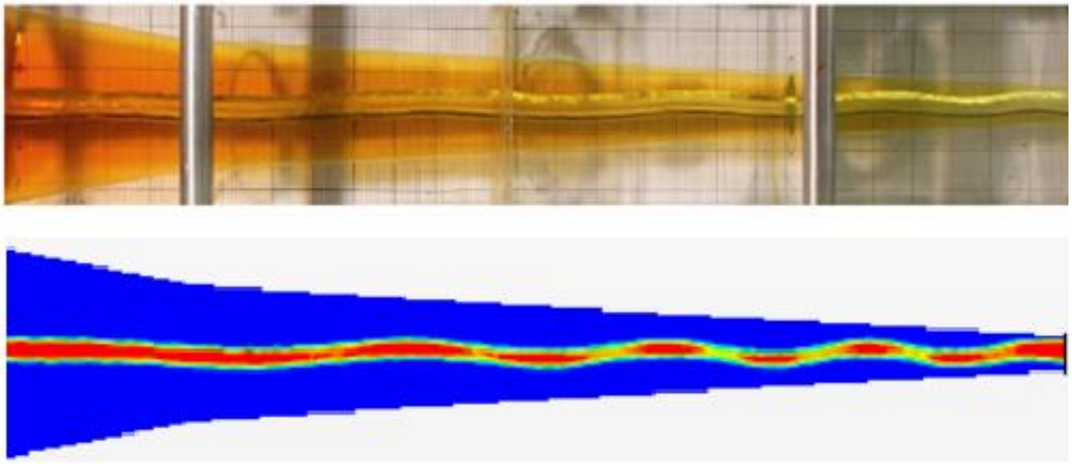

Figure 6.6 One to one comparison of the air core in NaI

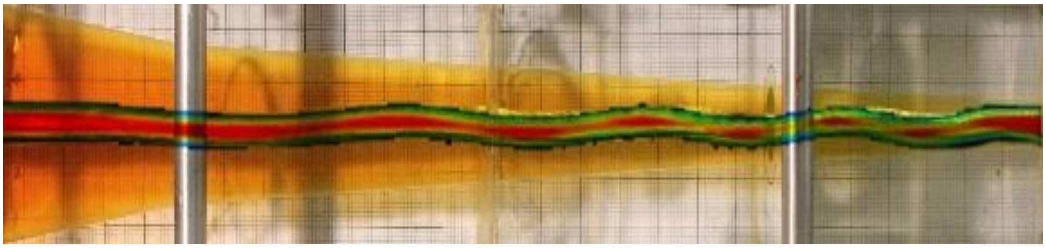

Figure 6.7 Superimposition of the air core in NaI

As can be seen from the figures above, the dimensions of the air core can be predicted using the grid paper. The images also show a perfect similarity to the CFD result of the air core. The superimposition of the CFD air core on the actual image shows complete similarity between the experimental and computational results.

The following charts shows the air core shape and dimension as obtained from the CFD and Grid paper. The z = 0 is located at the beginning of the conical section while z = 25 is the location of the underflow of the hydrocyclone. The blue (experimental) and the grey (computational) lines represents the upper limit of the air core and the orange (experimental) and yellow (computational) lines represent the lower limit.

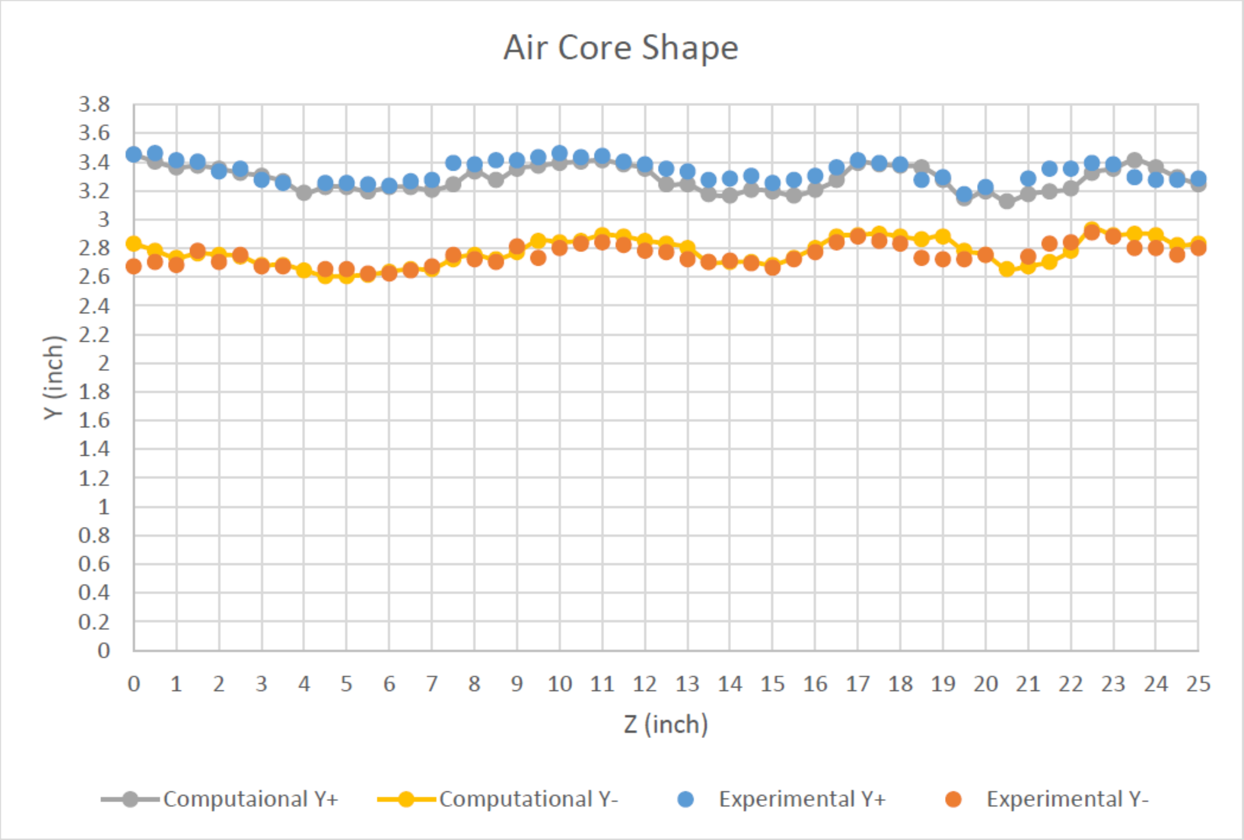

Figure 6.8 Air core shape for NaI Solution

6.3 Air core measurements for Water

A similar study was performed using water a test fluid. The results are presented below.

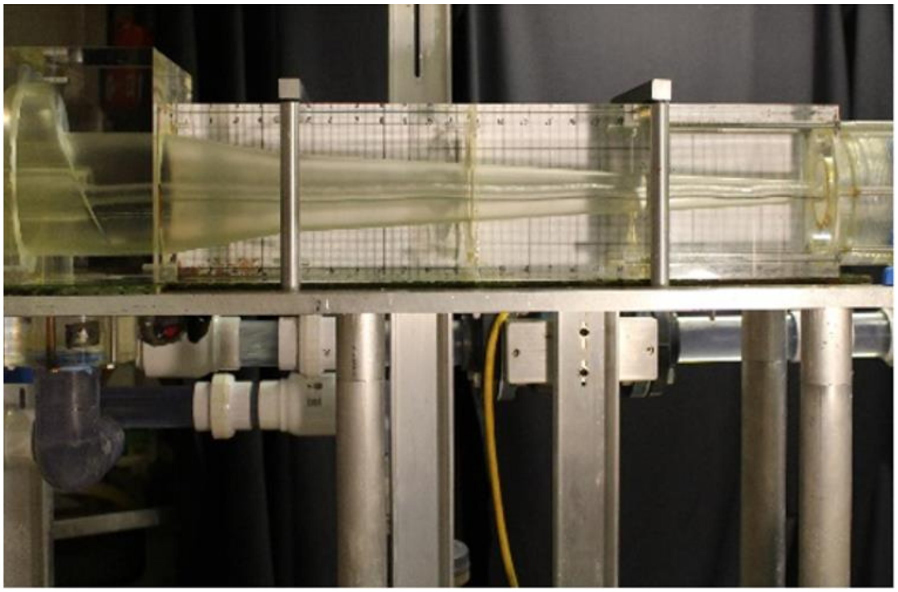

Figure 6.9 Air core formation using Water

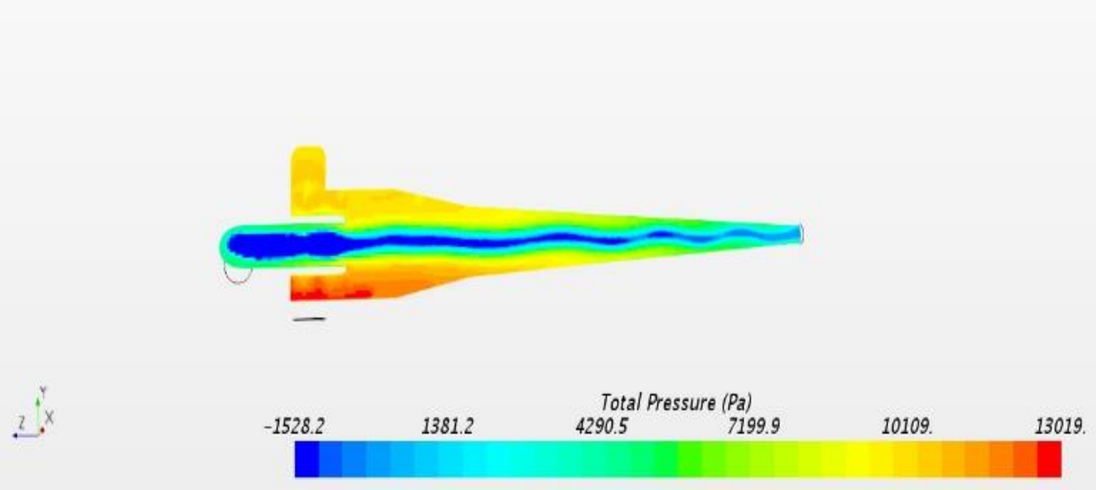

Figure 6.10 Total Pressure contour for Water

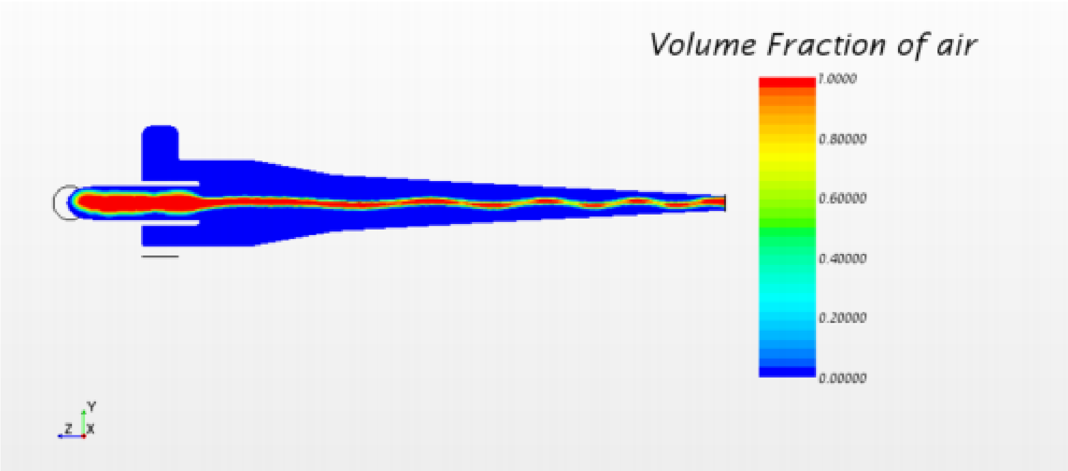

Figure 6.11 Volume fraction of air for Water

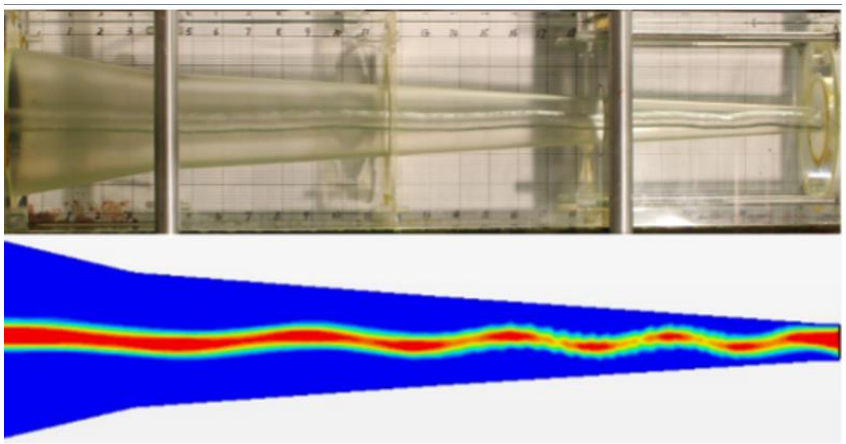

Figure 6.12 One to one comparison of air core in Water

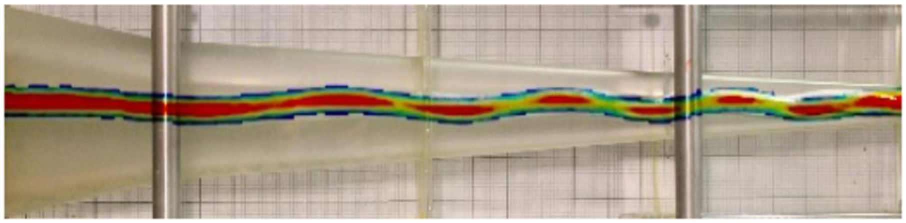

Figure 6.13 Superimposition of air core in Water

The superimposition of the air core when water is used as the test fluid shows great similarity. However, since the refractive index of water and the acrylic material of cyclone is not the same, the images obtained are not accurate. The grid paper has a slight shift due to the varying refractive indices. The air core shape and diameter was predicted by performing mathematical calculations for the refractive indices.

The following charts show the shape and diameter of the air core after calculations. The blue (experimental) and the grey (computational) lines represents the upper limit of the air core and the orange (experimental) and yellow (computational) lines represent the lower limit.

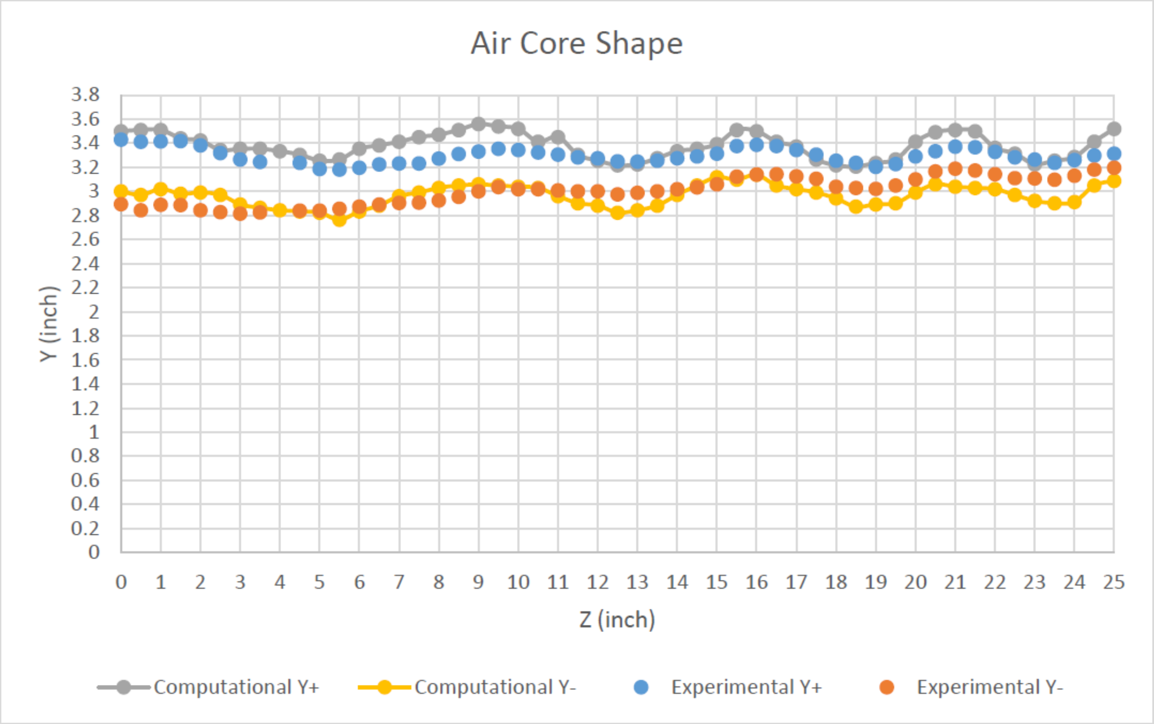

Figure 6.14 Air core shape for Water

CHAPTER 7

PIV RESULTS AND DISCUSSION

The r-z test plane was divided into four field of views and different location along the hydrocyclone. The results for every field of view will be presented. The VFD was set to 20Hz and the inlet flow rate recorded was 29.5±2 GPM for all the four test locations when taking the PIV data.

7.1 Velocities on the Radial-Axial Plane

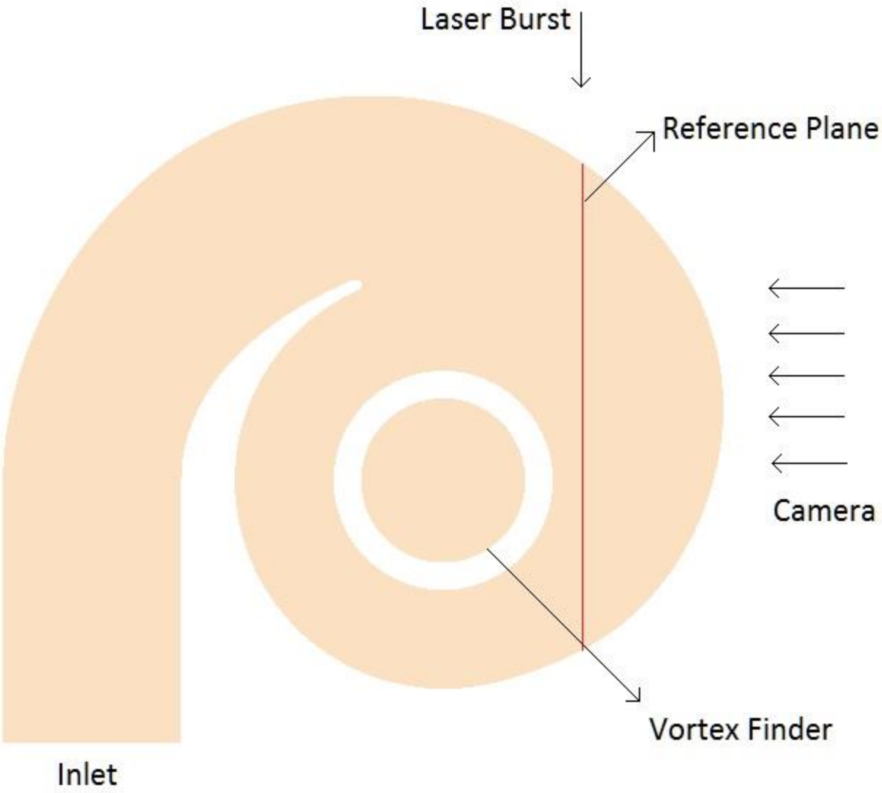

Figure 7.1 The reference plane 1, 10mm from the vortex finder.

Figure 7.1 shows the first plane of interest investigated in the PIV experiments; the model hydrocyclone was mounted horizontally. A typical hydrocyclone is mounted vertically.

Therefore, words such as “top, bottom, below and above” etc., are also used in the following text to denote different axial locations (as if the cyclone were mounted vertically).

The position of this plane is at 0.01 m offset from the central axis of the hydrocyclone, just in front of the air core. The air core is set at the center of the viewing angle. The direction of the laser bursts is also presented in the figure. PIV cannot be used to study the air core as it causes scattering of the light due to difference in the refractive index of air and NaI solution. Figures 7.2 through 7.15 present the PIV results for each section and the corresponding velocity vectors plot in the radial-axial plane.

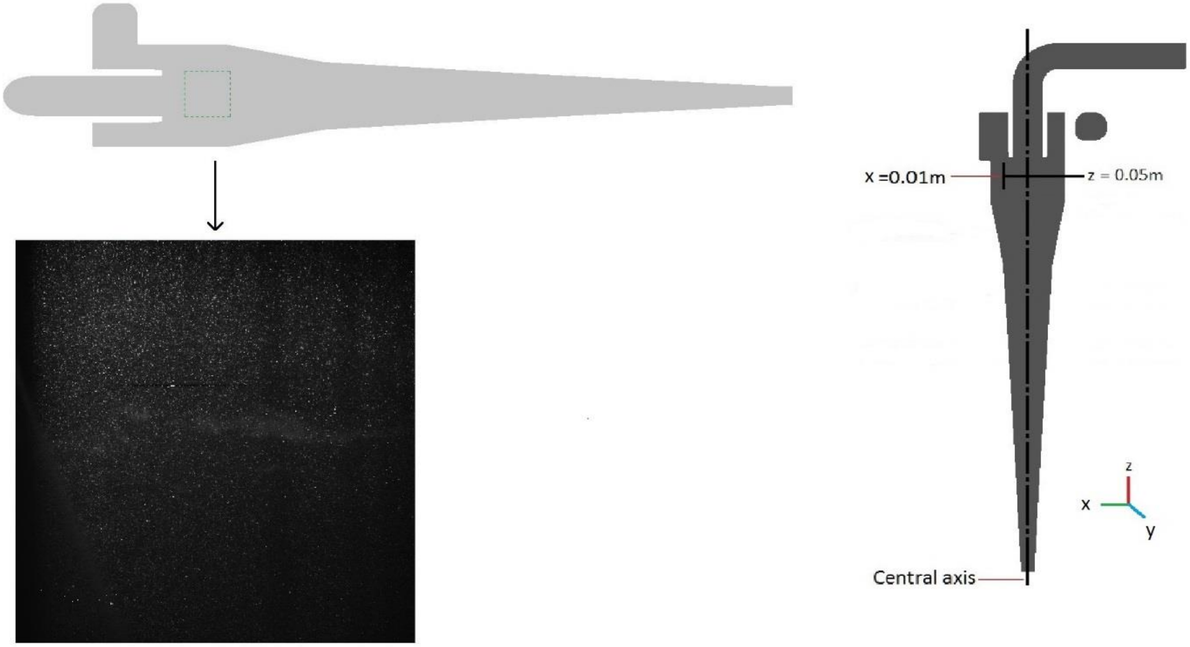

Figure 7.2 PIV image and the position of the 1st test location

The first test plane is located at 0.01 m offset of the central axis of the hydrocyclone and is offset from the air core. As discussed previously in chapter 4, section 4.7.4, the location of the 1st test plane is in the cylindrical section of the hydrocyclone. The above figure illustrates the position of the test plane. In the following figures, a “Q” in the legend indicates that the colored contour legend corresponds to the resultant magnitude of the two components of velocity (X and Y) measured in the PIV laser plane, while a “V” in the legend indicates that it is the vertical component of velocity in the laser plane, and a “U” indicates that it is a the horizontal component of velocity in the laser plane.

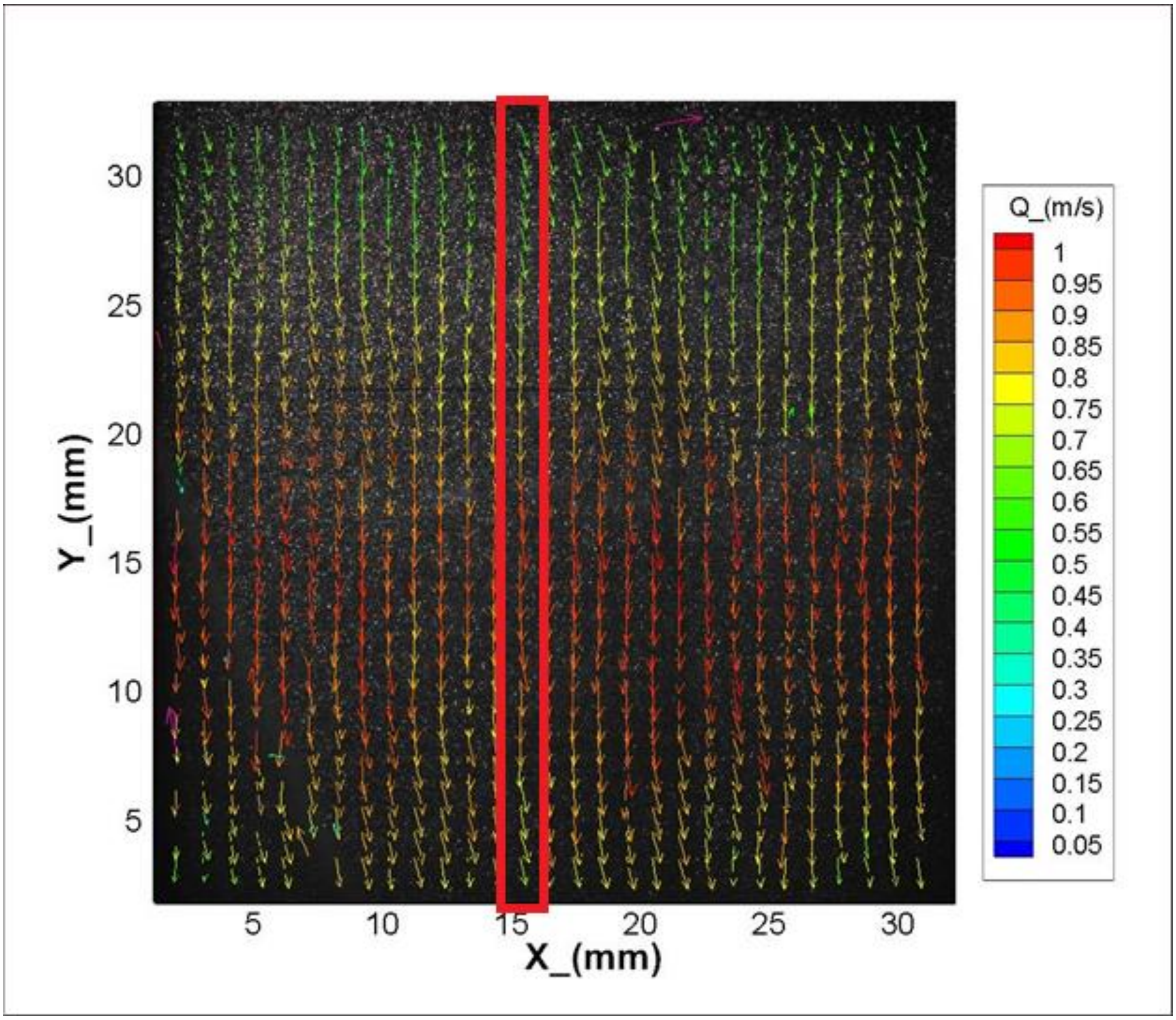

Figure 7.3 Velocity Vectors of the 1st test location

The PIV images were post processed using the commercial software Tecplot Focus 2016. This facilitated the creation of contour maps for the two components of the velocity vectors which are in the plane of the laser light sheet. The black areas in figure 5.4 are parts of the contour map which produced bad results due to air bubbles. The data used for validating the Star CCM results was taken at the center line of the contour as shown in the figure 5.3. Since there is no bad spots along the center line, the result can be used for validation. PIV measures the velocity components within the plane of the laser light sheet. As the FOVs were not located at the central axis of the cyclone, the PIV measurements are capturing velocities in the axial (seen as the horizontal direction in the following figures), as well as the combination of tangential and radial velocities (seen as the vertical direction in the following figures) in the plane of interest.

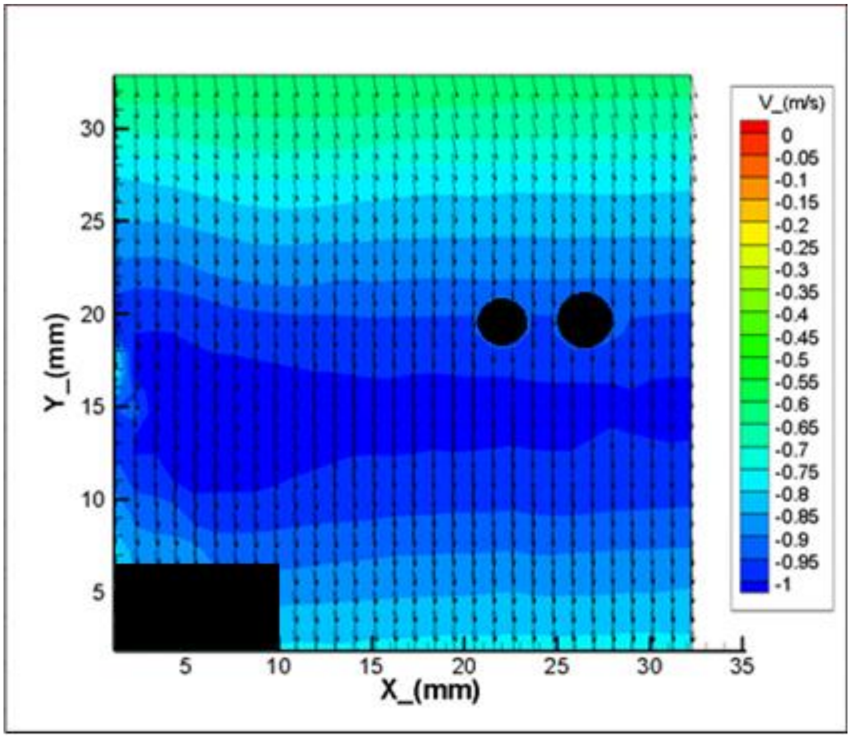

Figure 7.4 The combination of Tangential and Radial Velocity components contour of the 1st test location

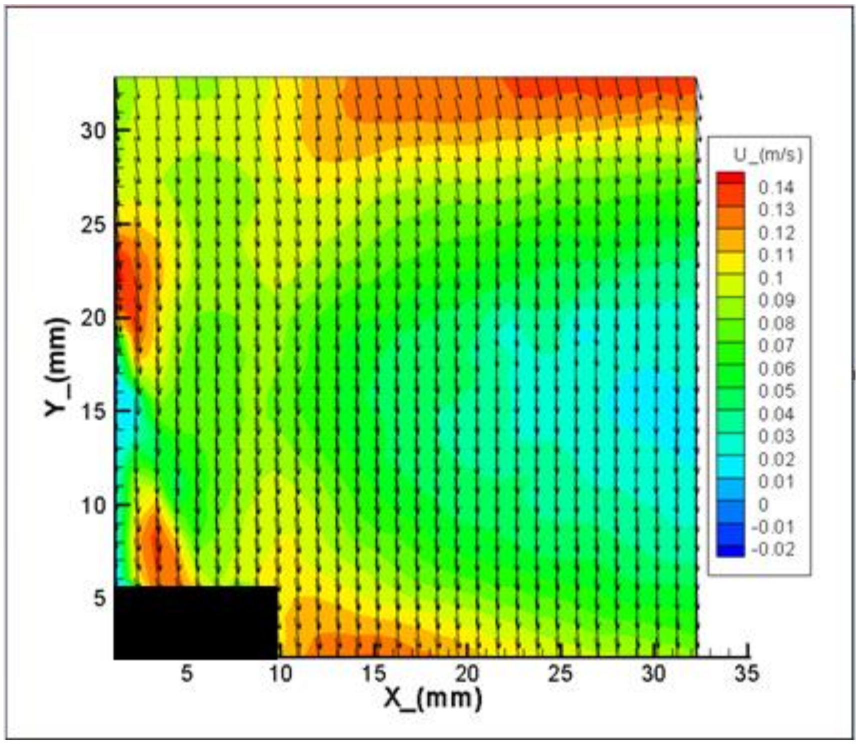

Figure 7.5 Axial velocity contour of the 1st test location

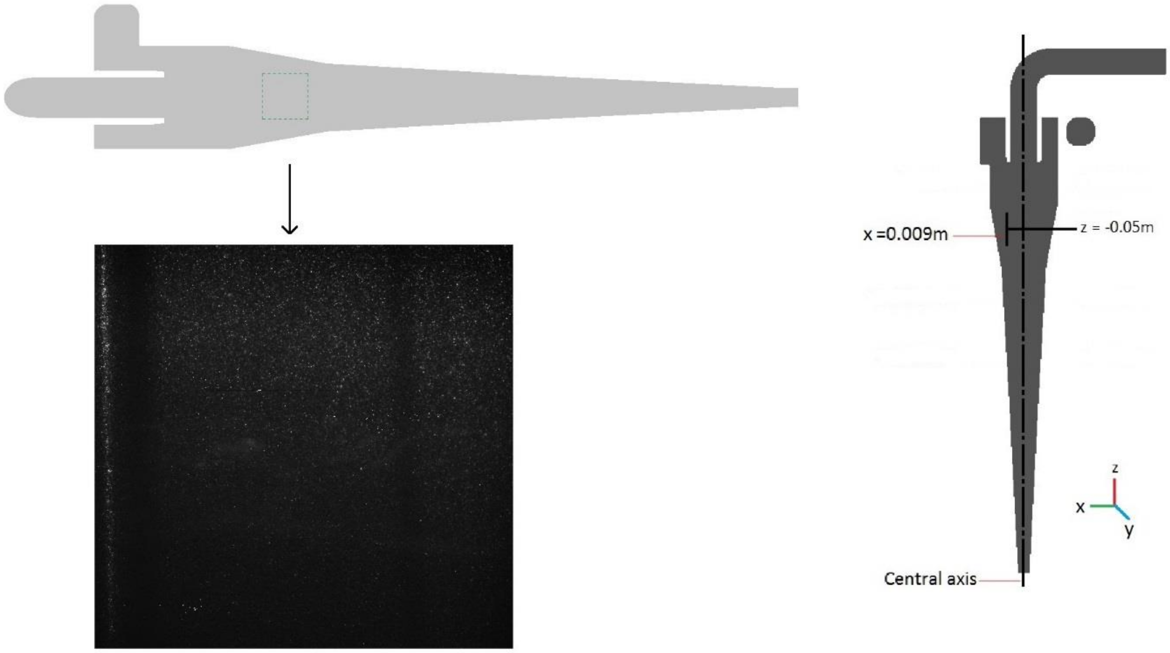

Figure 7.6 PIV image of 2nd test location

The 2nd test plane was located in the first conical section of the hydrocyclone. It was located at 0.009m away from the central axis. The plane had to be moved slightly back (away from the camera and towards the air core) due to the reducing diameter of the hydrocyclone as you move from the vortex finder towards the underflow. The above figure illustrates the position of the test plane.

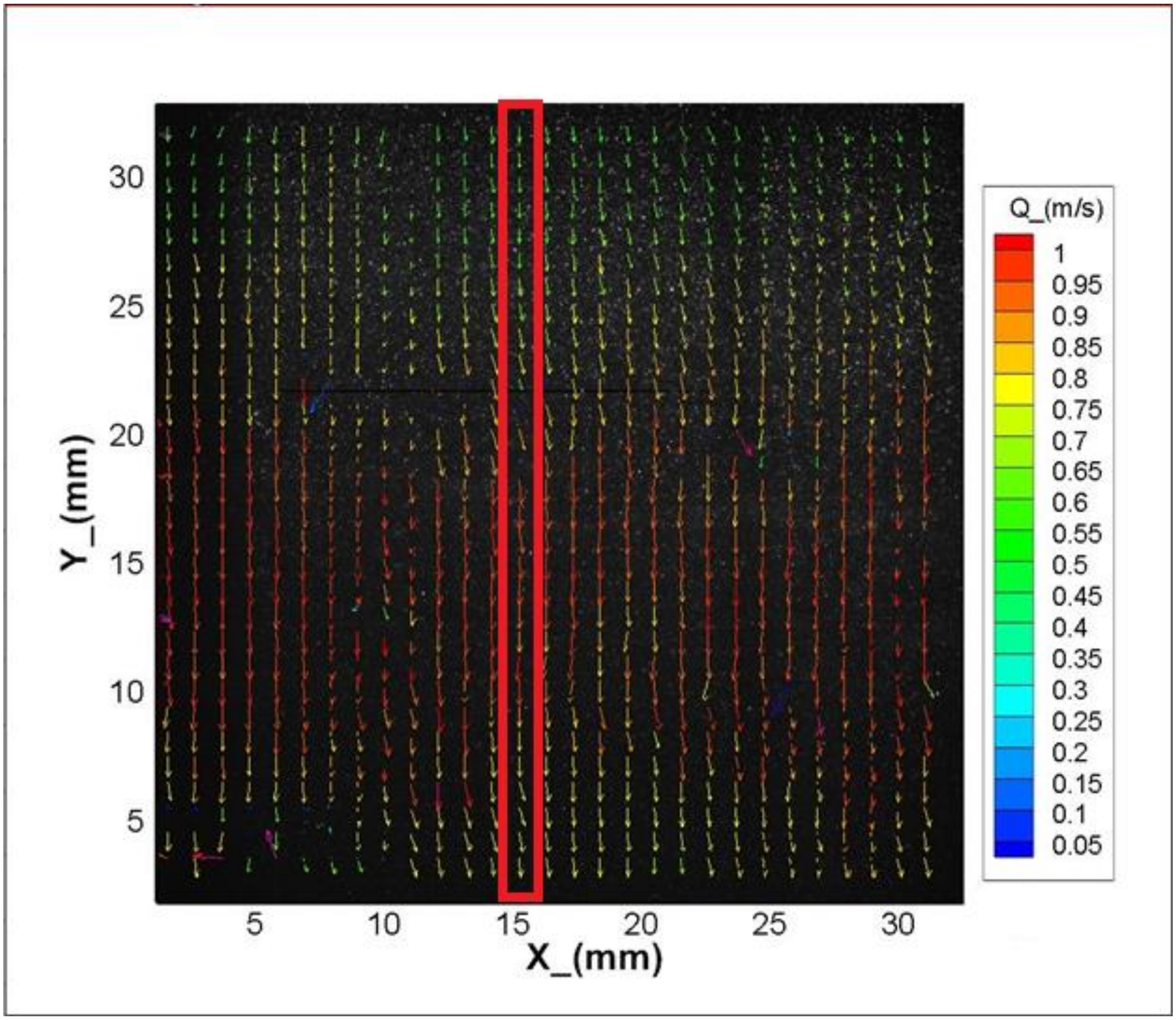

Figure 7.7 Velocity vectors of the 2nd test location

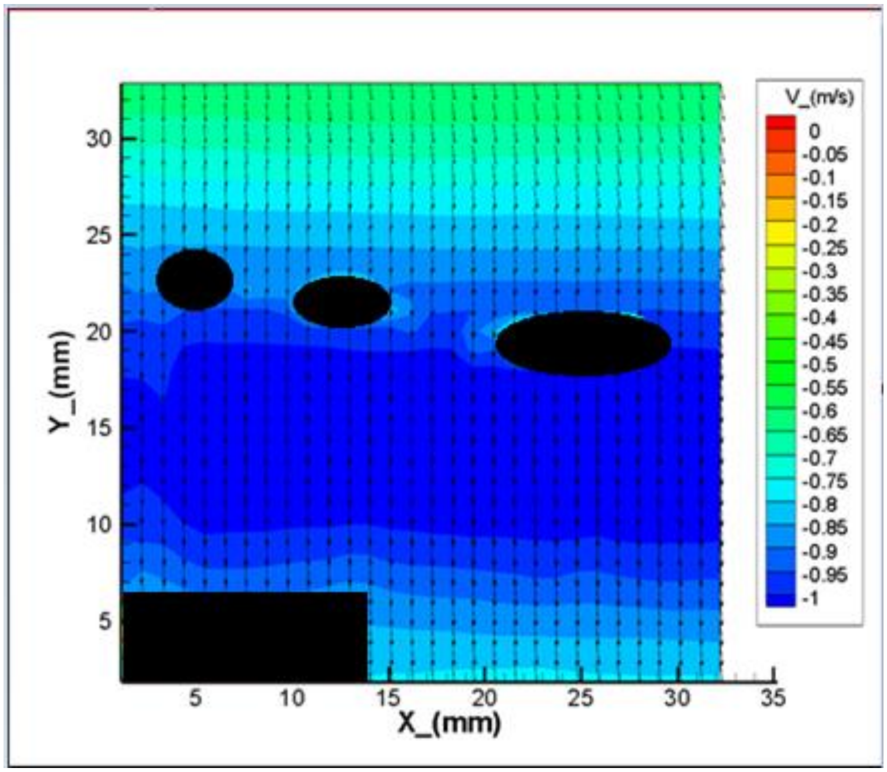

Figure 7.8 The combination of Tangential and Radial Velocity components contour of the 2nd test location al velocity contour of the 2nd test location

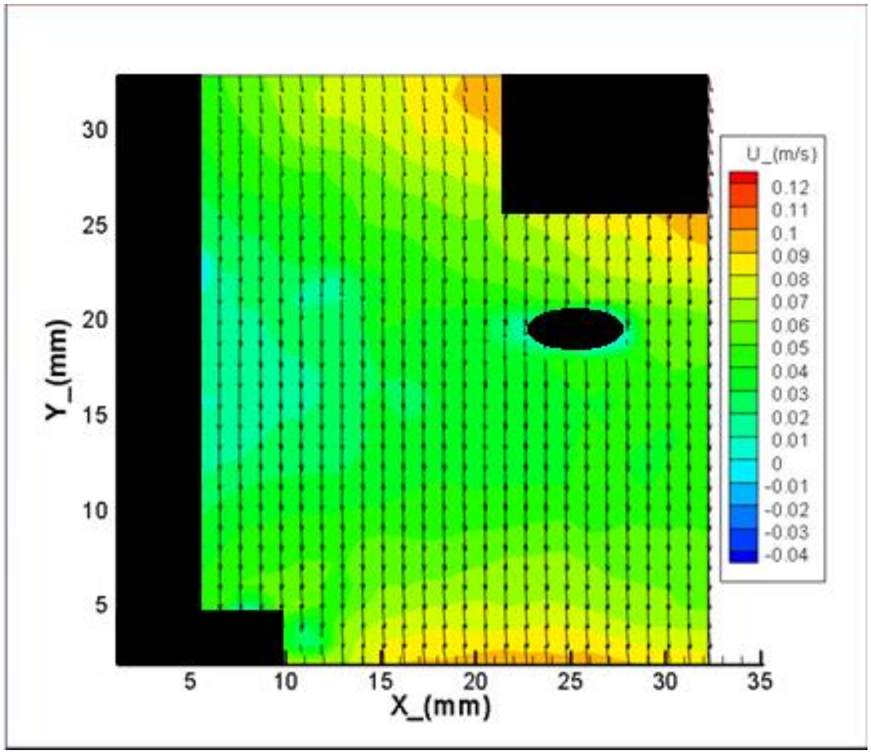

Figure 7.9 Axial velocity contour of the 2nd test location

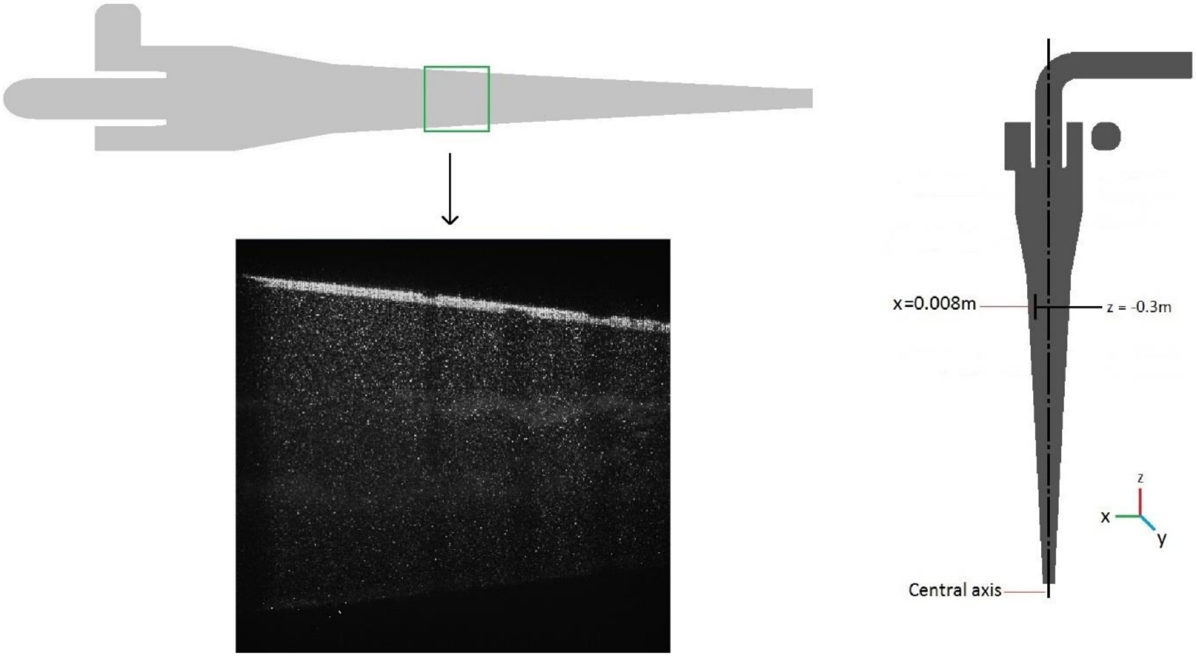

Figure 7.10 PIV image of 3rd test location

The 3rd test plane was located in the narrow conical of the hydrocyclone. It was located at 0.008m away from the central axis. The plane had to be moved slightly back due to the reducing diameter of the hydrocyclone. The Laser plane went outside the boundaries of the hydrocyclone and the diameter in this section was smaller than the height of the laser plane. The contour image maps the boundary of the hydrocyclone. The above figure illustrates the position of the test plane.

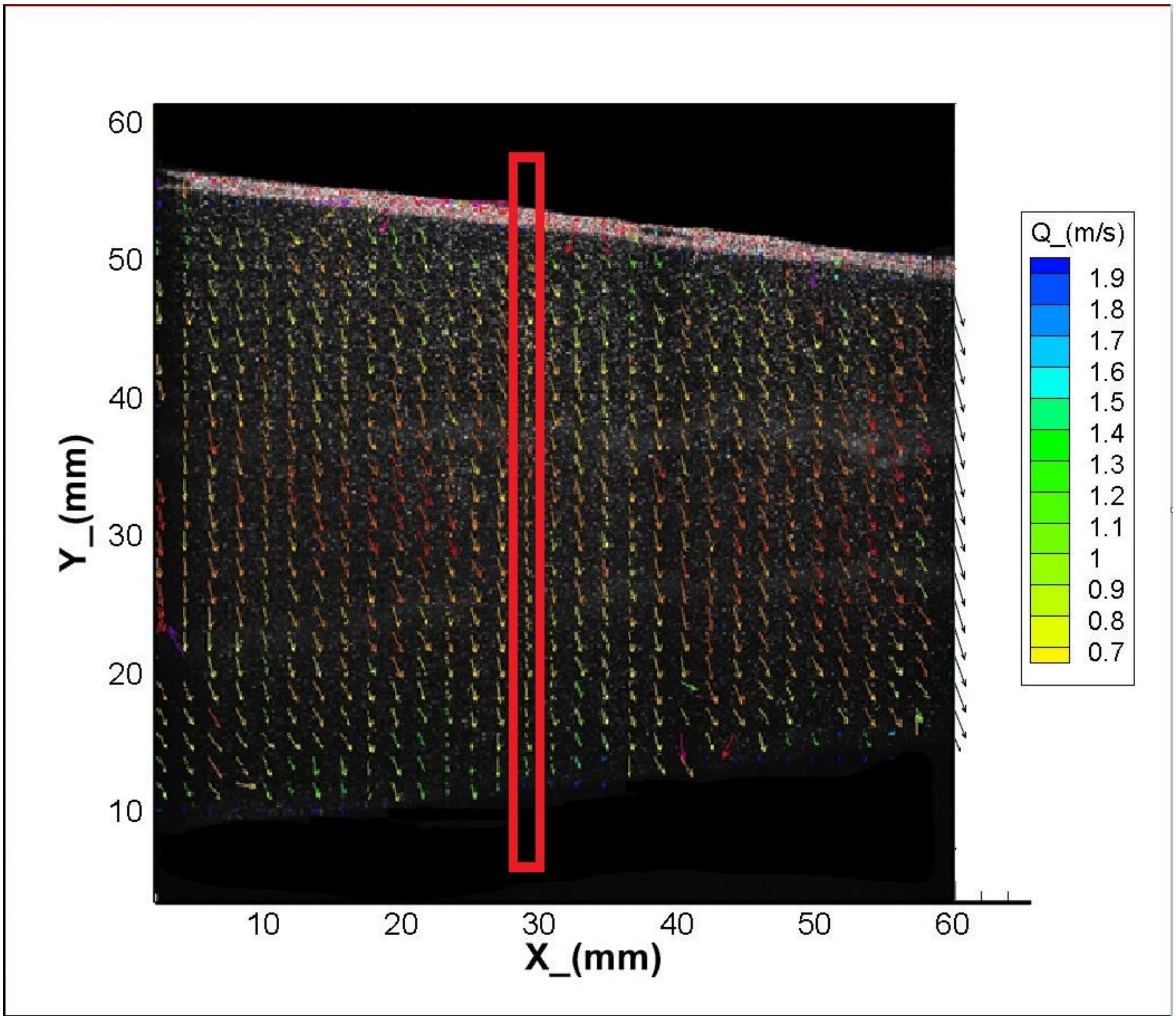

Figure 7.11 Velocity vectors of the 3rd test location

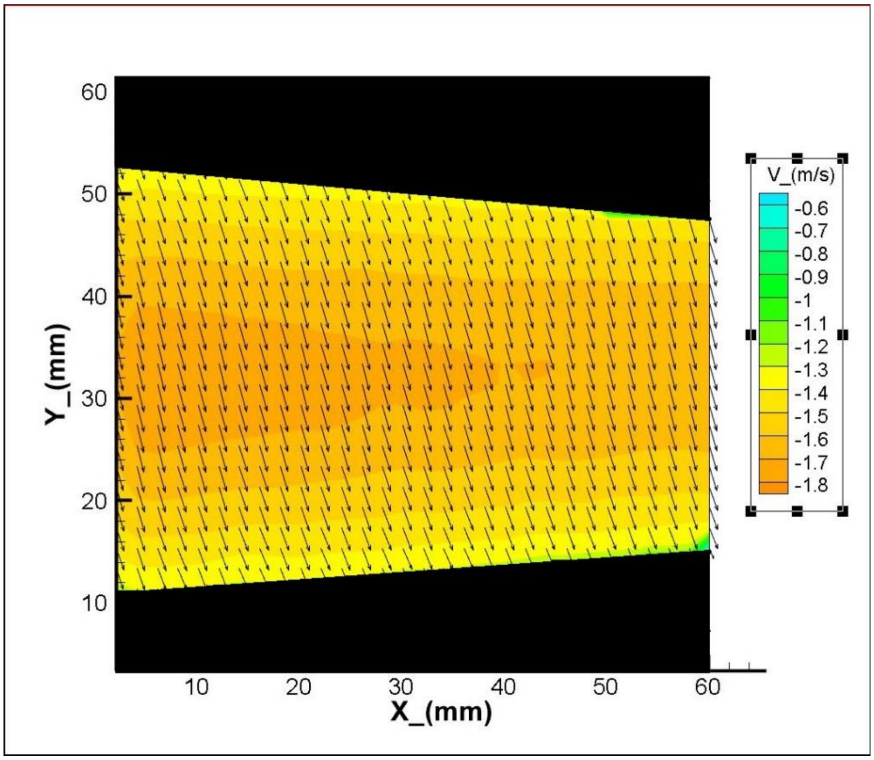

Figure 7.12 The combination of Tangential and Radial Velocity contour of the 3rd test location

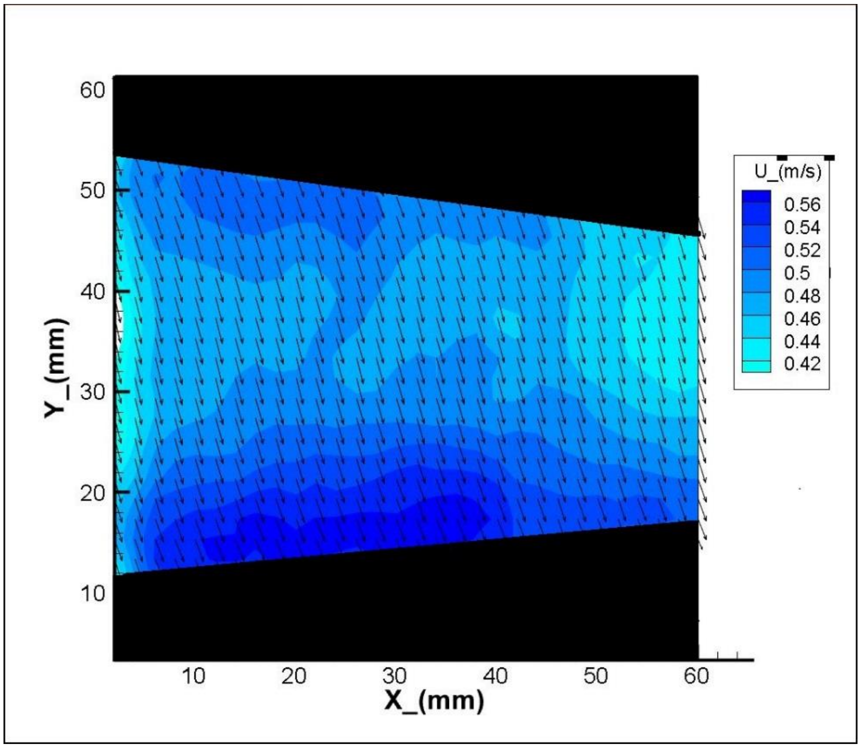

Figure 7.13 Axial velocity contour of the 3rd test location

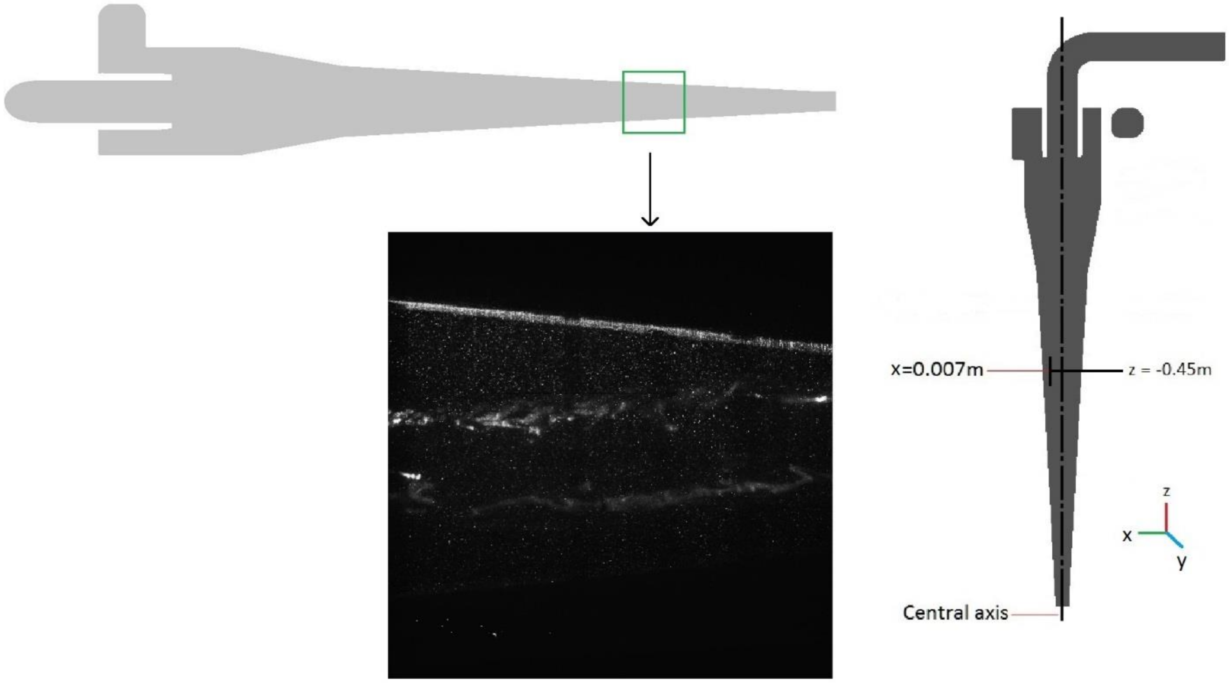

Figure 7.14 PIV image of the 4th test location

The 4th test plane was located closer to the underflow of the hydrocyclone. It was located at 0.007m away from the central axis. At this location there was very little space for the lase plane to fit into. Since this test location was located near the underflow, the air core interfered with the laser plane. The output has been presented below. Due to the heavy air interference, the contour map did not produce a good result. The above figure illustrates the position of the test plane. The air core is represented by the red boundary shown in the following figure.

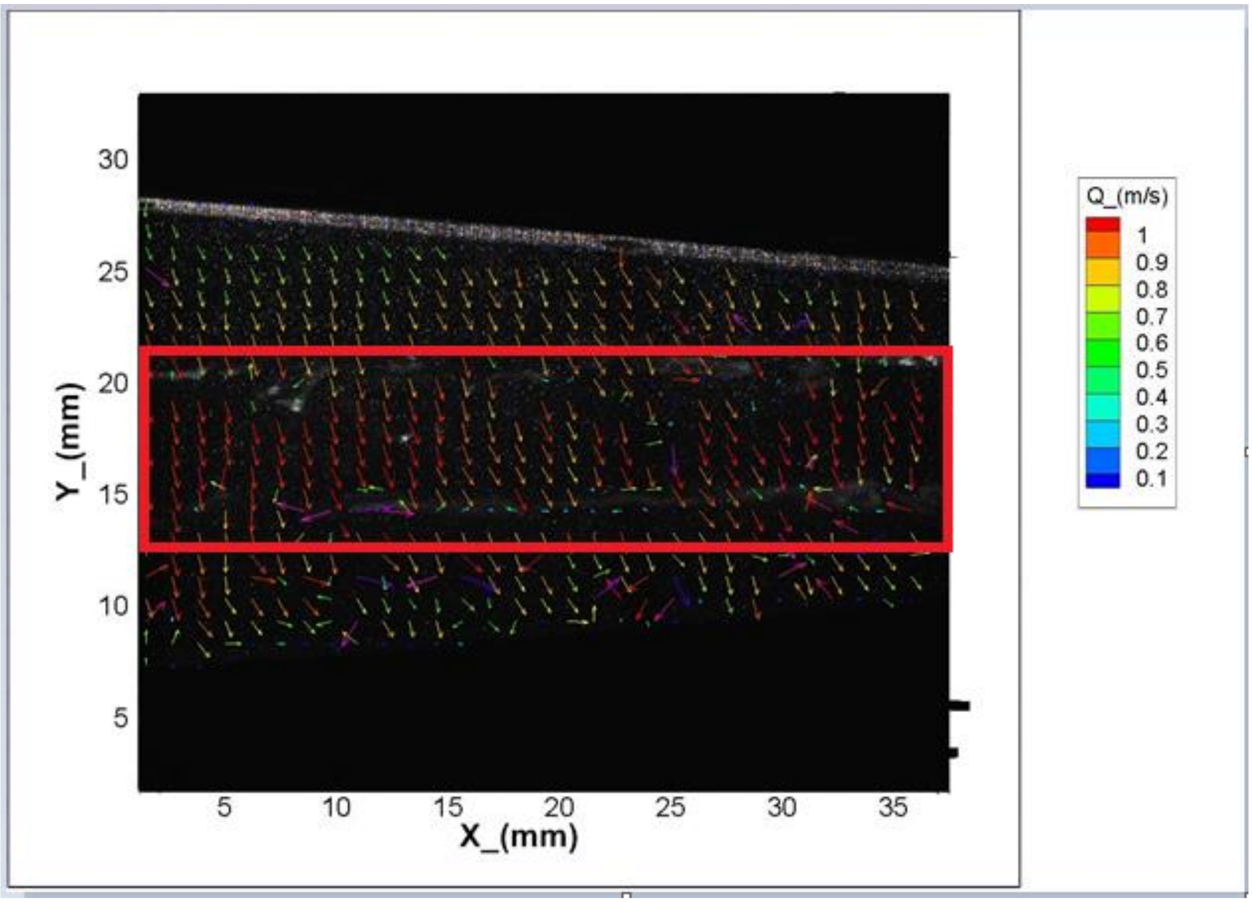

Figure 7.15 Velocity Vectors of the 4th test location

7.2 Flow Parameters at Inlet and Overflow Outlet

The new design of the hydrocyclone loop helped in obtaining important flow parameters. The pressure gauges located at the inlet and the overflow outlet were used for measuring the respective pressure values. The magnetic flow meter provided the inlet flow rate while the SONARtrac instrument provided the overflow flow rate through the inverted U-loop. The magnetic flow meter could also be installed within the U loop to measure the overflow flow rate. All of flow parameters were measured when the tank liquid-air interface height was 5 inches below the central axis of the underflow of the hydrocyclone, with the inverted U-loop installed and the loop filled, while the pump was running.

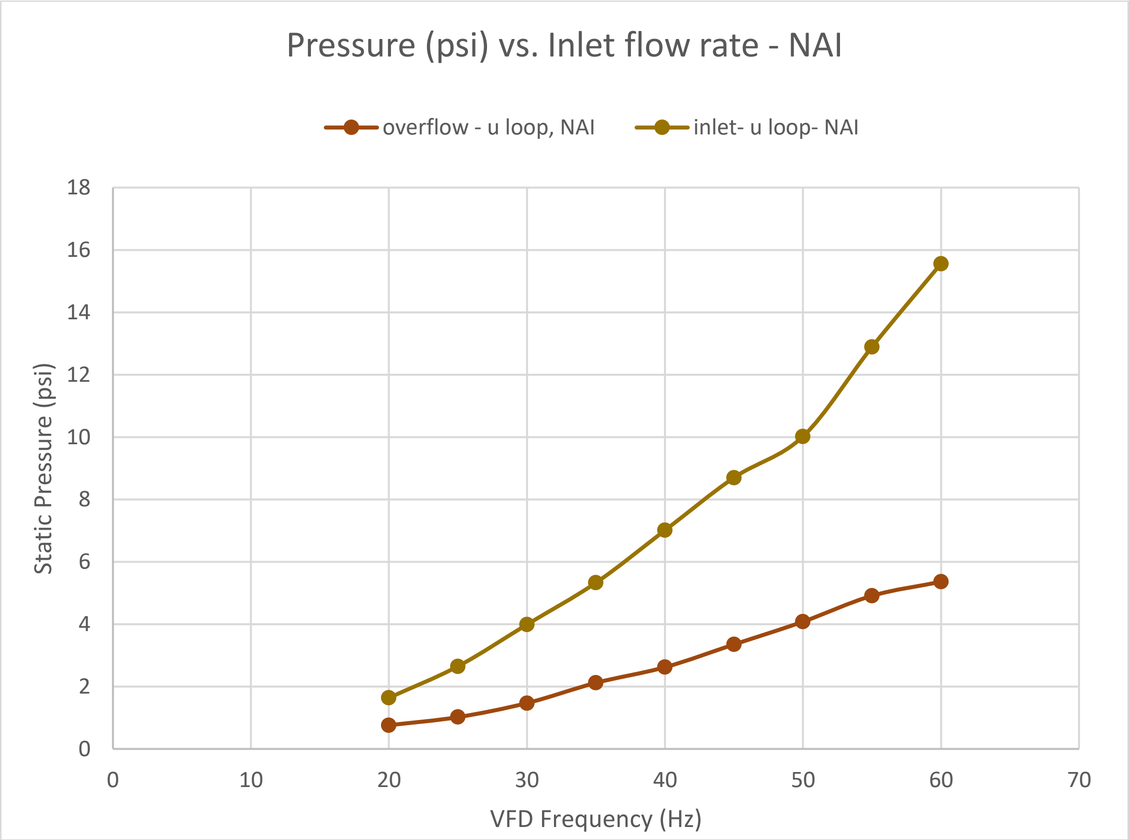

Figure 7.16 The inlet and overflow static pressure versus inlet flow rate with U-loop installed for NaI solution

Figure 7.16 shows the static pressures (Psi) of the inlet and overflow outlet measured by the pressure gauge. As can be seen in the figure, due to the back pressure created by the overflow piping, a non-zero, positive gauge pressure is present at the overflow outlet. The ratio of inlet static pressure to overflow static pressure stays approximately constant at a value of about 2.7. Figure 7.17 shows the inlet flow rate versus the VFD frequency. The following data was collected using the Magnetic Flow meter both at inlet and overflow outlet.

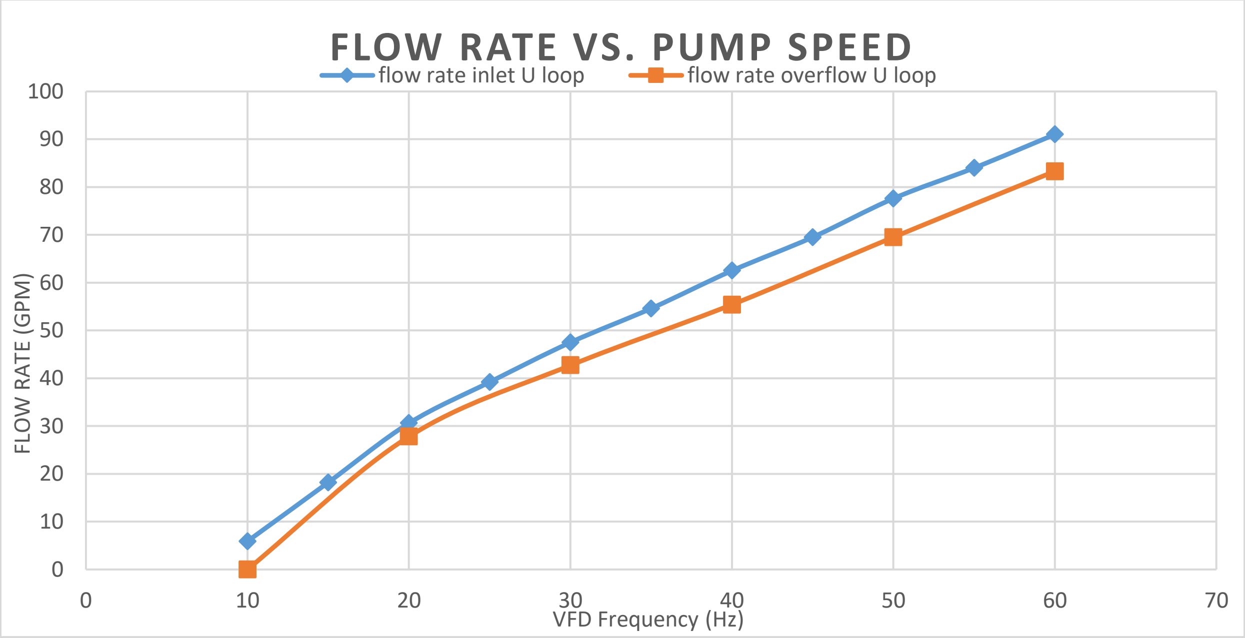

Figure 7.17 Inlet Flow and Overflow Flow Rate (GPM) vs VFD Frequency (Hz) for NaI, with U-loop installed in the overflow piping

As seen from above, the ratio of the inlet flow rate to the overflow flow rate with the U loop does vary as the pump speed is increased. The ratio of overflow flow rate to inlet flow rate is approximately 0.90, but the actual liquid ratio is less than that, since the air flow rate was included in the overflow flow rate in the measurement.

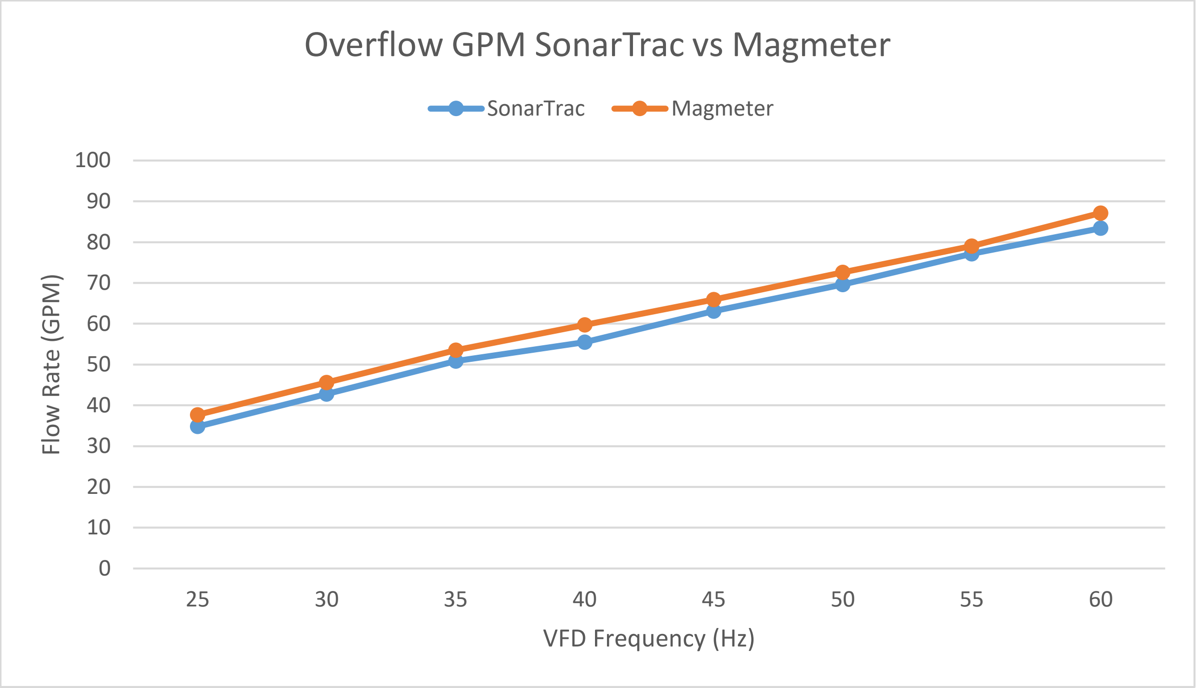

Figure. 7.18 Overflow GPM SonarTrac vs Magmeter Reading for NaI

The SonarTrac also had a flow rate measuring utility on it. The following graph will compare the overflow flow rate obtained from the magnetic flow meter and the SonarTrac in the U-loop section located downstream of the overflow of the hydrocyclone.

7.3 Uncertainty Analysis

The overall uncertainty of this study will be presented in this section which consists of two components, namely, the random uncertainty and systematic uncertainty and the value of the overall uncertainty is the root mean square of those two components.

In an experiment, both measuring instruments and changes in environmental conditions will result in unexpected variations which leads to random uncertainties (or errors). The random uncertainties in this study were calculated using the data reduction program mentioned previously. The code first eliminates the outliers which are the spurious velocity vectors from the data sets. Then the average velocities and standard deviations at each effective grid point are calculated using the following equations:

$$\overline{U}_{i,j} = \frac{\sum_{k=1}^{N_S} U_{i,j,k}}{N_S} \qquad (7.1)$$

$$S_{i,j} = \sqrt{\frac{\sum_{k=1}^{N_S}(U_{i,j,k}-\overline{U_{i,j}})^2}{N_S-1}} \qquad (7.2)$$

Where $U_{i,j,k}$ is the velocity components at every grid point, indices i, j and k denote the x direction, y direction, and the number of image pairs respectively, $S_{i,j}$ is the standard deviation, and N_s is the number of measurements taken. The standard deviation distribution is computed based on the value of mean velocity.

The relative random error for each point is calculated by assuming a Gaussian distribution with a 95% of confidence level:

$$\sigma_{\overline{u}} = 1.96\frac{S}{\sqrt{N_S}} \qquad (7.3)$$

Equation 7.3 computes an average value over the entire FOV in this study and then creates an output file. The random uncertainty value can be minimized by taking substantial image pairs, in this study, a maximum number of 800 image pairs were taken at each FOV.

The systematic uncertainty in this works was caused by the measuring instruments. It has no relationship to the number of measurements and in a PIV experiment, Wernet (2005) suggested that timing and displacement estimate are the two major factors of systematic uncertainty, and Equation 7.4 was given:

$$\frac{\sigma_u}{U} = \sqrt{\left(\frac{\sigma_t}{\Delta t}\right)^2 + \left(\frac{\sigma_x}{\Delta x}\right)^2} \qquad (7.4)$$

Where σ_t and σ_x are temporal and spatial uncertainties, and σ_u is the uncertainty in the velocity. The timing error of the Nd YAG laser is $2\text{x}10^{-9}$ seconds and the time interval for this study can be assumed to be on the order of 10^{-4} second and hence $\left(\frac{\sigma_t}{\Delta t}\right)$ is somewhere around $2\text{x}10^{-5}$. The uncertainty of the displacement measurement is approximately 0.1 to 0.2 pixels (Wernet & Pline, 1993), and Δx equals the maximum displacement, which was 16 pixels in this experiment, this can be calculated by Equation 7.5:

$$\sigma_u/U = 0.2/16 = 1.25\ \% \qquad (7.5)$$

The temporal uncertainty is relatively very small compared to the spatial uncertainty and it is negligible and the relative systematic uncertainty for this study is 1.25%. The total uncertainty can be calculated by Equation 7.6:

$$\frac{\sigma_{total}}{U} = \sqrt{\left(\frac{\sigma_{system}}{U}\right)^2 + \left(\frac{\sigma_{random}}{U}\right)^2} \qquad (7.6)$$

Table 7.1 is the list of the random, systematic, and total uncertainties associated with each FOV.

Test location	Calculated average random uncertainty (%)	Relative systematic uncertainty (%)	Total average uncertainty (%)
1	1.7	1.25	2.11
2	4.1	1.25	4.29
3	2.6	1.25	2.88
4	2.2	1.25	2.53

Table 7.1 Uncertainties associated with each FOV

As presented in the table, total average uncertainties of each field of view are all lower than 5%, which means that the error in the experiments is acceptable and the PIV data are reliable.

The following table describes the uncertainties associated with all the mechanical devices used for measurements.

Device Name	Uncertainty (%)
Magnetic Flow Meter	±6.67
Pressure Gauges	±0.5
SONARtrac	±6.79

Table 7.2 Uncertainties associated with Mechanical Devices

7.4 Comparison with the Computational Results

In this section, the fluid velocities measured and calculated through PIV experiments will be used to validate and compare the computational results both at the global level and the local level.

7.4.1 Global Validation of CFD Results and PIV

In the experimental works, inlet static gauge pressure and inlet velocity were measured to be 1.883 psi and 0.94 m/s respectively. The computational works calculated an inlet static pressure of 1.615 psi. The predicted values of pressure by CFD shows a 14 % difference with the experimental measurements. Based upon the PIV data from cyclone inlet, an average velocity magnitude of 1.006 m/s was calculated, and the corresponding calculated flow rate at the inlet is 30.3 GPM. The inlet flow rate measured by the magnetic flow meter is 29.5±2 GPM, hence, the difference between the flow meter measurement and the PIV is 2.7%, and it is considered acceptable.

7.5 Validation of CFD results based on local flow velocities

7.5.1 Comparison of Velocity Distributions

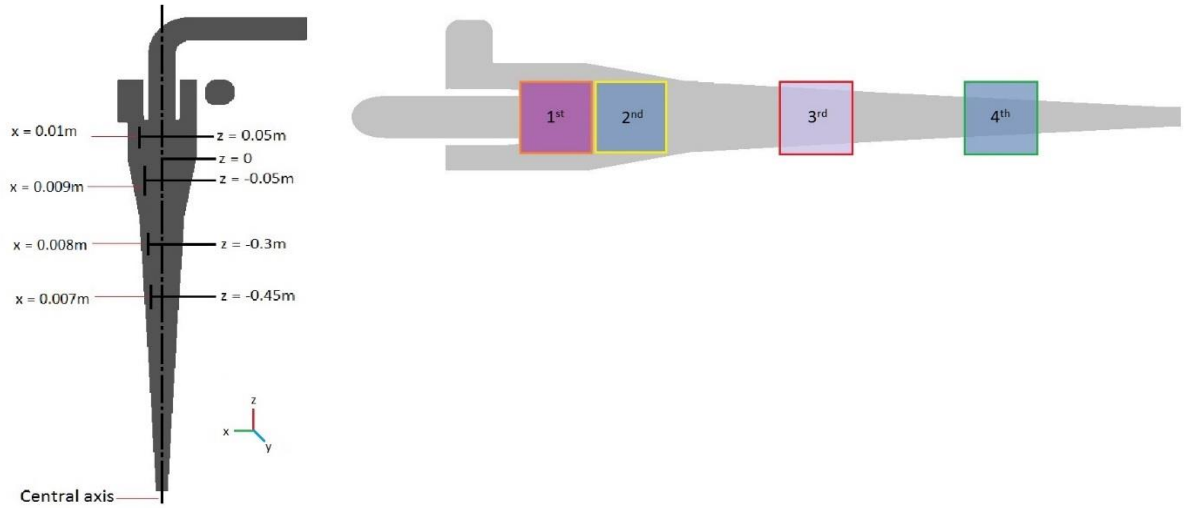

Figure 7.19 The interrogation planes and the test locations.

Figure 7.19 shows the position of the test planes used in both experiments and CFD to compare the values of velocities. The left image shows the relative position of the laser sheet with respect to the central axis of the hydrocyclone. While on the right, the image shows the position of planes in the r-z plane.

In this section, the velocity distributions along with various interrogation lines will be plotted for comparisons between the computational and experimental, and the positions of those interrogation lines are indicated in Figures 7.19. The PIV data files were post processed using the commercial software Tecplot Focus and the flow quantities along the center of each test location were imported to an excel sheet. The values for the computational works were exported from Star CCM+ directly by using “Probe” tool at the same location as in the experiment. The following plots show the comparison of the combination of the radial and tangential velocity that lie in the laser planes at the various test locations used in the experiments to the combination of radial and tangential velocity components which lie in the laser plane obtained from the CFD. Also the Axial Velocities at different interrogation lines are compared.

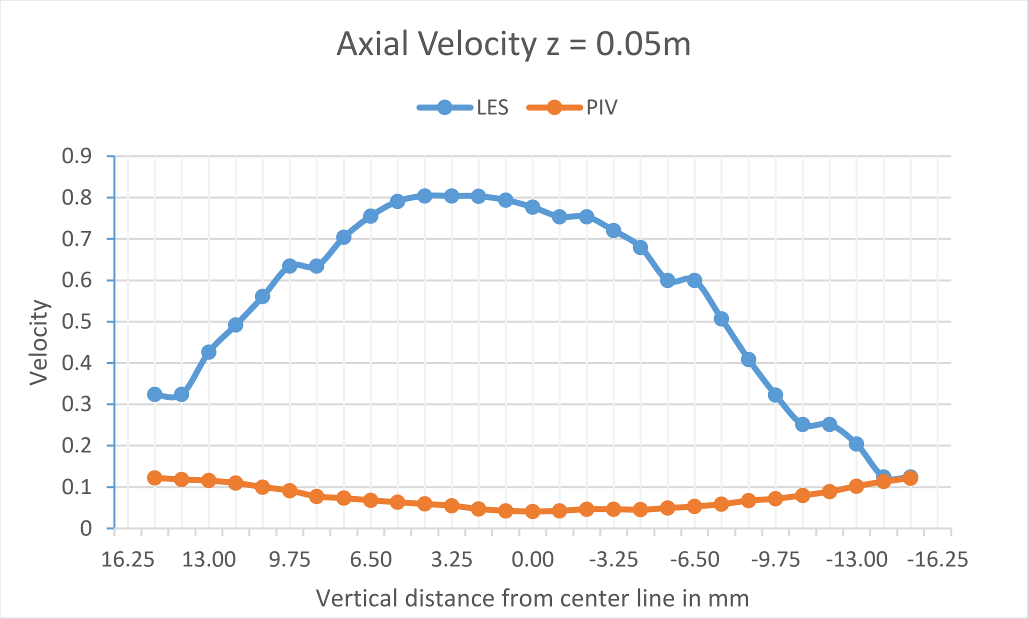

Figure 7.20 Comparison of axial velocity distributions in 1st section

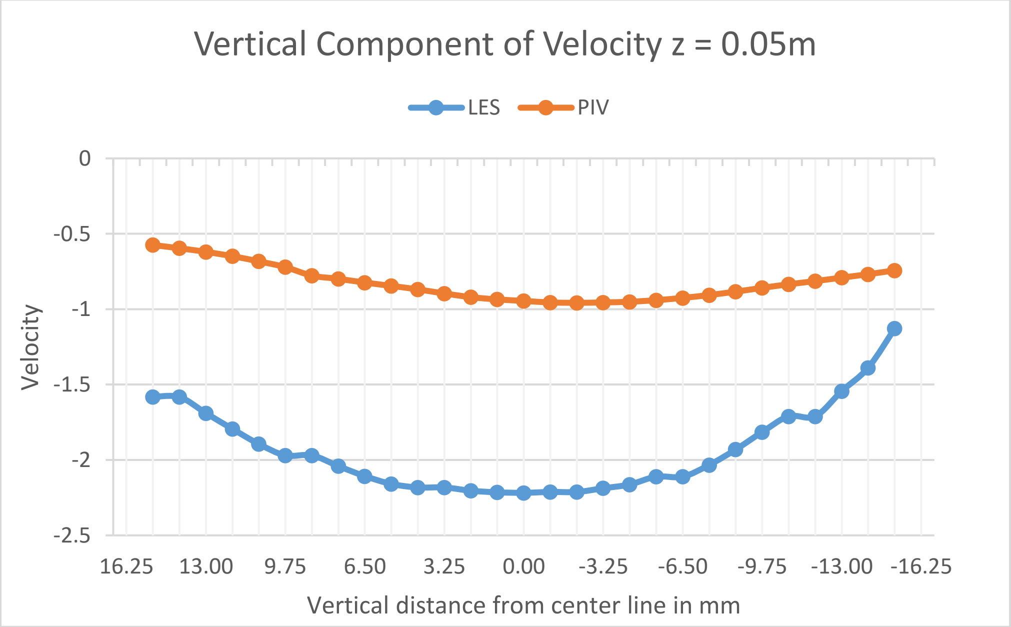

Figure 7.21 Comparison of vertical component of velocity distributions in 1st section

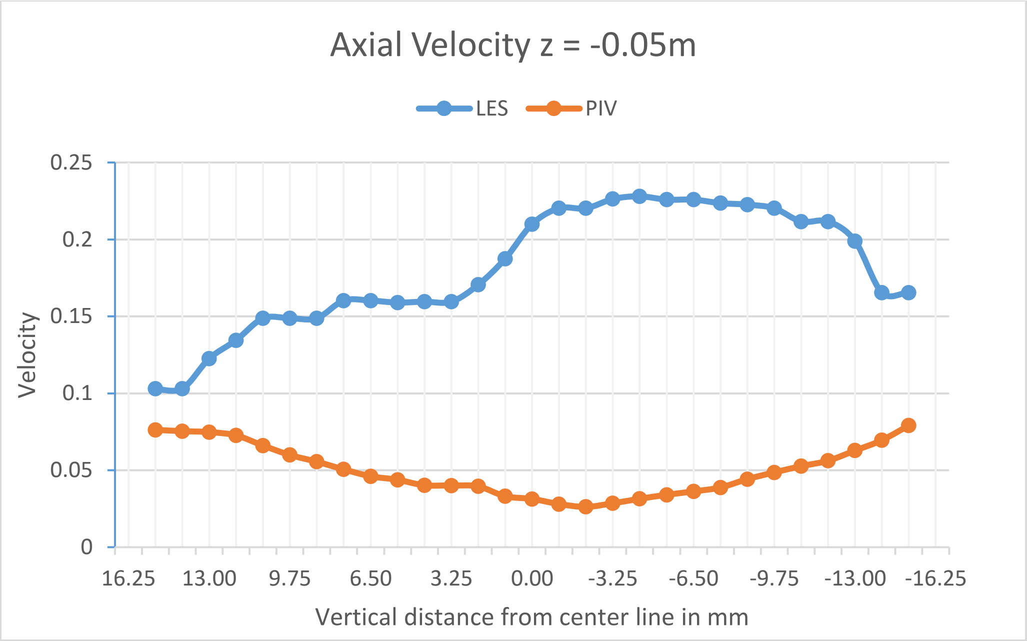

Figure 7.22 Comparison of axial velocity distributions in 2nd section

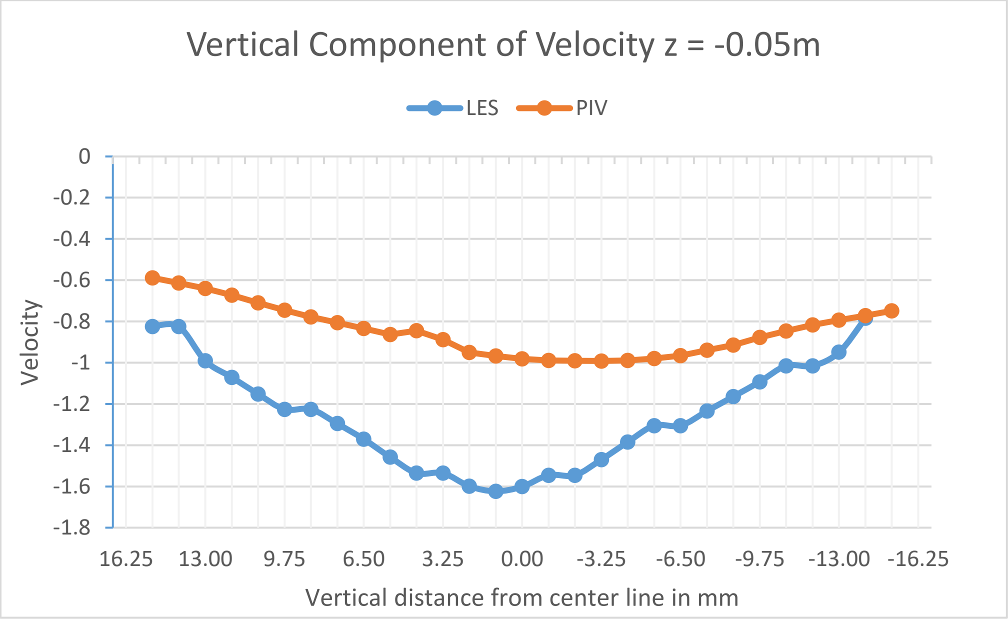

Figure 7.23 Comparison of vertical component of velocity distributions in 2nd section

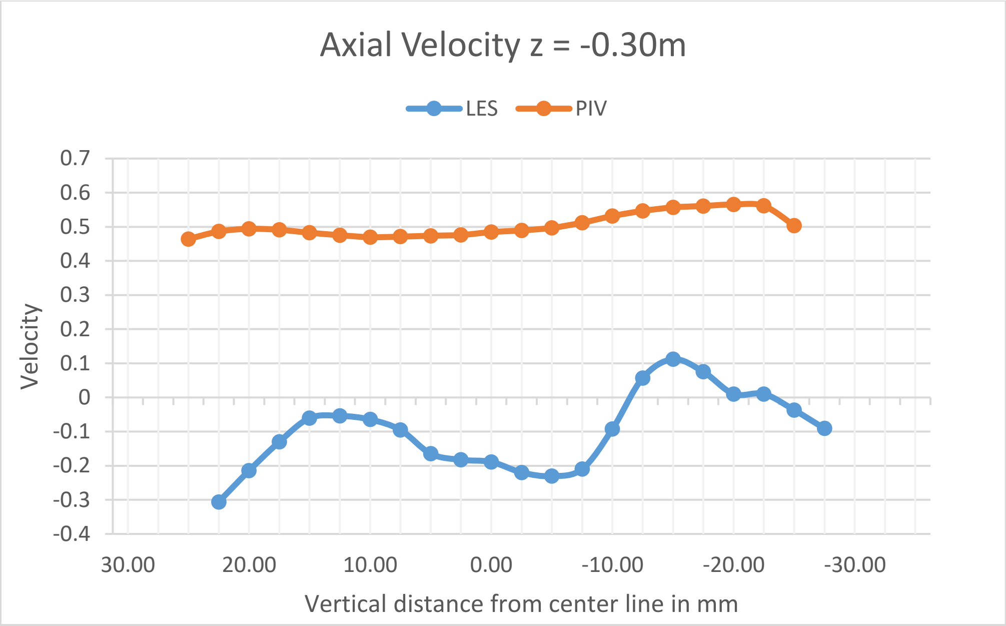

Figure 7.24 Comparison of axial velocity distributions in 3rd section

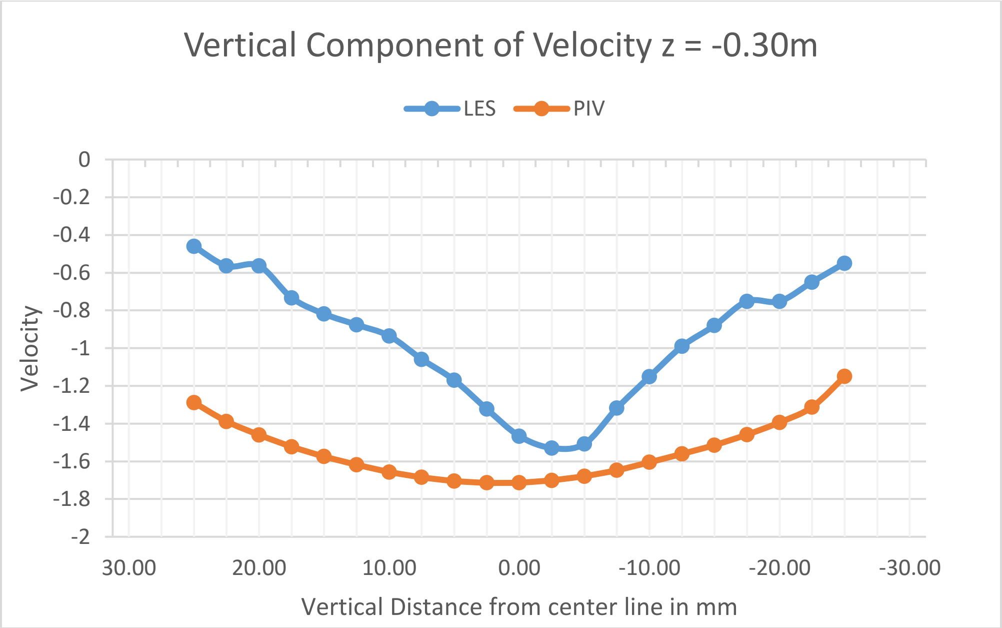

Figure 7.25 Comparison of vertical component of velocity distributions in 3rd section

The magnitude of velocity acquired by experimental and computational techniques are compared in figures 7.20 through 7.25.

The LES is more reliable in simulating the hydrocyclone flow in unsteady status than the RSM model (especially in the lower part of the hydrocyclone) despite the fact that RSM model has achieved great successes in simulation of cyclone without an air core (Kucukal 2015). The LES model also requires finer meshes than the RSM model based on the previous simulation works; therefore the extra computational costs will be introduced, and further investigations about these two model need to be conducted in order to choose the suitable model in specific cases.

CHAPTER 8

CONCLUSION AND FUTURE RECOMMENDATIONS

8.1 Conclusions

The objective of this study consisted of performing numerical simulations and experimental measurements with the aim of validating the computational model. The primary aim of this study included the investigation of the two-phase fluid flow inside a model hydrocyclone geometrically similar to a real Hydrocyclone with an air core generated at the central axis, using Particle Image Velocimetry (PIV); the second objective included validating the CFD results obtained using the commercial CFD software, CD-Adapco's Star CCM+. The conclusions achieved from the study are as follows:

(1) Only the Large eddy simulation model was used in the CFD simulations since it was considered to be more effective as demonstrated by Ke 2016. The LES model made a successful prediction for the values of the total and static pressure in the entire global flow field. A finer mesh was generated, and the LES model was able to produce a stable air core. The LES model predicted the value of static pressure with a difference of 14%.

(2) The SONARtrac instrument was used to obtain the percentage of air by volume in the overflow pipe section. This enabled the LES model to correctly produce a stable air core along the central axis of the hydrocyclone.

(3) The tangential, axial and radial components of the velocity from simulations were plotted at various interrogation lines at different axial depths. The maximum tangential velocities occurred outside of the air core area and inner vortex, where the liquid axial velocities approached zero value.

(4) The vectors obtained from the PIV measurements, was resolved into two components, the vertical component being the resultant of tangential and radial velocity, while the horizontal component to be the axial velocity as the data was taken in the r-z plane. The PIV measurements was compared to CFD values. The PIV data was taken on a plane offset from the air core, and it showed symmetrical results for the velocity magnitude around the air core.

(5) The simulation could not be validated by PIV data due to the lack of specific boundary conditions as in the overflow boundary was set to 0 Pa while the experimental data provided with a pressure value. Also further improvements to the model can be made in order to validate the simulation using the PIV data.

(6) Images of the air core were taken using a Cannon DSLR. These were then compared to the CFD results. The shape and size of the air core were in good agreement which proved the LES model to be suitable for simulations.

8.2 Future Recommendations

This study mainly concentrated on the properties of the axial velocity component of the fluid flowing inside the hydrocyclone. A future work can be done by taking data at a certain angle within the same plane sections.

A general system update to PIV can be done, as this study was performed on an older 32 bit version of PIVACQ and PIVPROC due to limitations of the computer. The 64 bit version developed by Dr. Wernet from NASA has more control over the process of acquiring and processing the PIV images. A high resolution camera can also facilitate capturing a larger FOV thereby allowing to study a larger area.

Alternative experimental methods can be employed to this work as PIV has limitations with the concentration of particles by volume. Pulsed Ultrasound Doppler Velocimetry (PUDV) methods can be used which can enable the measurement of velocity at high flow rates as refractive index matching is not mandatory for these methods. Additionally, water can be used as a test fluid with the non-optical techniques, which would result in eliminate the problem of air bubbles entering the hydrocyclone body at higher flow rates and feed pressures.

The CFD model can be improved further using the precise boundary conditions as obtained in this study. By employing a different experimental method, the simulations can be run using high inlet velocity for better stability of the air core as currently the simulations are running at a threshold value of inlet velocity.

Electrical resistance tomography (ERT) could be used to investigate the shape and diameter of the air core in dense phase slurry flows, and also to measure the concentration profiles at various sections along the cyclone. Additionally, the shape and diameter of the air core on NAI and water solutions can be investigated more carefully using grids and camera photos. In addition, the resistance temperature detector (RTD) could also be used to measure the liquid temperature in the tank.

References

Bai, Z.-s., Wang, H.-l., & Tu, S.-T. (2009). Experimental study of flow patterns in deoiling hydrocyclone. Minerals Engineering, 22(4), 319-323.

Bank, N., & Gauvin, W. (1977). Measurements of flow characteristics in a confined vortex flow. The Canadian journal of Chemical Engineering, 55(4), 397-402.

Bhaskar, K. U., Murthy, Y. R., Raju, M. R., Tiwari, S., Srivastava, J., & Ramakrishnan, N. (2007). CFD simulation and experimental validation studies on hydrocyclone. Minerals Engineering, 20(1), 60-71.

Bradley, D. The hydrocyclone, 1965: Pergamon Press, Great Britain.

Brennan, M. (2003). Multiphase CFD simulations of dense medium and classifying hydrocyclones. Paper presented at the Proceedings of the 3rd International Conference on CFD in the Minerals and Process Industries, CSIRO Melbourne Australia.

Bretney, E. (1891). bretney: Google Patents.

Chen, W., Zydek, N., & Parma, F. (2000). Evaluation of hydrocyclone models for practical applications. Chemical Engineering Journal, 80(1), 295-303.

Chiné, B., & Concha, F. (2000). Flow patterns in conical and cylindrical hydrocyclones. Chemical Engineering Journal, 80(1), 267-273.

Dai, G., Chen, W., Li, J., & Chu, L. (1999). Experimental study of solid–liquid two-phase flow in a hydrocyclone. Chemical Engineering Journal, 74(3), 211-216.

Delgadillo, J. A., & Rajamani, R. K. (2005). A comparative study of three turbulence-closure models for the hydrocyclone problem. International Journal of Mineral Processing, 77(4), 217-230.

Dlamini, M., Powell, M., & Meyer, C. (2005). A CFD simulation of a single phase hydrocyclone flow field. Journal-South African Institute of Mining and Metallurgy, 105(10), 711.

Dyakowski, T., & Williams, R. (1995). Prediction of air-core size and shape in a hydrocyclone. International Journal of Mineral Processing, 43(1), 1-14.

Evans, W. K., Suksangpanomrung, A., & Nowakowski, A. F. (2008). The simulation of the flow within a hydrocyclone operating with an air core and with an inserted metal rod. Chemical Engineering Journal, 143(1), 51-61.

Heiskanen, K. (1993). Particle classification: Chapman & Hall London.

Hoekstra, A., Derksen, J., & Van Den Akker, H. (1999). An experimental and numerical study of turbulent swirling flow in gas cyclones. Chemical Engineering Science, 54(13), 2055-2065.

Hoffmann, A. C., & Stein, L. E. (2002). Gas cyclones and swirl tubes. Springer-Verlag Berlin Heidelberg, 2008.

Karimi Mohsen, Akdogan Guven, Bradshaw Steven, Mainza Aubrey (2012), Numerical Modelling of Air Core in Hydrocyclones.

Kelsall, D. (1952). A study of the motion of solid particles in a hydraulic cyclone.

Ke R. (2016). Experimental and CFD investigations of the fluid flow inside a hydrocyclone separator with an air core. Case Werster Reserver University.

Kondukula Udaya, Ravi Raju, Ramakrishnan N.(2007), CFD Simulation and Experimental Validation Studies on Hydrocyclone.

Kucukal, E. (2015). EXPERIMENTAL AND CFD INVESTIGATIONS OF THE FLUID FLOW INSIDE A HYDROCYCLONE SEPARATOR WITHOUT AN AIR CORE. Case Western Reserve University.

Ma, L., Ingham, D., & Wen, X. (2000). Numerical modelling of the fluid and particle penetration through small sampling cyclones. Journal of Aerosol Science, 31(9), 1097-1119.

Narasimha, M., Brennan, M., & Holtham, P. (2006). Large eddy simulation of hydrocyclone—prediction of air-core diameter and shape. International Journal of Mineral Processing, 80(1), 1-14.

Park, S. H. (2003). Separation of polymer particles using a hydrocyclone.

Petty, C. A., & Parks, S. M. (2001). Flow predictions within hydrocyclones. Filtration & separation, 38(6), 28-34.

Pletcher, R. H., Tannehill, J. C., & Anderson, D. (2012). Computational fluid mechanics and heat transfer: CRC Press.

Rietema, K., & Maatschappij, S. I. R. (1961). Performance and design of hydrocyclones—I: General considerations. Chemical Engineering Science, 15(3), 298-302.

Shalaby, H., Pachler, K., Wozniak, K., & Wozniak, G. (2005). Comparative study of the continuous phase flow in a cyclone separator using different turbulence models. International journal for numerical methods in fluids, 48(11), 1175-1197.

Slack, M., Prasad, R., Bakker, A., & Boysan, F. (2000). Advances in cyclone modelling using unstructured grids. Chemical Engineering Research and Design, 78(8), 1098-1104.

Tennekes, H., & Lumley, J. L. (1972). A first course in turbulence: MIT press.

Wang, B., Xu, D., Chu, K., & Yu, A. (2006). Numerical study of gas–solid flow in a cyclone separator. Applied Mathematical Modelling, 30(11), 1326-1342.

Wang B, Ren J, Ma Y, Jin H (2010), Theorotical analysis and separation efficiency calculation of axial flow hydrocyclone for gas-liquid separation.

Wernet, M. P., & Pline, A. (1993). Particle displacement tracking technique and Cramer-Rao lower bound error in centroid estimates from CCD imagery. Experiments in Fluids, 15(4-5), 295-307.

Wernet, M. P. (2005). Lecture notes on fundamental of digital particle image velocimetry given at Case Western Reserve Universiy. Optical Instrumentation Technology Branch NASA Glenn Research Center.

Yakhot, A., Orszag, S. A., Yakhot, V., & Israeli, M. (1989). Renormalization group formulation of large-eddy simulations. Journal of Scientific Computing, 4(2), 139-158.

Young, G., Wakley, W., Taggart, D., Andrews, S., & Worrell, J. (1994). Oil-water separation using hydrocyclones: An experimental search for optimum dimensions. Journal of petroleum science and engineering, 11(1), 37-50.

Zhao, B. (2004). A theoretical approach to pressure drop across cyclone separators. Chemical engineering & technology, 27(10), 1105-1108.

Zhou, L. X., & Soo, S. L. (1990). Gas—solid flow and collection of solids in a cyclone separator.

Powder technology, 63(1), 45-53.